

Characterization of strained semiconductor structures using transmission electron microscopy

Dissertation

zur Erlangung des akademischen Grades
Doktor der Naturwissenschaften (Dr. rer. nat.)

der Technischen Fakultät
der Christian-Albrechts-Universität zu Kiel

Vasfi Burak Özdöl

Kiel

August 2011

1. Gutachter: Prof. Dr. Wolfgang Jäger
2. Gutachter: Prof. Dr. Peter van Aken
3. Gutachter: Prof. Dr. Lorenz Kienle

Datum der mündlichen Prüfung: 25/07/2011

Contents

1. General introduction	1
2. Electron-matter interaction and image formation in the TEM	5
2.1. Interaction of the electron beam with crystalline material	6
2.2. Image formation in the transmission electron microscope	8
3. Quantitative nanometer scale strain analysis in Si/SiGe heterostructures	12
3.1. Strain in epitaxially grown Si/SiGe heterostructures	13
3.2. TEM sample preparation techniques for quantitative strain analysis	16
3.3. Direct strain mapping from HRTEM images	19
3.4. Strain mapping using Geometric Phase Analysis (GPA)	23
3.5. Geometric phase analysis for complex-valued exit-face wave functions	27
3.6. Comparison of the methods	33
4. An efficient, simple and precise way to map strain with nanometer resolution in semiconductor devices	38
4.1. Introduction	39
4.2. Experimental	41
4.3. Results and discussion	43
4.4. Conclusion	47
5. A non-damaging electron microscopy approach to map In distribution in InGaN light-emitting diodes	50
5.1. Introduction	51

5.2. Experimental	52
5.3. Results and discussion	54
5.4. Conclusion	60
6. Correlating the structural, chemical and optical properties at nanometer resolution	63
6.1. Introduction	64
6.2. Experimental	66
6.3. Results and discussion	67
6.4. Conclusion	72
7. Dedicated sample preparation techniques for transmission electron microscopy	75
7.1. Indirect preparation methods	76
7.2. Preliminary preparation techniques	78
7.3. Cleavage	81
7.4. Chemical and electrolytic methods	83
7.5. Ion beam milling	85
7.6. Tripod polishing	90
7.7. Ultramicrotomy	93
7.8. Focused ion beam milling	95
7.9. Combination of different preparation methods	100
8. Conclusions and future works	109
Appendix	111
Acknowledgments	112
Curriculum Vitae	113

Chapter 1

General Introduction

Today's state of the art semiconductor electronic devices utilize the charge transport within very small volumes of the active device regions. The structural, chemical and optical material properties in these small dimensions can critically affect the performance of these devices. It is therefore crucial to characterize the material properties, which are directly related to the electronic band structure, quantitatively and at the nanometer scale for better understanding of the devices. The strain state of semiconductor materials, apart from the local electrostatic potential, is one of the most important material properties, which modifies the electronic band structure. Thus, engineering of nanoscale devices relies heavily on insight obtained from the characterization of the local stress-strain state.

High spatial resolution is a key requirement when characterizing material properties at the nanoscale. Transmission electron microscopy (TEM) is a well established technique to resolve device structures at the atomic level. TEM is widely used for local property analysis using diffraction contrast imaging in bright field (BF) and dark field (DF) conventional TEM, phase contrast imaging in high-resolution TEM (HRTEM), energy filtered imaging in energy-filtered TEM (EFTEM), using diffraction in selected area electron diffraction (SAED) or convergent beam electron diffraction (CBED) as well as utilizing microanalytical methods such as electron energy loss spectroscopy (EELS) and energy dispersive X-ray spectroscopy (EDXS). Although conventional techniques may reveal the strain state qualitatively, numerical image processing algorithms are required to extract quantitative information.

The elastic interaction of the fast electrons with the crystalline material inside the microscope is reflected in their wave function at the exit surface of the electron-transparent TEM sample:

$$\psi(\vec{r}) = \sum_{\vec{g}} (A_{\vec{g}} e^{i\phi_{\vec{g}}}) e^{2\pi i(\vec{k}_0 + \vec{g} + \Delta\vec{g}) \cdot \vec{r}} \quad (1.1)$$

where \vec{k}_0 is the electron wave vector inside the crystal, \vec{g} is the reciprocal lattice vector, $A_{\vec{g}}$ and $\varphi_{\vec{g}}$ are the amplitude and the phase of the diffracted beam and $\Delta\vec{g}$ stands for the variations in the crystal periodicity of reciprocal space vector \vec{g} . In absence of variations in specimen composition, thickness or specimen bending $\varphi_{\vec{g}}$ represents the geometric phase which describes local deviations of the lattice fringes from the positions in the ideal, un-strained crystal.

Quantitative measures of the strain can be obtained by extracting the $\Delta\vec{g}$ term using different techniques. One way to visualize the variations in crystal periodicity is the analysis of the lattice fringe shifts in HRTEM using the technique referred as geometric phase analysis (GPA). Another approach, which is defined here as “Dark-field Inline Electron Holography (DIH)”, relies on the reconstruction of $\varphi_{\vec{g}}$ from a focal series of DF images.

The present dissertation is based on several manuscripts which are already published or in press, where I am the first author or co-author. The thesis is organized in the following order. Chapter 2 is devoted to the fundamentals of image formation inside the TEM: the electron-matter interaction, its effect on the electron wave function and the resulting image. In chapter 3, experimental TEM techniques for characterization of the strain state in semiconductor materials are discussed using a Si/SiGe model heterostructure. It includes the preparation methods to achieve the required specimen quality for quantitative analysis and the fundamentals of strain analysis using HRTEM related techniques. In Chapter 4, the strain state in metal oxide semiconductor field-effect transistor (MOSFET) channels is investigated by the DIH method using strain engineered 45nm p-MOS transistor arrays [1]. The experimental advantages over strain mapping by HRTEM will be discussed. Chapter 5 is dedicated to compositional and structural analysis on InGaN quantum wells (QWs) in high efficiency green light-emitting diodes [2]. Low electron dose HRTEM and DIH techniques are exploited to overcome the well-known electron beam induced modification of InGaN QWs inside the microscope. In Chapter 6, strain mapping is used as a complementary technique to correlate the structural, chemical and optical properties at the nanometer scale [3]. A GaN/AlGaN model heterostructure is investigated using EELS, plasmon mapping by EFTEM and strain mapping by HRTEM. As a special topic, advances in dedicated sample preparation for TEM are

reviewed in Chapter 7 [4]. Finally, conclusions and future work is summarized in Chapter 8.

References:

- [1] C. T. Koch, V. B. Özdöl, and P. A. van Aken, *An efficient, simple, and precise way to map strain with nanometer resolution in semiconductor devices*, Appl. Phys. Lett. **96**, pp. 091901-091903 (2010).
- [2] V. B. Özdöl, C. T. Koch, and P. A. van Aken, *A nondamaging electron microscopy approach to map In distribution in InGaN light-emitting diodes*, Journ. of Appl. Phys. **108**, pp. 056103-056105 (2010).
- [3] L. Gu, V. B. Özdöl, W. Sigle, C. T. Koch, V. Srot, and P. A. van Aken, *Correlating the structural, chemical, and optical properties at nanometer resolution*, Journ. of Appl. Phys. **107**, pp. 013501-013504 (2010).
- [4] V. B. Özdöl, V. Srot, and P. A. van Aken, *Dedicated sample preparation for transmission electron microscopy*, in Handbook of Nanoscopy, Wiley-VCH, Weinheim, in press (2011).

Chapter 2

Electron-matter interaction and image formation in the TEM

Abstract:

When an electron beam passes through a thin slice of a material, it interacts with the atoms in that volume, and its wave function is changed, imprinting in it information about the electron-matter interaction. The aim of characterization by using electron beams is to retrieve information about small volumes of the material. Therefore, it is important to understand how these interactions, namely elastic and inelastic scattering processes, are encoded into the electron wave function and how the wave function forms the image in the TEM. For the scope of this dissertation, the following chapter will focus on elastic scattering processes in crystalline semiconductor materials as well as how the electron wave is translated to an image in TEM.

2.1 Interaction of the electron beam with crystalline material

The interaction of a single electron with a crystalline material can be described by solving the Schrödinger equation given by [1]:

$$\nabla^2 \psi(\vec{r}) + \frac{8\pi^2 m_0 e}{h^2} (U_A + V(\vec{r})) \psi(\vec{r}) = 0 \quad (2.1)$$

where $\psi(\vec{r})$ is the wave function of the fast electron at the specimen exit surface, h is Planck's constant, $V(\vec{r})$ is the crystal potential and U_A , m_0 and e are the acceleration voltage, the rest mass and the charge of the electron, respectively. The potential $V(\vec{r})$ of a periodic crystal can be formulated as a Fourier series:

$$V(\vec{r}) = V_0 + \sum_{\vec{g} \neq 0} V_{\vec{g}} e^{2m\vec{g} \cdot \vec{r}} \quad (2.2)$$

where V_0 is the mean inner potential of the crystal, \vec{g} is the lattice vector in reciprocal space and $V_{\vec{g}}$ are the Fourier coefficients of the crystal potential. The mean inner potential, V_0 is the atomic potential averaged over the volume of the crystal. $V(\vec{r})$, as a function of position, is shown graphically in Fig. 2.1.

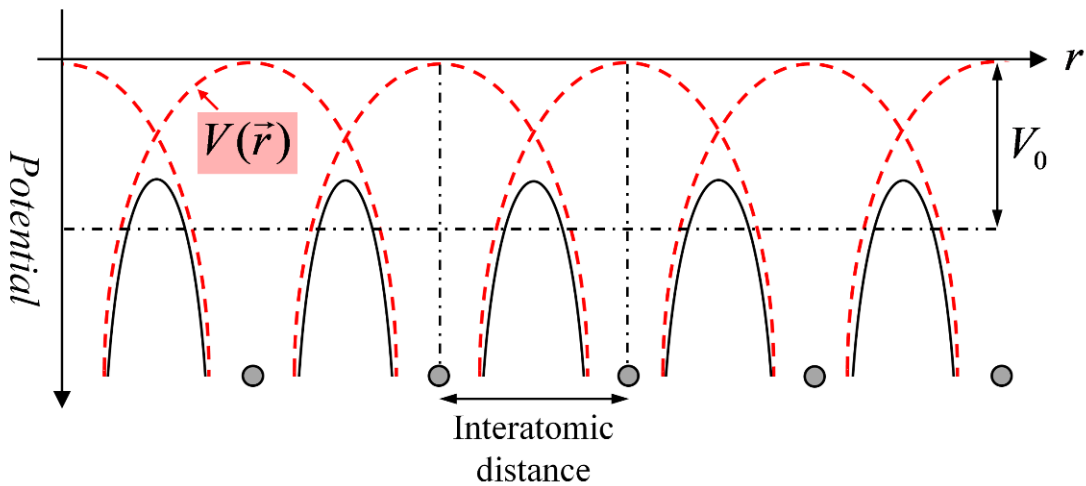


Fig. 2.1: Schematic diagram showing the potential change with respect to atomic position.

Inserting Eq. (2.2) into Eq. (2.1), the following formulation can be obtained:

$$\nabla^2 \psi(\vec{r}) + 4\pi^2 k_0^2 \psi(\vec{r}) = -\frac{8\pi^2 m_0 e}{h^2} \left(\sum_{\vec{g} \neq 0} V_{\vec{g}} e^{2\pi i \vec{g} \cdot \vec{r}} \right) \psi(\vec{r}) \quad (2.3)$$

where the wave number k_0 of the fast electron is defined as:

$$k_0 \equiv \frac{\sqrt{2m_0 e(U_A + V_0)}}{h} \quad (2.4)$$

Assuming the electrons travel only in directions \vec{k}_0 and $\vec{k}_0 + \vec{g}$, the general solution for Eq. (2.3) corresponding to the electron exit wave function can be described as a Fourier series [1]:

$$\psi(\vec{r}) = \sum_{\vec{g}} H_{\vec{g}} e^{2\pi i (\vec{k}_0 + \vec{g}) \cdot \vec{r}} \quad (2.5)$$

where $H_{\vec{g}}$ is the Fourier coefficient corresponding to reflection \vec{g} , \vec{k}_0 is the electron wave vector in the crystal. The complex coefficient $H_{\vec{g}}$ can be written as:

$$H_{\vec{g}} = A_{\vec{g}} e^{i\varphi_{\vec{g}}} \quad (2.6)$$

where $A_{\vec{g}}$ is the modulus and $\varphi_{\vec{g}}$ is the phase of the reflection \vec{g} . Therefore, the exit wave function contains the electron wave phase term of $\varphi_{\vec{g}}$ [1].

2.2 Image formation in the transmission electron microscope

Image formation in the transmission electron microscope is commonly described using the Abbé imaging process, as shown graphically in Fig. 2.2. The exit wave function translates to reciprocal space at the back focal plane of the objective lens of the microscope. The reciprocal space wave function (its squared amplitude is the diffraction pattern) can be formulated by the Fourier transform (FT) of the exit wave function as follows:

$$\begin{aligned}\tilde{\psi}(\vec{k}) &= FT\{\psi(\vec{r})\} = \sum_{\vec{g}} H_{\vec{g}} \int e^{2\pi i((\vec{k}_0 + \vec{g}) - \vec{k}) \cdot \vec{r}} d\vec{r} \\ &= \sum_{\vec{g}} H_{\vec{g}} \delta(\vec{k} - (\vec{k}_0 + \vec{g}))\end{aligned}\quad (2.7)$$

where \vec{k} is the coordinate of the Fourier space [2].

The aberrations in the objective lens of the microscope give a phase shift to each diffracted beam, which is modeled in terms of the contrast transfer function (CTF) of the microscope, $T(\vec{k})$ [2]:

$$T(\vec{k}) = e^{i\chi(\vec{k})}\quad (2.8)$$

in which the aberration function, $\chi(\vec{k})$, can be simplified as follows, including only the spherical aberration coefficient, C_s , and defocus, Δf of the objective lens:

$$\chi(\vec{k}) = 0.5\pi C_s \lambda^3 k^4 + \pi \Delta f \lambda k^2\quad (2.9)$$

The aberrated wave function at the back focal plane of the objective lens, $\tilde{\Psi}(\vec{k})$, is given by:

$$\tilde{\Psi}(\vec{k}) = \tilde{\psi}(\vec{k})T(\vec{k}) = \sum_{\vec{g}} T(\vec{k})H_{\vec{g}}\delta(\vec{k} - (\vec{k}_0 + \vec{g}))\quad (2.10)$$

The wave function in the image plane, $\tilde{\Psi}(\vec{r})$, is the inverse Fourier transform (FT⁻¹) of the aberrated wave function

$$\tilde{\Psi}(\vec{r}) = FT^{-1}\{\tilde{\Psi}(\vec{k})\} = \int \sum_{\vec{g}} T(\vec{k})H_{\vec{g}}\delta(\vec{k} - (\vec{k}_0 + \vec{g}))e^{2\pi i\vec{k} \cdot \vec{r}} d\vec{k}$$

$$= \sum_{\vec{g}} T(\vec{g}) H_{\vec{g}} e^{2\pi i(\vec{k}_0 + \vec{g}) \cdot \vec{r}} \quad (2.11)$$

where the summation includes all the diffracted beams passing through the objective aperture positioned in the back focal plane [3].

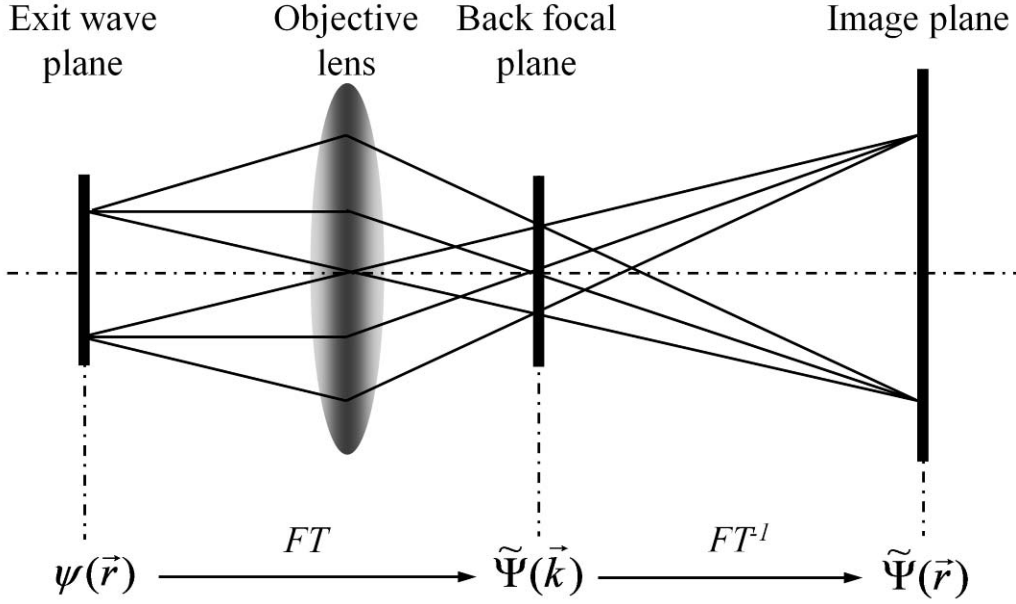


Fig. 2.2: Schematic diagram showing the Abbé theory of image formation in the transmission electron microscope.

The contrast in the image is simply the position-dependent intensity, $I(\vec{r})$:

$$\begin{aligned} I(\vec{r}) &= |\Psi(\vec{r})|^2 = \sum_{i,j} \Psi_{\vec{g}_i}(\vec{r}) \Psi_{\vec{g}_j}^*(\vec{r}) \\ &= \sum_{i,j} T(\vec{g}_i) T^*(\vec{g}_j) H_{\vec{g}_i} H_{\vec{g}_j}^* e^{2\pi i(\vec{g}_i - \vec{g}_j) \cdot \vec{r}} \end{aligned} \quad (2.12)$$

For $\vec{g} = 0$ the intensity equation, describing the bright-field (BF) image contrast, is reduced to $I(\vec{r}) = A_0^2$, where A_0 is the modulus of Fourier coefficient of the transmitted beam. In conventional TEM, the image intensity is formed by recording only the moduli of the complex Fourier coefficients; the information about the phase of the electron wave function is lost. In HRTEM, transmitted and diffracted beams included in the objective aperture are used for image formation, where the phase differences between $\vec{g} = 0$, and nonzero \vec{g} 's results in periodic contrast.

Therefore, HRTEM image contrast relies on phase differences, but the phases of the electron beams are not measured individually.

In contrast to conventional and high-resolution TEM, electron holography is a technique that aims to reconstruct the phase of the electron wave directly. Apart from material properties like internal electrostatic potential or magnetic fields, electron holography is also sensitive to strain fields. Another “phase” in electron microscopy is the geometric phase in HRTEM images, which describes the shifts of lattice fringes as phase shifts in Fourier space. In the following chapters, these two “phase” terms are exploited in order to derive quantitative strain information that is not accessible using conventional imaging techniques.

References:

- [1] M. De Graef, *Introduction to conventional transmission electron microscopy*, Cambridge University Press, Cambridge (2003).
- [2] B. Fultz, and J. M. Howe, *Transmission electron microscopy and diffractometry of materials*, Springer, Berlin (2001).
- [3] Williams, D.B. and Carter, C.B. *Transmission Electron Microscopy: A Text Book for Materials Science*, Springer, New York (2009).

Chapter 3

Quantitative nanometer scale strain analysis in Si/SiGe heterostructures

Abstract:

Experimental TEM techniques for characterization of local strain in Si/SiGe model heterostructures are discussed including the preparation methods to achieve the required specimen quality for quantitative analysis and the fundamentals for strain analysis using HRTEM related techniques. Application of a peak-finding method and geometric phase analysis (GPA) is demonstrated. The required imaging conditions as well as the limitations of GPA are addressed. A modified version of GPA, which is based on the analysis of the reconstructed exit wave function, is proposed to overcome artifacts arising from the imperfect objective lens in the TEM.

3.1 Strain in epitaxially grown Si/SiGe heterostructures

Heterostructures with lattice mismatch can be grown without introducing misfit dislocations if the films are below a certain critical thickness. The mismatch is then completely accommodated by biaxial lattice strain. For $\text{Si}_{1-x}\text{Ge}_x$ on Si, compressive strain in the $\text{Si}_{1-x}\text{Ge}_x$ layer parallel to the interface requires that the lattice constants perpendicular to the interface adjust independently to minimize the elastic energy. The lattice constant perpendicular to the interface must be increased because of the Poisson's ratio effect. The resulting tetragonal distortion in the so-called pseudomorphic growth lowers the energy of the interfacial atoms at the expense of stored strain energy within the coherent layers [1].

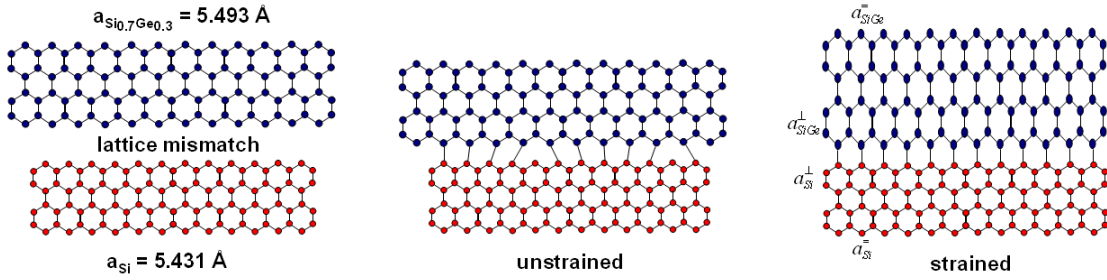


Fig. 3.1: Schematic diagram showing the lattice mismatch between Si and SiGe film (left), and the unstrained state due to the formation of misfit dislocations (middle), and the strained state in the case of coherent film growth (right). The lattice constants for Si and Ge are taken from Ref. [4].

The atomic positions and strain in the coherently grown heterostructure can be determined by minimizing the macroscopic elastic energy [2]. When Si and $\text{Si}_{1-x}\text{Ge}_x$ with lattice constants a_{Si} and $a_{\text{Si}_{1-x}\text{Ge}_x}$ (see Fig. 3.1) form a heterostructure, the lattice constants of the heterostructure are given as follows, assuming the lattice constant parallel to the plane of the interface to remain unchanged throughout the structure: [3]

$$a_{\text{Si}_{1-x}\text{Ge}_x}^{\parallel} = a_{\text{Si}}^{\parallel} = \frac{a_{\text{Si}_{1-x}\text{Ge}_x} G_{\text{Si}_{1-x}\text{Ge}_x} h_{\text{Si}_{1-x}\text{Ge}_x} + a_{\text{Si}} G_{\text{Si}} h_{\text{Si}}}{G_{\text{Si}_{1-x}\text{Ge}_x} h_{\text{Si}_{1-x}\text{Ge}_x} + G_{\text{Si}} h_{\text{Si}}}, \quad (3.1)$$

$$a_{\text{Si}_{1-x}\text{Ge}_x}^{\perp} = a_{\text{Si}_{1-x}\text{Ge}_x} \left(1 - \frac{2C_{12}^{\text{Si}_{1-x}\text{Ge}_x}}{C_{11}^{\text{Si}_{1-x}\text{Ge}_x}} \left(\frac{a_{\text{Si}}^{\parallel}}{a_{\text{Si}_{1-x}\text{Ge}_x}^{\parallel}} - 1 \right) \right), \quad (3.2)$$

where “ \parallel ” and “ \perp ” indicates the lattice constants parallel and perpendicular to the plane of the heterostructure interface, respectively. Assuming the substrate thickness h_{Si} is infinite, $a_{Si_{1-x}Ge_x}^{\parallel} = a_{Si}^{\parallel}$. The shear modulus in the $\langle 001 \rangle$ directions within the (001) plane, $G_{Si_{1-x}Ge_x}^{001}$, is given by:

$$G_{Si_{1-x}Ge_x}^{001} = 2(C_{11}^{Si_{1-x}Ge_x} + 2C_{12}^{Si_{1-x}Ge_x})\left(1 - \frac{C_{12}^{Si_{1-x}Ge_x}}{C_{11}^{Si_{1-x}Ge_x}}\right), \quad (3.3)$$

where C_{11} and C_{12} are the elastic constants. The elastic constants of Si, Ge, and $Si_{1-x}Ge_x$ are given in Table 3.1.

The strain components in the strained layer are determined by:

$$\varepsilon_{Si_{1-x}Ge_x}^{\parallel} = \left(\frac{a_{Si_{1-x}Ge_x}^{\parallel} - a_{Si_{1-x}Ge_x}}{a_{Si_{1-x}Ge_x}}\right), \quad (3.4)$$

$$\varepsilon_{Si_{1-x}Ge_x}^{\perp} = \left(\frac{a_{Si_{1-x}Ge_x}^{\perp} - a_{Si_{1-x}Ge_x}}{a_{Si_{1-x}Ge_x}}\right). \quad (3.5)$$

Fig. 3.2 shows the schematic diagram and typical BF image of the Si/Si_{0.7}Ge_{0.3} model structure. In this case, the strained Si_{0.7}Ge_{0.3} layer has $\varepsilon_{Si_{1-x}Ge_x}^{\parallel} = -1.24\%$ and $\varepsilon_{Si_{1-x}Ge_x}^{\perp} = 0.95\%$.

	Lattice constant (Å)	C_{11} (GPa)	C_{12} (GPa)
<i>Si</i>	5.4309	165.7	63.9
<i>Ge</i>	5.6575	128.5	48.3
$Si_{1-x}Ge_x$	$(1-x)a_{Si} + xa_{Ge}$	$(1-x)C_{11}^{Si} + xC_{11}^{Ge}$	$(1-x)C_{12}^{Si} + xC_{12}^{Ge}$

Table 3.1: Material properties for Si, Ge and SiGe alloy [4].

Taking the Si substrate as the reference, a relative strain, $\varepsilon_{rel Si_{1-x}Ge_x}^{\parallel}$, can be defined as the change in the lattice constant of the strained layer relative to the Si lattice as follows:

$$\varepsilon_{rel Si_{1-x}Ge_x}^{\parallel} = \left(\frac{a_{Si_{1-x}Ge_x}^{\parallel} - a_{Si}}{a_{Si}}\right), \quad (3.6)$$

$$\varepsilon_{rel Si_{1-x}Ge_x}^{\perp} = \left(\frac{a_{Si_{1-x}Ge_x}^{\perp} - a_{Si}}{a_{Si}} \right). \quad (3.7)$$

It will be convenient to use the relative strain for the following measurements, because the strain in the strained structure is to be measured relative to the strain in the reference layer which is defined as zero. Unless otherwise stated, the strain values will be given relative to the reference substrate material.

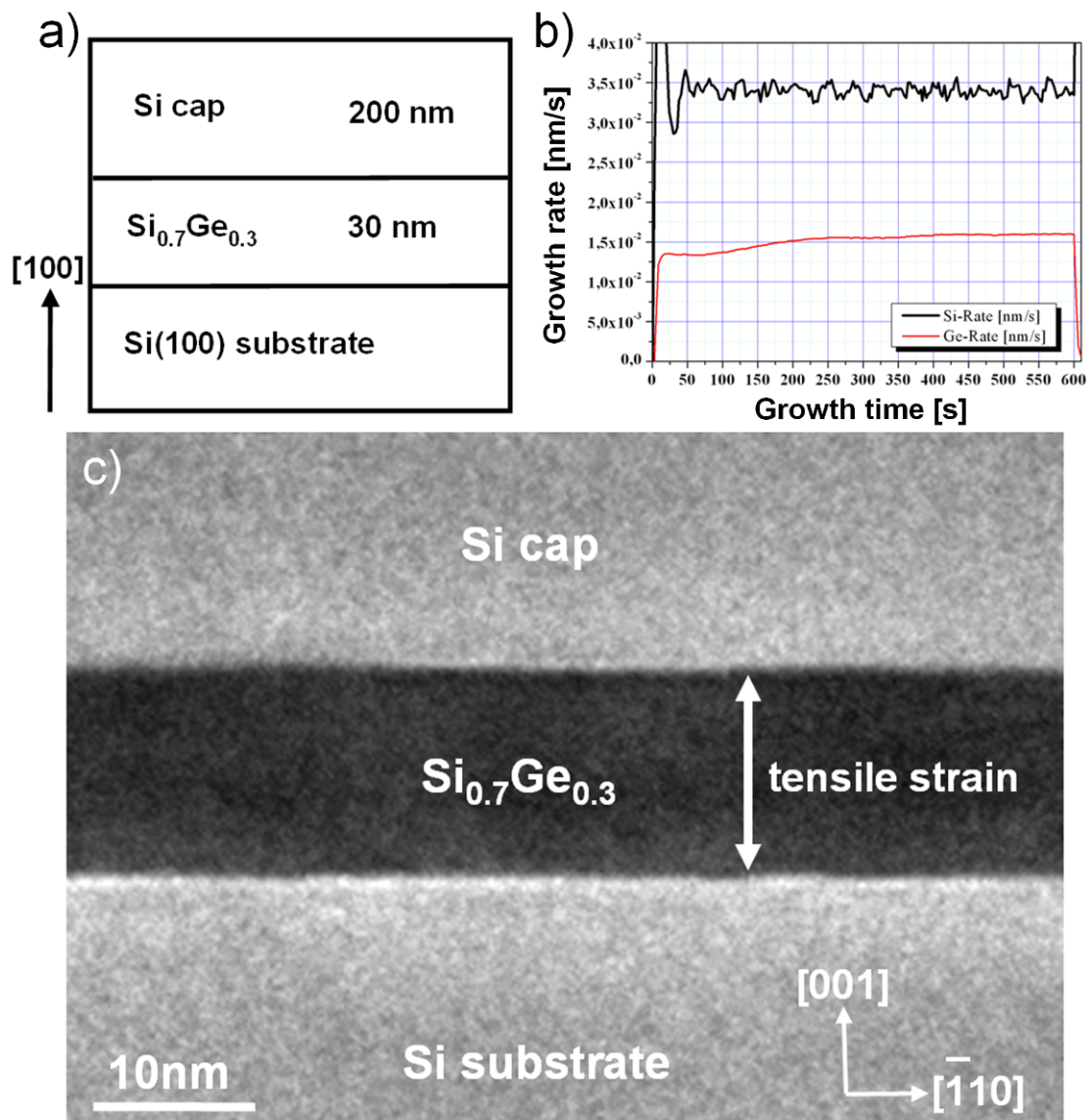


Fig. 3.2: (a) Schematic diagram of the Si/SiGe heterostructure. A SiGe film with 30% Ge and a nominal thickness of 30 nm was grown by molecular-beam epitaxy on a (001)-oriented Si substrate at 500 °C and subsequently capped by a Si layer of 200 nm [Si/SiGe heterostructures were grown by Erich Kasper and his group at Stuttgart University. See ref. 4 for an overview]. (b) Growth rate vs. growth time of the SiGe film. (c) Cross-sectional BF image of the heterostructure.

3.2 TEM sample preparation techniques for quantitative strain analysis

Quantitative strain analysis based on HRTEM ideally requires the preparation of specimens of very high quality. Specimens so prepared therefore should have a uniform thickness (< 30 nm) with relatively flat surfaces. The most widely used preparation method for hard materials to achieve electron transparency is mechanical thinning followed by successive final ion beam milling (a detailed review on sample preparation is given in Chapter 7). The more conventional way of performing mechanical thinning from pre-cut specimen is to grind a concave impression (polishing in a basin shape) or dimple, thinning the center of a disk to 3 mm in diameter and about several tens of microns thick, so that final thinning by Ar ion milling can then be performed. During ion milling it is necessary to take into account the fact that preferential thinning might occur at the interface, in this case at the Si/SiGe interface. This effect is minimized by reducing the incidence angle of the accelerated Ar ions relative to the sample surface. Fig. 3.2(a) shows a HRTEM image of the Si/SiGe interface along the $[110]$ zone axis. The ion milling was performed with the precision-ion-polishing system (PIPS, Gatan, Pleasanton, USA) using accelerated Ar ions operated at 4.0 keV. The beam angle of incidence for both ion guns was set to 8° . The sample was in continuous rotation mode to minimize the redeposition of the sputtered material. The major artifact in conventional ion milling is the modification of the sample surface of the crystalline material. The resulting surface amorphization can be minimized by lowering the ion beam energy and also by avoiding the temperature increase at the specimen surface. The high quality HRTEM image in Fig 3.2(b) was obtained from a specimen prepared by ion milling with progressively lowering the of the Ar ions energy (from 4.0 to 0.2 keV) in a liquid nitrogen cooled stage.

Another mechanical thinning method prior to ion milling is tripod polishing. The specimen is mounted on a tripod polisher and first mechanically polished on one side, using a sequence of progressively finer diamond lapping films (from $30\ \mu\text{m}$ to $0.1\ \mu\text{m}$). The surface is then briefly polished with a cloth wheel using colloidal silica ($0.05\text{-}0.02\ \mu\text{m}$) to attain the final polish. By introducing a wedge angle during final polishing of the other surface, it is possible to obtain an electron transparent wedged

edge. Fig. 3.2(c) displays an HRTEM image from a sample prepared by automated tripod polishing using the AlliedTech MultiPrep System with successive low energy ion milling mounting the sample in a cooled stage. To avoid specimen bending, which is another detrimental effect in the conventional preparation technique, the wedge angle had to be limited to 1.0°-1.5°. Apart from the high surface quality obtained by reducing the ion milling time considerably compared to the conventional method,

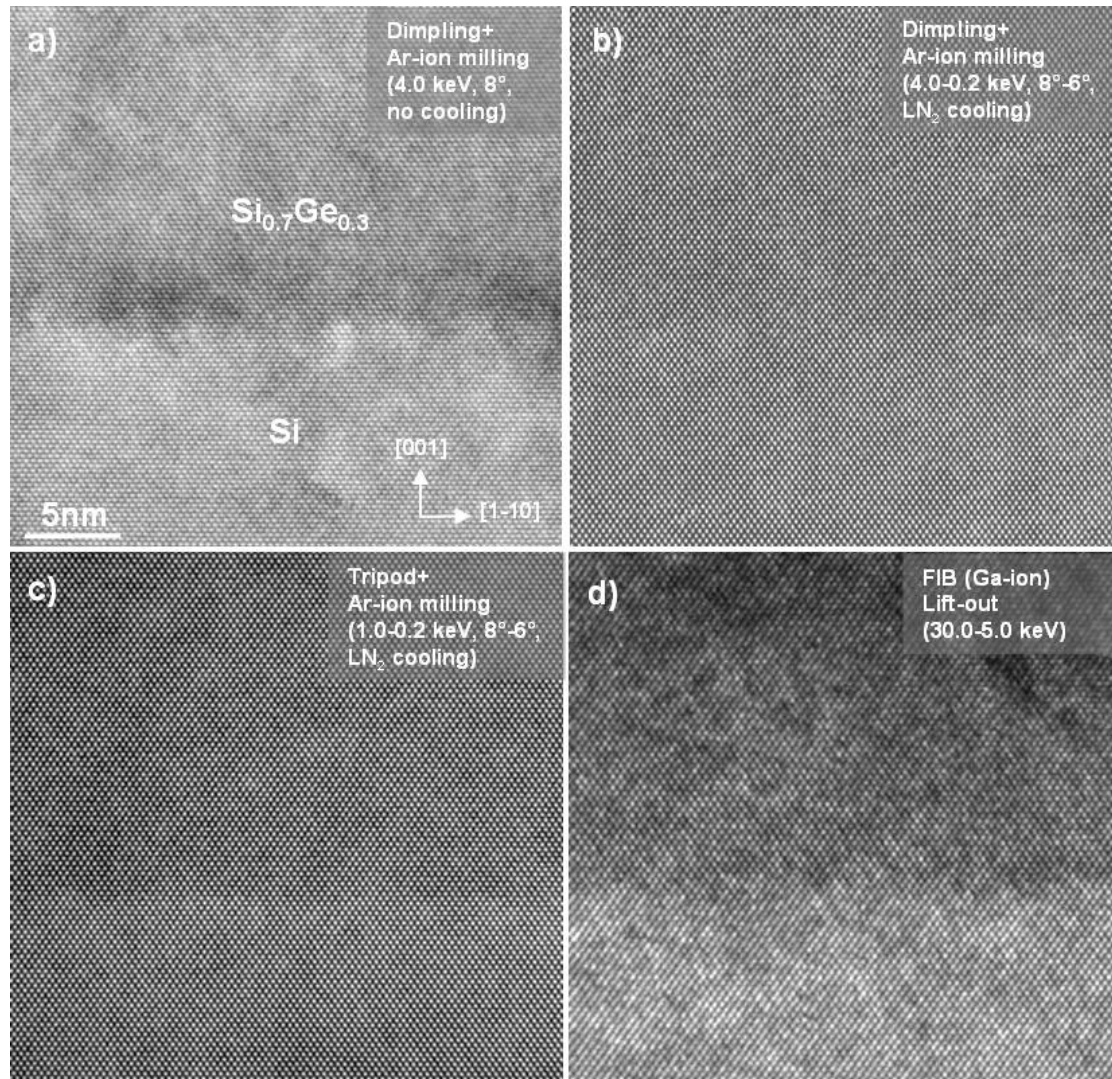


Fig. 3.2: [110] HRTEM images of a Si/SiGe interface from cross sectional TEM samples prepared by different techniques: (a) Dimple grinding and final Ar ion beam thinning at 4.0 keV energy at an incidence angle of 8°. The high energy ion bombardment causes excessive heating of the specimen and surface damage by amorphization. (b) The artifacts can be decreased by lowering the accelerating voltage of the Ar ions (1.0-0.2 keV) and liquid nitrogen assisted cooling of the specimen stage. (c) Tripod polishing and final low energy Ar ion milling (1.0-0.2 keV) with liquid nitrogen cooling. The surface damage is minimized by decreasing the ion milling time. (d) Focused ion beam lift out using Ga ions at 30 keV energy followed by final thinning at 5 keV. The bombardment by heavy Ga ions results in surface amorphization and Ga implantation. The quality of the HRTEM image is further reduced by the limited minimum thickness achievable by this method.

much larger specimen areas are possible to obtain for quantitative HRTEM analysis.

Focused ion beam (FIB) milling using Ga ion is widely employed in sample preparation for TEM, especially to investigate particular points on semiconductor devices with sub-micron positional accuracy. Short sampling time, ease of providing a flat cross-section and a positional accuracy better than 0.5 μm are its main advantages. Although FIB is quite useful for characterizing device structures, the samples are usually quite thick for HRTEM observations, as shown in Fig 3.2(d). The specimen was prepared by the lift-out technique. The severe surface damage introduced by high energy 30 keV Ga bombardment may be reduced by lowering the energy to 5 keV for the final polish. However it was still not possible to obtain the required quality for quantitative analysis. Another major drawback of high energy ion milling is the Ga implantation, which introduces errors during strain analysis of the crystalline structures.

3.3 Direct strain mapping from HRTEM images

Direct strain mapping relies on the assumption that a HRTEM micrograph of a coherent structure recorded under proper conditions represents the geometry of the lattice. The positions of the image maxima/minima depend on specimen thickness and orientation, imaging parameters such as defocus and microscope alignment, etc, and, thus do not necessarily coincide with the projections of the atom columns [5]. Nevertheless, a constant spatial relationship between the image intensity maxima/minima and the projected atom columns can be assumed on a local scale. A mismatch in lattice constants between a strained epitaxial $\text{Si}_{1-x}\text{Ge}_x$ layer and the reference lattice of the Si substrate results in a cumulative displacement, u_n , as shown schematically in Fig. 3.3. It is possible to determine the displacement that is defined as the difference between real atomic position and the reference lattice position as follows:

$$u_n = \sum_0^n (a_{\text{Si}_{1-x}\text{Ge}_x}^\perp - a_{\text{Si}}) \quad (3.8)$$

It is also necessary to consider the relaxation which occurs due to the thinning of the TEM specimen. HRTEM is very insensitive to the displacements in the direction of the transmitted electron beam. Such in-plane displacements are expected to be small, however more exact measurements for these displacements requires finite element simulation of relaxation. Lattice relaxation of the SiGe film with increasing distance from the interface was minimized by deposition of an epitaxial Si capping layer following the growth of SiGe film.

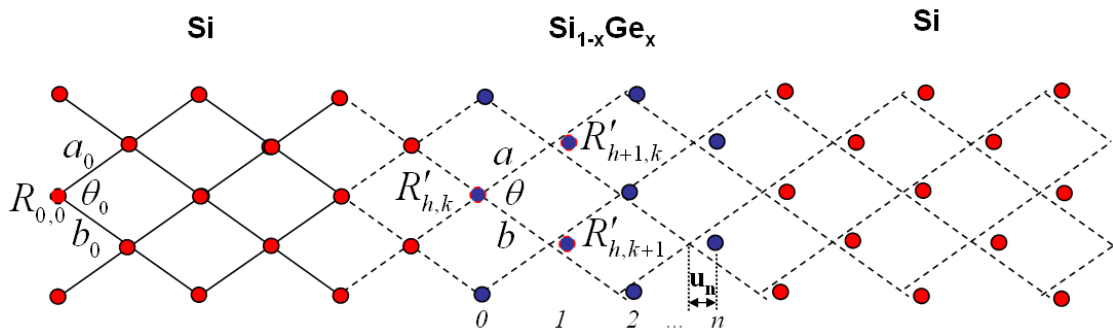


Fig. 3.3: Schematic diagram of displacements in a HRTEM image.

A widely used approach to determine the lattice displacements relies on the use of image processing algorithms which work in real image space. Displacements are measured by superimposing a two-dimensional reference lattice extrapolated from a non-distorted region of the material to the experimental one, built up from the set of intensity maxima in the HRTEM image. Fig. 3.3a summarizes the procedures involved in the so called peak-finding methods by using Lattice Distortion Analysis (LADIA) [6,7] as an example. The detection limit for displacements from HRTEM images is seriously influenced by the noise coming from an amorphous surface layer. For noise reduction, besides Bragg- and band-pass filters, the Wiener filter has been found to be the most efficient. The Wiener filter is a type of linear filter that is applied to an image adaptively, tailoring itself to the local image variance, and preserving edges and other high frequency parts of the image, assuming Gaussian white additive noise. In order to define the positions of the intensity peaks, a cross-correlation factor (XCF) calculation [8] was performed between the experimental micrograph and a template motif. Here, the template motif is created by averaging over 20 single motifs which are chosen from an undistorted region in the micrograph.

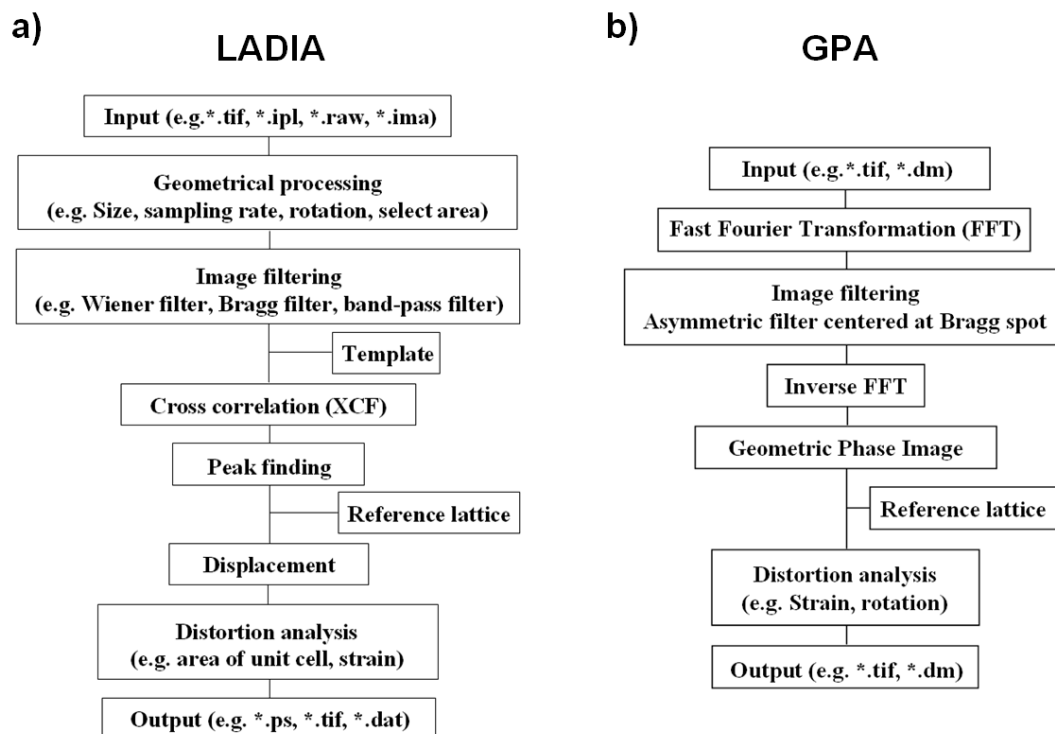


Fig. 3.4: Outline of two image processing algorithms for quantitative distortion analysis from HRTEM images: (a) Lattice Distortion Analysis (LADIA), (b) Geometric Phase Analysis (GPA).

The cross-correlation function (XCF) of the experimental image and the template is calculated at each pixel position r_{pq} :

$$\Phi(r_{pq}) = \sum_i \sum_j [I_{ima}(r_{ij} - r_{pq}) - \langle I_{ima} \rangle] \cdot [I_{temp}(r_{ij}) - \langle I_{temp} \rangle], \quad (3.9)$$

where I_{ima} and I_{temp} are the intensities of the image and the template, respectively, and $\langle I_{ima} \rangle$ and $\langle I_{temp} \rangle$ are their mean values. The subtraction of the mean values substantially removes the influence of slow variations of the background intensity on the XCF. To calculate the displacement of every intensity peak, lattice fitting should be used firstly in a selected distortion-free region. The peaks of the XCF are used to calculate a regular lattice (reference lattice), $R_{u,v}$, by a least square fitting procedure [9]:

$$R_{u,v} = R_{0,0} + ua_0 + vb_0, \quad (3.10)$$

where $R_{0,0}$ is the origin of the reference lattice, a_0 and b_0 are the base vectors and u and v are the indices of the reference lattice points. The reference lattice is extrapolated over the entire image and all intensity peaks $R'_{u,v}$ are indexed. The displacement of every peak position from its extrapolated position can be calculated as (Fig 3.3),

$$\Delta R_{u,v} = R'_{u,v} - R_{u,v}. \quad (3.11)$$

The strain along any direction (m, n) can be calculated as

$$\varepsilon_{u,v} = \left| R_{u+m,v+n} - R_{u,v} \right| / \left| ma_0 + nb_0 \right|. \quad (3.12)$$

Fig 3.5 shows the HRTEM image of the whole Si/SiGe hetrostructure along the [110] zone axis and the corresponding two dimensional out-of-plane strain, ε_{yy} , map. The value of the maximum strain within the $\text{Si}_{1-x}\text{Ge}_x$ layer (given as isolines in Fig 3.5b) reaches (1.73 ± 0.20) %. Taking the experimentally measured in-plane strain, ε_{xx} , of (0.02 ± 0.20) % into account, the tetragonal strain state of the hetrostructure is lower than the theoretical predictions ($\varepsilon_{yy}^{bulk} = 2.21$ % with respect to

unstrained Si, calculated using elastic constants given in Table 1), which might be attributed to the thin foil relaxation of the TEM specimen.

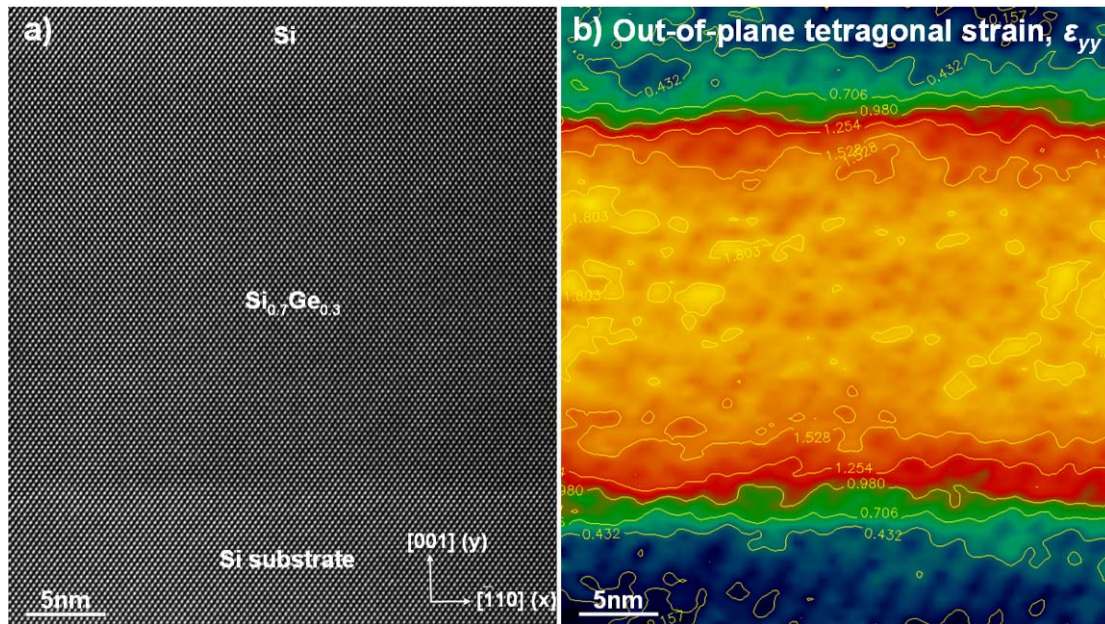


Fig. 3.5: (a) [110] HRTEM image of the Si/SiGe heterostructure. (b) Tetragonal out of plane strain measured using peak finding algorithm LADIA.

3.4 Strain mapping using Geometric Phase Analysis

Another approach to measure displacements in HRTEM images is based on geometric phase analysis (GPA) [10,11], which operates in reciprocal space, analyzes the spatial frequency phase shift, and expresses the lattice distortions in terms of this shift. If we consider the periodic fringe image with periodicity $1/|\vec{g}|$ in \vec{g} direction, the image contrast can be represented as the Fourier series:

$$I(\vec{r}) = \sum_{\vec{g}} H_{\vec{g}} e^{(2\pi\vec{g}\cdot\vec{r})}, \quad (3.13)$$

where $I(\vec{r})$ is the image intensity at a point \vec{r} , \vec{g} are the spatial frequencies corresponding to the Bragg reflections, and $H_{\vec{g}}$ are the Fourier coefficients. The complex values $H_{\vec{g}}$ can be expressed as:

$$H_{\vec{g}} = A_{\vec{g}} e^{(iP_{\vec{g}})}, \quad (3.14)$$

where $A_{\vec{g}}$ is the amplitude of the sinusoidal periodic contrast corresponding to planes \vec{g} and $P_{\vec{g}}$ determines the phase shift of this sinusoid with respect to the reference point. In the presence of variations in the lattice periods, the Fourier coefficients depend on the coordinate \vec{r} . The symmetric Fourier components of a real image (e.g. $H_{\vec{g}}$ and $H_{-\vec{g}}$) are complex-conjugates of each other, so the contrast for each system of planes \vec{g} can be described as:

$$I_{\vec{g}}(\vec{r}) = 2A_{\vec{g}}(\vec{r}) \cdot \cos(2\pi\vec{g}\vec{r} + P_{\vec{g}}(\vec{r})). \quad (3.15)$$

$H_{\vec{g}}(r)$ in reciprocal space represents the distribution of the complex scattering factor around the corresponding reflection \vec{g} and can be extracted by inverse Fourier transformation as:

$$H_{\vec{g}}(\vec{r}) = FT^{-1} \left[H_{\vec{g}}(\vec{k}) \otimes (\vec{k} - \vec{g}) \cdot M(\vec{k} - \vec{g}) \right]. \quad (3.16)$$

where, \vec{k} is the current vector in reciprocal space and $M(\vec{k} - \vec{g})$ is a mask in reciprocal space. The field $P_{\vec{g}}(\vec{r})$ of phase shifts can be interpreted as a field of displacement, $u(r)$

$$P_{\vec{g}}(\vec{r}) = P_0 - 2\pi\vec{g} \cdot u(\vec{r}). \quad (3.17)$$

If the term P_0 is constant (note that P_0 is only constant if the thickness, composition, and orientation of the sample do not change), the local strain, which is the derivative of the displacement, can be calculated from $P_{\vec{g}}(\vec{r})$ as follows:

$$\frac{\partial u(\vec{r})}{\partial \vec{r}} = -\frac{1}{2\pi\vec{g}} \frac{\partial P_{\vec{g}}(\vec{r})}{\partial \vec{r}}. \quad (3.18)$$

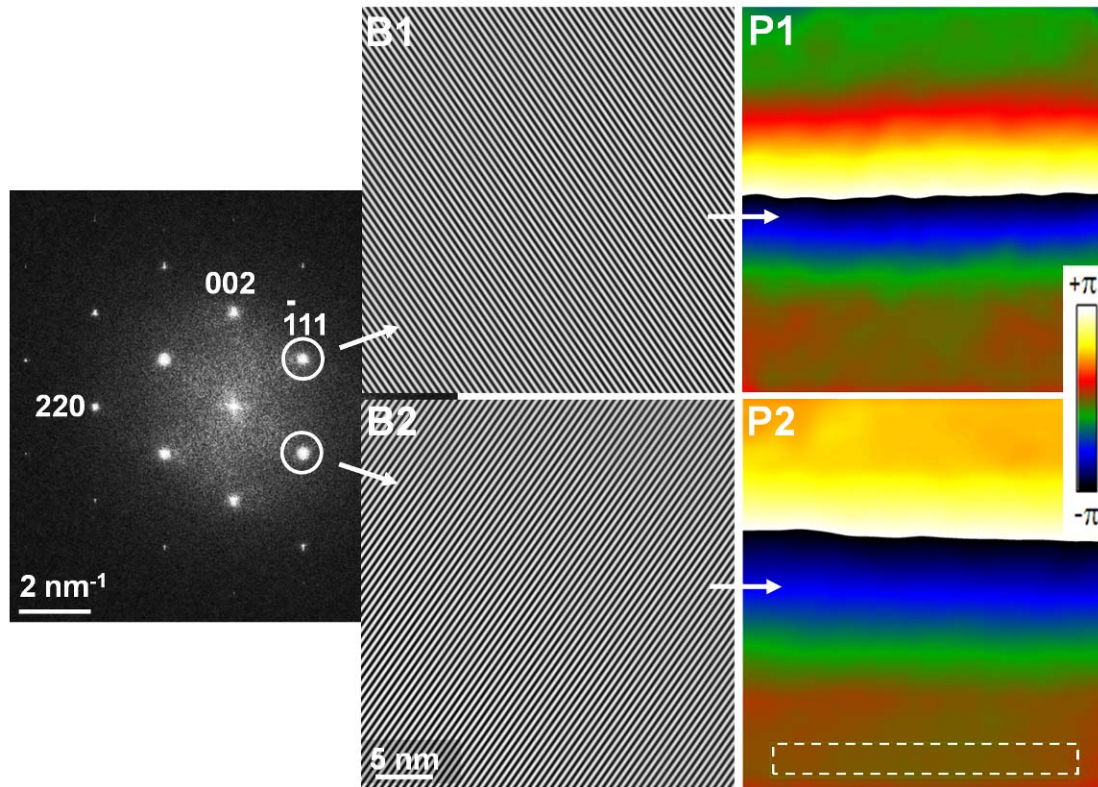


Fig. 3.6: Flow of geometric phase reconstruction process as an example demonstrated for Si/SiGe interface in [110] orientation: The diffractogram is calculated by Fourier transform of the HRTEM image (from Fig 3.5 (a)). Two non-linear Bragg reflections (in this case, $\langle 111 \rangle$ reflections) are selected by applying a mask. The isolated reflections are moved to the center and the inverse Fourier transform is applied. The resulting periodic lattice fringe images and the corresponding phase shift of the periodicity are given in B1-B2 and P1-P2, respectively.

The flowchart in Fig 3.4(b) outlines the main steps of the GPA algorithm, which is implemented in DigitalMicrograph (e.g. as a plug-in provided by HREM Research [12]). The diffractogram in Fig. 3.6 is computed by the Fourier transform (FFT algorithm) of the HRTEM image of the Si/SiGe heterostructure in Fig 3.5.

The Bragg reflection intensity maxima are selected for phase analysis. In this example, two $\langle 111 \rangle$ beams are selected, masks around the reflections are applied and the masked images are transferred to the center of the reciprocal space to produce the phase images. The diameter of the mask will determine the effective spatial resolution and precision. A compromise between spatial and spectral resolution must be established to obtain reliable strain information. In the current case, a Lorentzian mask of radius $|\vec{g}|/4$ was centered on the Bragg spot \vec{g} in the Fourier space. An inverse Fourier transform of the centered reflection is computed and the phase information of the transformed complex images is extracted as displayed as P1 and P2 in Fig 3.6. The two-dimensional displacement field can be determined from P1 and P2 as follows:

$$u(\vec{r}) = -\frac{1}{2\pi} [P_1(\vec{r})\vec{a}_1 + P_2(\vec{r})\vec{a}_2]. \quad (3.19)$$

where \vec{a}_1 and \vec{a}_2 are the vectors which correspond to the lattice in real space defined by the reciprocal lattice vectors \vec{g}_1 and \vec{g}_2 . The two-dimensional strain tensor, ε , given by the gradient of the displacement field can be described as follows:

$$\varepsilon = \begin{pmatrix} \varepsilon_{xx} & \varepsilon_{xy} \\ \varepsilon_{yx} & \varepsilon_{yy} \end{pmatrix} = -\frac{1}{2\pi} \begin{pmatrix} a_{1x} & a_{2x} \\ a_{1y} & a_{2y} \end{pmatrix} \begin{pmatrix} \frac{\partial P_1}{\partial x} & \frac{\partial P_1}{\partial y} \\ \frac{\partial P_2}{\partial x} & \frac{\partial P_2}{\partial y} \end{pmatrix}. \quad (3.20)$$

Fig 3.7(a) and 3.7(b) are the two main components of the strain tensor, ε_{xx} and ε_{yy} , respectively, calculated using phase images P1 and P2 following Eq. (3.20). Strain relative to the reference Si substrate is given as color-coded maps. The average in-plane strain ε_{xx} determined from the dashed box 2 in Fig 3.7(a), which represents the SiGe alloy film, is -0.02 % and its standard deviation is 0.02 %. The average ε_{xx} over the dashed box 1 in Fig 3.7(a), which represents the Si substrate, is 0 % and its standard deviation is 0.02 %. Both average values are within their standard deviations,

which means that the SiGe alloy film grew epitaxially keeping its lattice constant in the x direction equal to that of the Si substrate. The average out-of-plane strain, ε_{yy} , within the film measured from the dashed box 4 in Fig 3.7(b), is 1.71 % and its standard deviation is 0.26 %, and the ε_{yy} in the Si substrate from the dashed box 3 is measured as 0.07 % with a standard deviation of 0.20 %. As expected, a lattice mismatch in the growth direction due to the tetragonal distortion of SiGe lattice was observed. However, as in the case of strain measurements by peak finding methods like LADIA, GPA showed lower values than the theoretical expectation by macroscopic elasticity theory ($\varepsilon_{yy} = 2.21$ %) [13].

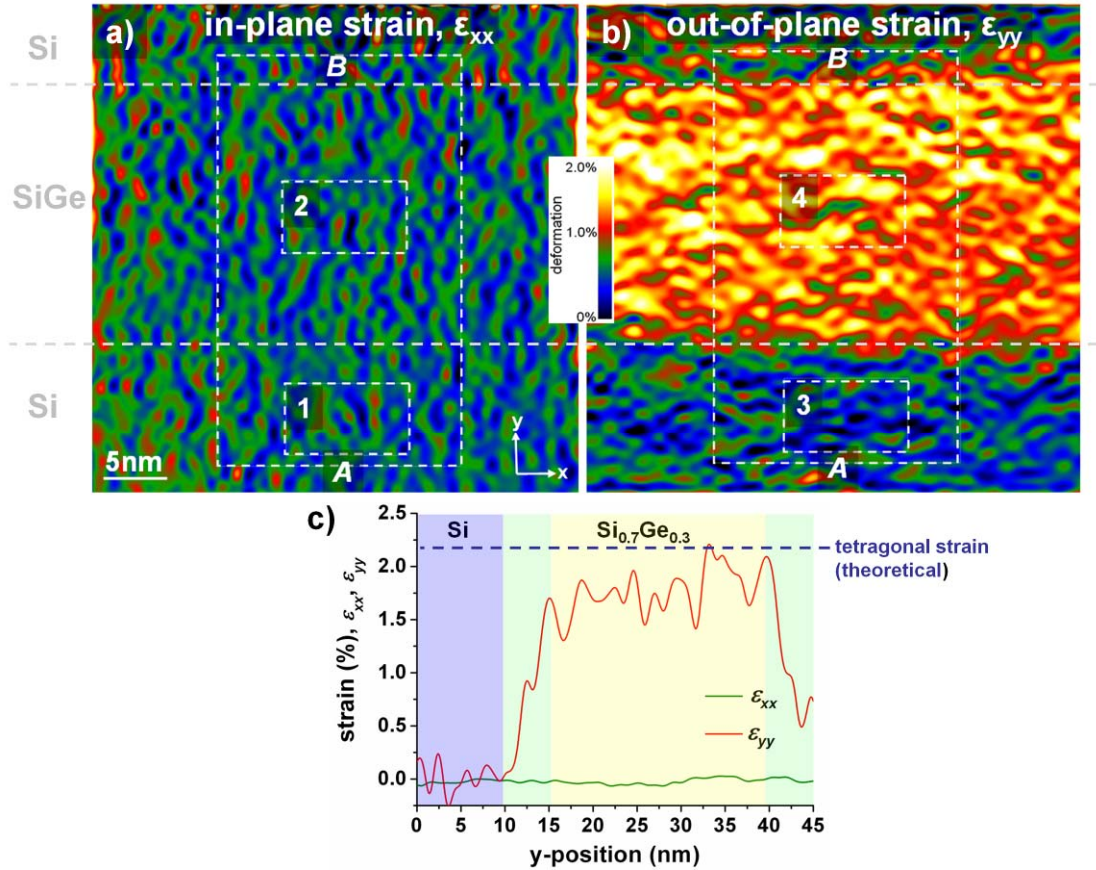


Fig. 3.7: In-plane, ε_{xx} , and out-of-plane, ε_{yy} , strain maps of a Si/SiGe heterostructure calculated by GPA are shown in (a) and (b), respectively. The spatial resolution defined by the reciprocal mask radius is 1.6 nm. (c) Integrated line scan profiles (marked as dashed rectangles in a) and b), from A to B averaged over 20 nm) across the interface are showing the strain evolution. At both interfaces a pronounced strain gradient is observed. As highlighted with green, this gradient extends over ca. 5 nm. Similar observations are reported by other authors [11]. Such gradients may arise from transients in the Ge flux and interdiffusion or segregation of Ge during the layer growth.

3.5 Geometric Phase Analysis for a complex-valued exit face wave function

Although GPA is an efficient approach to measure displacements, it relies on the assumption that the positions of the maxima and minima in the HRTEM image are not displaced by the aberrating contrast transfer function of the microscope. Errors may result when strain gradients are present and when gradient of the aberration function is non-zero, $\nabla\chi \neq 0$, for the spatial frequency used for the analysis [14]. The errors can be minimized by following some experimental guidelines such as [15]:

- avoiding regions where the fringe contrast changes rapidly;
- analyzing centrosymmetric or symmetry-related reflections;
- choosing conditions (thickness and defocus) where the fringe contrast is maximal, to reduce the effective lens transfer function;
- carrying out the analysis at different defocus values.

Fig. 3.8 shows HRTEM images of the Si/SiGe interface ([011] zone axis) acquired at different defocus values (enlargements are shown as subset images) using the Zeiss SESAM microscope equipped with a 200 keV FEG. The effect of defocus variations on the measured strain values is investigated using a script implemented in DigitalMicrograph, based on the original publication by Hytch et al [13]. The line profiles in Fig. 3.9(e) display the measured tetragonal strain across the interface obtained from a series of images acquired at different defocus values ranging from -80 nm to 60 nm. Spurious strain fluctuations are observed at the interface, which might be misinterpreted as compressive strain reaching up to 1%.

It is not straightforward to analyze the effect of the gradient of the aberration function on the strain maps obtained from HRTEM images using GPA. The lateral displacement of the spatial frequencies in the image due to the spherical aberration of the objective lens increases strongly with the spatial frequency. The effect is rarely a problem on LaB₆ instruments due to their limited coherence. However, on FEG instruments like SESAM ($C_s=1.2$ mm), with their high coherence resulting in a strong contribution of high spatial frequencies, this effect is quite pronounced. Depending on the spatial frequencies transferred and the defocus, the delocalization at the interface can be up to several nanometers [16]. From an experimental point of view, the

accuracy of GPA mainly depends on the signal to noise ratio, but not on the spatial resolution of the HRTEM image. For the Si/SiGe structure, it is sufficient to resolve the (111) planes by choosing an appropriate size for the objective aperture. In the case of 7-beam imaging, for which only the undiffracted beam \bar{g}_0 and the six first-order diffracted beams $\pm \bar{g}_1$ contribute to the image intensity, not only the extension of delocalization can be minimized, but also the non-linear image contributions are reduced.

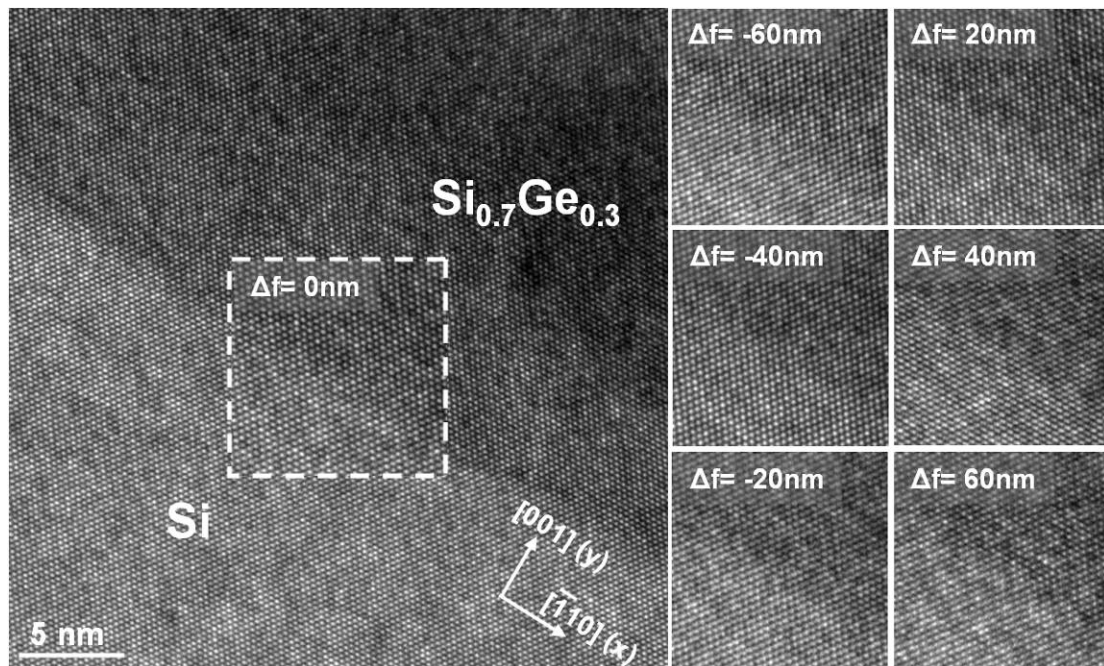


Fig. 3.8: HRTEM images of the Si/SiGe interface ([011] zone axis) acquired at different defocus values (enlargements are shown as subset images) using the Zeiss SESAM microscope equipped with 200 keV FEG.

An alternative approach to minimize the artifacts arising from the aberrated wave function is to reconstruct the exit-face wave function $|\Psi_0(\vec{r})|$ from a focal series of HRTEM images and apply the GPA directly to the wave function. The GPA analysis of HRTEM images may only retrieve the difference between the geometric phase and the phase of the central beam and is therefore strongly affected by variations in the sample thickness and the mean inner potential. To overcome this, a modified version of the GPA-algorithm has been implemented in DigitalMicrograph which can handle complex wave functions (see reference [17]). The full resolution exit-wave reconstruction (FRWR) [18] software is used for the reconstruction. The algorithm relies on the solution of a set of non-linear equations describing the image

formation by propagating between the specimen exit surface image plane at $\Delta f = 0$ and the focal planes at which the images have been recorded. During each iteration, estimates of the wave functions at the different focal planes are made by replacing the wave function amplitude $|\Psi_{\Delta f}(\vec{r})|$ with the experimental image amplitude $\sqrt{I(\vec{r})}$. The wave function in the exit surface plane is then estimated by a weighted average [19] of the wave functions back-propagated from the different focal planes to $\Delta f = 0$.

Precise image alignment is necessary prior to reconstruction because no microscope can record a series of 10-20 HRTEM images without mechanical drift between the images. The initial alignment of the images is performed manually between successive images, which is only a rough alignment because the contrast of the images in the focal-series is changing due to the defocus change. Therefore, the alignment is refined in each iteration step by calculating the relative image shift vector (\vec{r}') minimizing the square of the Euclidian distance between two images:

$$\begin{aligned}\xi^2(\vec{r}') &= \sum [I_{\text{exp}}(\vec{r} + \vec{r}') - I_{\text{sim}}(\vec{r})]^2 \\ &= -2I_{\text{exp}}(-\vec{r}) \otimes I_{\text{sim}}(\vec{r}) + \sum I_{\text{exp}}(\vec{r})^2 + \sum I_{\text{sim}}(\vec{r})^2\end{aligned}\quad (3.21)$$

where the minimum of $\xi^2(\vec{r}')$ occurs at the same relative shift as the maximum of the cross correlation $I_{\text{exp}}(-\vec{r}) \otimes I_{\text{sim}}(\vec{r})$ of the images $I_{\text{exp}}(\vec{r})$ and $I_{\text{sim}}(\vec{r})$.

The flux-preserving reconstruction algorithm updates the wave function amplitudes via weighing the spatial frequency components of the update by the strength by which they appear in the experimental image. The iteration is done through the following loop by [18]:

- propagating the estimate of the exit wave function to each of the n focal planes with defocus Δf_n according to:

$$\Psi_{\Delta f}(\vec{r}) = FT^{-1}[\Psi_0(\vec{q}) \exp(-i\chi(q, \Delta f))]\quad (3.22)$$

- estimating $\Psi'_{\Delta f_n}(\vec{r})$ at each focal plane by updating the wave function amplitude using the following steps:

$$I_{\Delta f}^{\text{sim}}(\vec{r}) = |\Psi_{\Delta f}(\vec{r})|^2 \otimes E_s(\vec{r}, \Delta f)\quad (3.23)$$

where $I_{\Delta f}^{sim}(\vec{r})$ and $E_s(\vec{r}, \Delta f)$ are the simulated image intensity and spatial coherence envelope function, respectively.

$$d\Psi_{\Delta f}(\vec{r}) = \sqrt{I_{\Delta f}^{exp}(\vec{r})} - \sqrt{I_{\Delta f}^{sim}(\vec{r})} \quad (3.24)$$

$$\Psi'_{\Delta f}(\vec{r}) = \left[|\Psi_{\Delta f}(\vec{r})| + d\Psi_{\Delta f}(\vec{r}) \right] \Psi_{\Delta f}(\vec{r}) / |\Psi_{\Delta f}(\vec{r})| \quad (3.25)$$

- obtaining a new estimate of the exit surface wave function by computing a weighted average of the back-propagated $\Psi'_{\Delta f}(\vec{r})$. The back-propagation is done by multiplying the wave function in reciprocal space with the complex conjugate of the contrast transfer function (CTF), $\exp(-i\chi(q, \Delta f_n))$. Each of the back-propagated wave functions is weighted by the corresponding envelope function $E_s(q, \Delta f_n)$ when determining the new estimate for the exit surface wave function.

Fig 3.9(a) displays the average-weighted complex-valued exit wave image reconstructed from a focal series of HRTEM images (a subset is shown in Fig 3.8). Unlike in GPA, where the diffractogram is obtained via FFT of the HRTEM image, the reconstructed diffraction pattern shown in Fig 3.9(b) allows not only to identify the local crystal tilt but also to minimize the excitation error. As marked in Fig 3.9(b), $\langle 111 \rangle$ reflections were selected using a circular mask with the size corresponding to 1.6 nm spatial resolution. A cosine function which produced a gradual transition of the mask value from 1 to 0 within the outer 20% of the mask radius was used for smoothing the edges of the circular masks. The resulting in-plane and out-of-plane strain maps are displayed in Fig 3.9(c) and 3.9(d), respectively. The average ε_{xx} from dashed box 1 in Fig 3.9(c), which represents the Si substrate, is 0 % and its standard deviation is 0.05 %. Both average values in 1 and 2 are within their standard deviations. The average out-of-plane strain, ε_{yy} , within the film measured from the dashed box 4 in Fig 3.9(d), is 1.83 % and its standard deviation is 0.13 %, and the ε_{yy} in the Si substrate from dashed box 3 is measured as 0.01 % with a standard deviation of 0.14 %. The integrated profiles ε_{xx} and ε_{yy} (from A to B and C to D, respectively) shown in Fig 3.9(f) do not only reveal the artifact-free strain evolution across the interface, but also provides higher precision compared to the strain profiles acquired

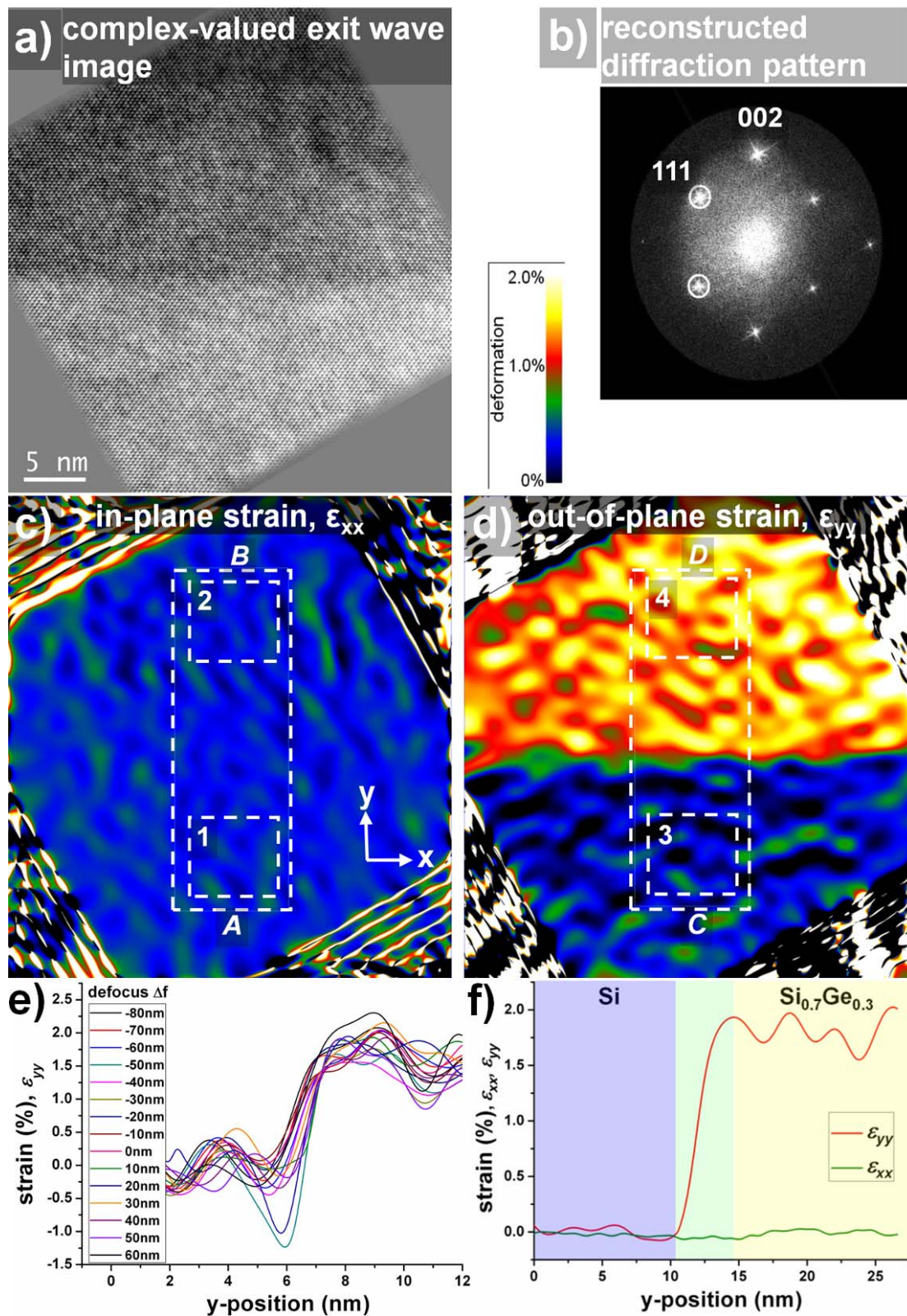


Fig. 3.9: (a) Complex-valued exit-face wave image and, (b) diffraction pattern reconstructed from focal series of 15 HRTEM images (defocus values were refined by the reconstruction algorithm resulting in a mean defocus step of 7.92 nm). (c) In-plane and, (d) out-of-plane strain maps calculated using $\langle 111 \rangle$ reflections. Strain profiles obtained from (e) HRTEM images at different defocus values and, (f) complex-valued exit-face wave image.

from each HRTEM images at different defocus planes (Fig 3.9(e)), due to the increased signal-to-noise ratio in the reconstructed exit wave image.

3.6 Comparison of the methods

Both LADIA and GPA approaches are based on the same assumption that phase shift between intensity maxima and atomic positions is zero or constant. Image information from many beams is used for displacement measurements based on LADIA, whereas only two reflections are required for analysis based on GPA. Different pairs of reflections can be used and compared for the validity of the measurement. In GPA, global averaging in reciprocal space is used for the noise reduction. The reference area has to be chosen very precisely. In reciprocal space, the determination of Bragg peak positions may have large error mainly due to averaging of the information from reference and strained areas. On the other hand, in LADIA noise reduction can be made in real space, which enables to measure localized displacements such as in sharp interfaces. Using only local information in Fourier space, compared to LADIA, GPA is affected less from the lens aberrations. In the presence of defects in the region of interest, GPA is more convenient to apply, since LADIA requires defect free periodic or nearly periodic structure. GPA on complex-valued exit face wave function can be used to reduce the artifacts arising from aberrations of objective lens. However, the method suffers from the necessity for highly stable experimental conditions and/or focal series reconstruction algorithm which can handle complex image alignment as well as non-linear image formation.

For the Si/SiGe structure investigated here, the average out-of-plane strain values are measured as (1.73 ± 0.2) % for LADIA and (1.71 ± 0.26) % for GPA. The minor difference is still within the precision windows of the two methods. This difference may result from averaging procedures (the size and the position of the box used for averaging). Such deviations may also result from the difference of size and the position of the reference area. For GPA, this depends on the precision in centering the reciprocal mask on the reflection of interest. For LADIA analysis, it depends on the precision in determination of the unit cell vectors and precision in fitting of positions of the maxima in XCF. GPA analysis on the complex-valued exit wave function revealed (1.83 ± 0.13) % average out-of-plane strain within the SiGe layer. Although the measured values are higher compared to those obtained by LADIA and GPA, they are still lower than the predicted by elastic calculations (2.21 %).

It is unlikely that these low values result from incorrect measurements of deformation as the system investigated here presents ideal conditions for strain mapping using LADIA or GPA. Imaging artifacts are minimized for centrosymmetric crystals [11], the lattice fringe spacings analyzed are much larger than the point-to-point resolution of the microscopes ($d_{111}^{Si} = 0.314$ nm, point-to-point resolution: 0.20 nm for SESAM, 0.17 nm for JEOL 4000EX and 0.12 nm for JEOL-ARM1250). Indeed, the precision (in deformation maps at 1.6 nm spatial resolution) in GPA on reconstructed exit wave function is 0.13 % which is much higher than average precision obtained in GPA on single lattice images thanks to the improved signal-to-noise ratio from focal series reconstruction (see Fig 3.9 e) and f) for comparison). The reason for the low value of measured strain is most probably due to the specimen preparation prior to HRTEM investigation.

Two free surfaces introduced during specimen preparation relax the stresses and hence modify the strain state with respect to the bulk [20,21]. In the case of very thin sample, one should consider the plane stress conditions rather than plane strain [22]. The important parameter to consider is the ratio of the strained film thickness to the specimen thickness. For example, the strain measured by GPA of 2.5 nm thick InGa_N quantum wells (see Chapter 5 for the details) has been shown closer to that of a bulk specimen. However, the SiGe film investigated here has a layer thickness of (27 ± 0.5) nm (estimated from the contrast in HRTEM image shown in Fig 3.5(a)), which is probably greater than the specimen thickness. Recent CBED analyses on very similar but thicker samples indeed show that as the specimen thickness becomes smaller, the measured deformation values approach those of expected in plane stress conditions [23]. According to the finite element modeling (FEM) results [23], in the limit the strain would be 1.7 % (with respect to Si lattice) in the SiGe layer which corresponds to the measured value by GPA and LADIA (for a detailed FEM analysis on similar Si/SiGe heterostructures see Ref. [13])

The accurate measurement of strain relies on the knowledge of the local composition at the region of interest. In the presence of compositional variations which change the size and the shape of the lattice unit cell, the undeformed state of the SiGe lattice is not the same everywhere. Both LADIA and GPA (see strain profile in Fig 3.7(c)) revealed strain gradients over ca. 5 nm. Even for GPA on complex exit wave function, where the minimization of objective lens distortions ensures the

imaging of interfaces without broadening, strain gradients extending over 4 nm (Fig 3.9(f)) were observed at spatial resolution of 1.6 nm. Such strain gradients may arise from transient in the Ge flux and interdiffusion or segregation of Ge during the layer growth. Similar observations are reported on SiGe islands [24] and SiGe films [11] grown on Si substrate.

References:

- [1] J. Zou, and D. J. H. Cockayne, in *Progress in Transmission Electron Microscopy 2*, Springer, Berlin (2000).
- [2] C. G. Van de Walle, *Band lineups and deformation potentials in the model-solid theory*, Phys. Rev. B **39**, pp. 1871-1883 (1989).
- [3] C. G. Van de Walle, and R. M. Martin, *Theoretical calculations of the heterojunction discontinuities in the Si/Ge system*, Phys. Rev. B **34**, pp. 5621-5634 (1986).
- [4] E. Kasper, *Properties of strained and relaxed Silicon Germanium*, the Institution of Electrical Engineers, London (1995).
- [5] J.C.H. Spence, in *High-Resolution Electron Microscopy*, Oxford University Press, Oxford, (2003).
- [6] K. Du, Y. Rau, N. Y. Jin-Phillipp, F. Phillipp, *Lattice distortion analysis directly from high resolution transmission electron microscopy images: The LADIA program package*, J. Mater. Sci. Tech., **18/2**, pp. 135-138 (2002).
- [7] K. Du, F. Phillipp, *On the accuracy of lattice-distortion analysis directly from high-resolution transmission electron micrograph*, Journal of Microscopy, **221/1**, pp. 63-71 (2006).
- [8] J. Frank, in *Computer Processing of Electron Microscope Images*, Springer, Berlin, pp. 187-222 (1980).
- [9] W.H. Press, S.A. Tenolsky, W.T. Veterling, and B.P. Flannery, in *Numerical Recipes in Fortran*, Cambridge University Press, Cambridge, (1992).
- [10] M. Hýtch, E. Snoeck, R. Kilaas, *Quantitative measurement of displacement and strain fields from HREM micrographs*, Ultramicroscopy, **74/3**, pp. 131-146 (1998).
- [11] M. Hýtch, F. Houdellier, *Mapping stress and strain in nanostructures by high-resolution transmission electron microscopy*, Microelectronic Engineering, **84/3**, pp. 460-463 (2006).
- [12] <http://www.hremresearch.com/> (21.04.2011).
- [13] F. Hue, M. Hýtch, H. Bender, J.M. Hartmann, and A. Claverie, *Strain measurements in s-Si/SiGe nanostructures by quantitative high-resolution electron microscopy*, Mater. Res. Soc. Symp. Proc., **1026**, pp. C20-04 (2008).

- [14] J. Chung and L. Rabenberg, *Effects of strain gradients on the strain measurements using geometrical phase analysis in the transmission electron microscope*, Ultramicroscopy, **108**, pp. 1595-1602 (2008).
- [15] M. Hýtch and T. Plamann, *Imaging conditions for reliable measurement of displacement and strain in high-resolution electron microscopy*, Ultramicroscopy, **87**, pp. 199-212 (2001).
- [16] C. Kübel, A. Thust, in *TrueImage: Introduction to Focal-Series Reconstruction* in Nato Science Series E, Kluwer Academic Publishers, Dordrecht, p. 373 (2005).
- [17] <http://www.christophkoch.com/strain/index.html> (21.04.2011)
- [18] C. T. Koch, *A flux-preserving inline electron holography reconstruction algorithm for illumination of partial spatial coherence*, Ultramicroscopy, **108**, pp. 141-150 (2008).
- [19] S. Bhattacharyya, C.T. Koch, M. Rühle, *Potential profiles across interfaces obtained by exit face wave reconstruction of Fresnel through focal series*, Ultramicroscopy, **106**, pp. 525-538 (2006).
- [20] M. M. Treacy, J. M. Gibson, and A. Howie, *On elastic relaxation and long wavelength microstructures in spinodally decomposed InGaAsP epitaxial layers*, Philos. Mag., **51**, pp. 389-417 (1985).
- [21] S. Kret, P. Ruterana, A. Rosenauer, and D. Gerthsen, *Extracting quantitative information from high resolution electron microscopy*, phys. stat. sol. (b), **227**, pp. 247-295 (2001).
- [22] J. P. Hirth, J. Lothe, in *Theory of dislocations*, second ed., Krieger, Malabar Florida (1992).
- [23] F. Houdellier, C. Roucau, L. Clement, J. L. Rouviere, and M. J. Casanove, *Quantitative analysis of HOLZ line splitting in CBED patterns of epitaxially strained layers*, Ultramicroscopy, **106**, pp. 951-959 (2006).
- [24] W. Neumann, H. Kirmse, I. Häusler, and R. Otto, *Quantitative high resolution transmission electron microscopy of nanostructured semiconductors*, Journ. of Microsc., **223**, pp. 200-204 (2006).

Chapter 4

An efficient, simple and precise way to map strain with nanometer resolution in semiconductor devices

Abstract:

The development of the dark-field electron holography technique and its application to map strain in strain-engineered gate channel in a 45 nm p-MOSFET structure is presented. The technique combines a large field of view of several μm with high precision (better than 0.01 %), high spatial resolution (better than 1 nm), and very loose experimental requirements not possible with any other technique currently available.

4.1 Introduction

The ability to measure local strain on the nanometer scale is an essential tool for characterizing modern nanostructured materials. Local stress fields affect materials mechanical and electronic properties, may induce diffusion, or control mass transport during growth, being responsible, for example, for self-organisation and growth of quantum dots. Strain-induced alteration of the band structure in semiconductors is being utilized for increasing the mobility of charge carriers in modern MOSFET and DRAM structures and with that the device performance [1,2]. Being able to map strain with high spatial resolution and a large field of view of at least 1 μm is therefore crucial for developing modern microelectronic devices. In this chapter, a simple method is presented for measuring the 2-dimensional strain tensor with high precision, a large field of view, and better than 1 nm spatial resolution. This method can be applied on any standard TEM and minimizes electron dose on the investigated specimen [3].

Among all kinds of radiation being used to measure strain, i.e. neutrons [4], X-rays [5], electrons [6-10], or light [11], electron scattering based techniques, because of the small wavelength and high scattering strength of electrons, and the possibility to focus them into small volumes, offer the highest spatial resolution. Within the field of electron scattering techniques applied for strain mapping, real-space methods relying on the analysis of the phase shift of scattered electron wave functions, namely the geometric phase analysis of HRTEM images [9] or dark-field off-axis holography (DOAH) [10,12], offer generally a higher spatial resolution than methods analyzing the geometric distortions in local diffraction patterns [6-8].

The dark-field inline holography (DIH) method presented in this chapter also relies on data collected in real space, but, in contrast to HRTEM-GPA or DOAH does not derive the strain information from the position of interference fringes of the scattered electron wave, but instead from variations in the intensity of dark-field TEM images with defocus. The resulting nonnecessity to sample fine interference fringes at a sufficiently high magnification allows for optimum use of the number of pixels in the detector and severely reduces the sensitivity to detector distortions which almost invariably occur in today's fiber-optically coupled CCD detectors. Also, as it will be described, in contrast to DOAH, the DIH strain mapping technique applied here has

virtually no requirements on the spatial coherence of the illuminating electron beam, making it much more widely applicable.

4.2 Experimental

Fig. 4.1 shows the experimental setup and contrast mechanism that is being made use of in DIH. Diffraction-based techniques [4-8] analyze tiny shifts in the diffraction plane (strongly exaggerated in Fig. 4.1(a)) while scanning a (small) probe relative to the sample. Such shifts in reciprocal space are caused by local lattice distortions and with that changes in scattering angle and correspond to a phase shift in real space. According to the diagram shown in Fig. 4.1(a), because of the tilted illumination the transmitted beam (\vec{k}_0) is blocked by the objective aperture located in the back-focal plane of the objective lens (diffraction plane) positioned on the optical axis of the microscope. By proper choice of the tilt angle different diffracted beams

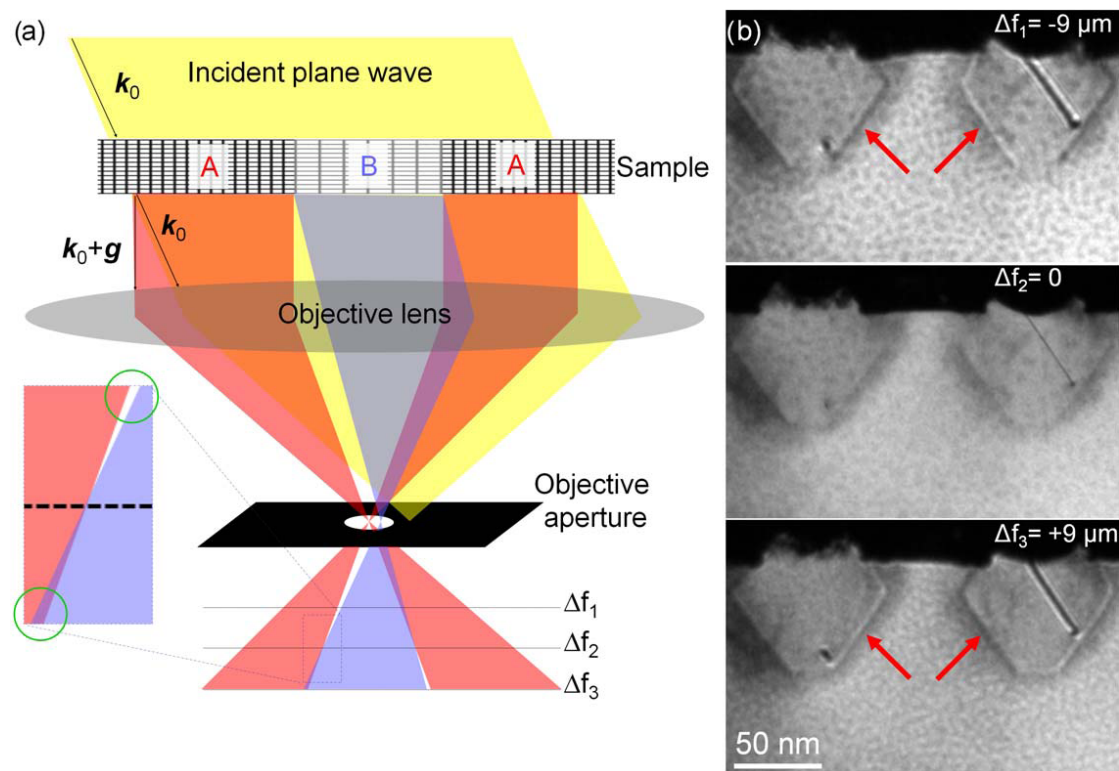


Fig. 4.1: (a) Diagram illustrating the principle of dark-field inline holography. A diffracted beam \vec{g} is selected using the objective aperture and dark-field images for at least 3 different planes of defocus ($\Delta f_1 \dots \Delta f_3$) are recorded. Lattice distortions (indicated by regions of different lattice constant A and B) lead to locally varying diffracting conditions and produce bright and dark features in places where the diffracting condition changes, as highlighted by the green circles in the inset. (b) Experimental dark-field inline holograms of a p-MOSFET structure. At the boundaries of regions of different lattice constant, i.e. SiGe (in the source and drain - see Fig. 4.2) and Si (in the substrate and also the gate channel), bright and dark bands (highlighted by red arrows) appear as illustrated in (a).

$(\vec{k}_0 + \vec{g})$ can be aligned with the optical axis of the microscope. The only difference to conventional dark-field imaging is that the images are recorded at at least 3 different planes of defocus. Fig. 4.1(b) shows subareas of 3 differently focused (220) dark-field zero-loss filtered images of a 45 nm p-MOSFET structure (see Fig. 4.2 for a bright-field image) recorded on the SESAM [13] (Carl Zeiss NTS) using a 2k x 2k fiber-optically coupled US1000 CCD camera (Gatan). The SESAM's in-column MANDOLINE filter was used for removing the contribution of inelastically scattered electrons to the recorded dark-field images. Defocus values of $\Delta f_1 = -9 \mu\text{m}$, $\Delta f_2 = 0 \mu\text{m}$ and $\Delta f_3 = +9 \mu\text{m}$ were achieved by varying the objective lens current. This task of recording a focal series is fully automated on most TEMs. An objective aperture with a diameter of $10 \mu\text{m}$ has been used to limit the resolution of these images to 0.77 nm. The in-focus ($\Delta f_2 = 0$) dark-field image provides the local intensity of the diffracted electron beam.

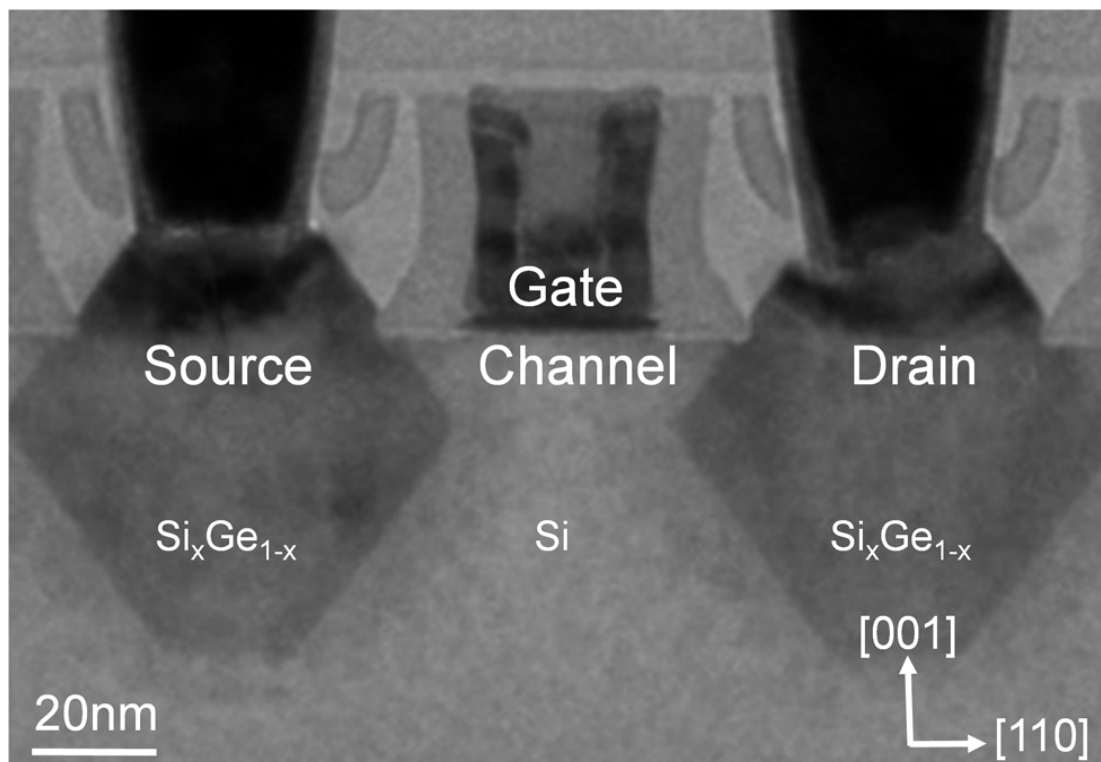


Fig. 4.2: Bright-field image of the 45nm technology p-MOSFET structure of a commercial processor used for the work presented here. The individual transistor components are labeled. The thin TEM samples have been prepared conventionally, i.e. by cutting a thin slice from a commercial processor and mechanically grinding it using a tripod polisher (AlliedTech). The resulting wedge-shaped sample was then polished using a beam of argon ions accelerated at low voltages (500 V) while cooling the sample to liquid Nitrogen temperature (Fischione, Model 1010).

4.3 Results and discussion

For small changes in defocus the corresponding phase of the diffracted electron wave function may be determined from a finite difference approximation of the transport of intensity equation (TIE) [14]

$$\begin{aligned}\nabla_{\perp}^2 \phi_{\vec{g}}(\vec{r}) &= \frac{-2\pi}{\lambda} \nabla_{\perp} \left[\frac{1}{I(\vec{r})} \nabla_{\perp} \frac{\partial I(\vec{r})}{\partial \Delta f} \right] \\ &\approx \frac{-2\pi}{\lambda} \nabla_{\perp} \left[\frac{1}{I_2(\vec{r})} \nabla_{\perp} \frac{[I_3(\vec{r}) - I_1(\vec{r})]}{\Delta f_3 - \Delta f_1} \right]\end{aligned}\quad (4.1)$$

where $I_n(\vec{r})$ is the intensity of the image at defocus Δf_n . The Fourier component of the crystal potential at the reciprocal lattice vector \vec{g} is given by

$$V_{\vec{g}} = |V_{\vec{g}}| \exp[i\phi_{\vec{g}}] = \sum f_{el}(|\vec{g}|) \exp[2\pi i \vec{g} \cdot (\vec{r} + \Delta \vec{r})] \quad (4.2)$$

In absence of variations in local composition, specimen thickness, and diffracting condition (see also [15] for a discussion of the effect of the column approximation on the phase and amplitude of diffracted beams in the context of analyzing strain fields) the phase $\phi_{\vec{g}}(\vec{r})$ of the diffracted wave function defines the geometric phase [9,10]

$$\phi_{geom}(\vec{r}) = \phi_{\vec{g}}(\vec{r}) = 2\pi \vec{g} \cdot \Delta \vec{r} + \phi_{\vec{g}}^0 \quad (4.3)$$

and may be reconstructed by inverting the 2-dimensional Laplace operator ∇_{\perp}^2 in expression (4.1). Here $\Delta \vec{r}$ is the displacement field and $\phi_{\vec{g}}^0$ is the phase of the Bragg beam for the perfect crystal. In places where the strain state of the sample changes, i.e. where variations in the strain occur:

$$\varepsilon_{i,j}(\vec{r}) = \frac{\partial \Delta \vec{r}_i}{\partial \vec{r}_j} \quad (4.4)$$

the Laplacian of the geometric phase $\nabla_{\perp}^2 \phi_{geom}(\vec{r})$ and with that the change in the image intensity with defocus are non-zero which can easily be seen by comparing the dark- field images shown in Fig. 4.1(b).

In case the change in defocus Δf between images is large, as in the case presented here, very small details in the geometric phase obtained by the TIE will not be accurately reconstructed. Therefore, a combined approach which corrects high-resolution inaccuracies in the TIE reconstruction by refining the initial TIE result using a non-linear reconstruction algorithm [16,17] is applied. This algorithm also correctly treats partial spatial coherence of the illuminating wave function. The resulting geometric phase is shown in Fig. 4.3(a). Since this approach reconstructs the phase of the diffracted wave function directly, no phase wrapping is involved, which is why the phase in Fig. 4.3(a) is presented on a gray scale of $-5\pi \dots +5\pi$.

The reconstruction of the two-dimensional strain tensor requires the geometric phase maps of two [9,10] or more [18] non-colinear reflections and has already become a standard procedure. For the pMOS transistor structure investigated in this chapter only the lateral strain component ε_{xx} along the (220) direction was of major interest because of its effect on the charge carrier mobility within the gate channel. If only a single component of the strain tensor is required, it suffices to record dark-field inline holograms only for a reflection along the direction of interest. We have therefore restricted ourselves to present here only experimental data for the (220) reflection required to reconstruct the horizontal strain component ε_{xx} , as shown in Fig. 4.3(b).

While the dark-field images used for reconstructing the strain map in Fig 4.3(b) (see Fig. 4.1(b) for sub-regions of 3 of these images) have been sampled using a pixel size of 0.58 nm (24000 times magnification at a CCD pixel size of 14 μm) the successful application of GPA of HRTEM images requires a sampling at least 10 times as fine, requiring a 100 times higher electron dose on the sample in order to achieve the same number of counts per pixel. In addition, the contrast of lattice fringes in HRTEM images is very often less than 10 % [19] which requires an even higher electron dose, in order to achieve signal-to-noise properties sufficient for producing high-precision displacement maps. The lattice-resolution HRTEM image shown in the inset in Fig. 3b has been recorded at the JEOL ARM1250 high-voltage TEM (point-to-point resolution: 0.11 nm) [20] on photographic film and was then digitized using a 2k x 2k CCD camera with a spatial sampling of 0.058 nm. The number of detector pixels was the same as for the low resolution images (2048 x 2048 pixels) so that the 10 times higher spatial sampling results in a field of view of only

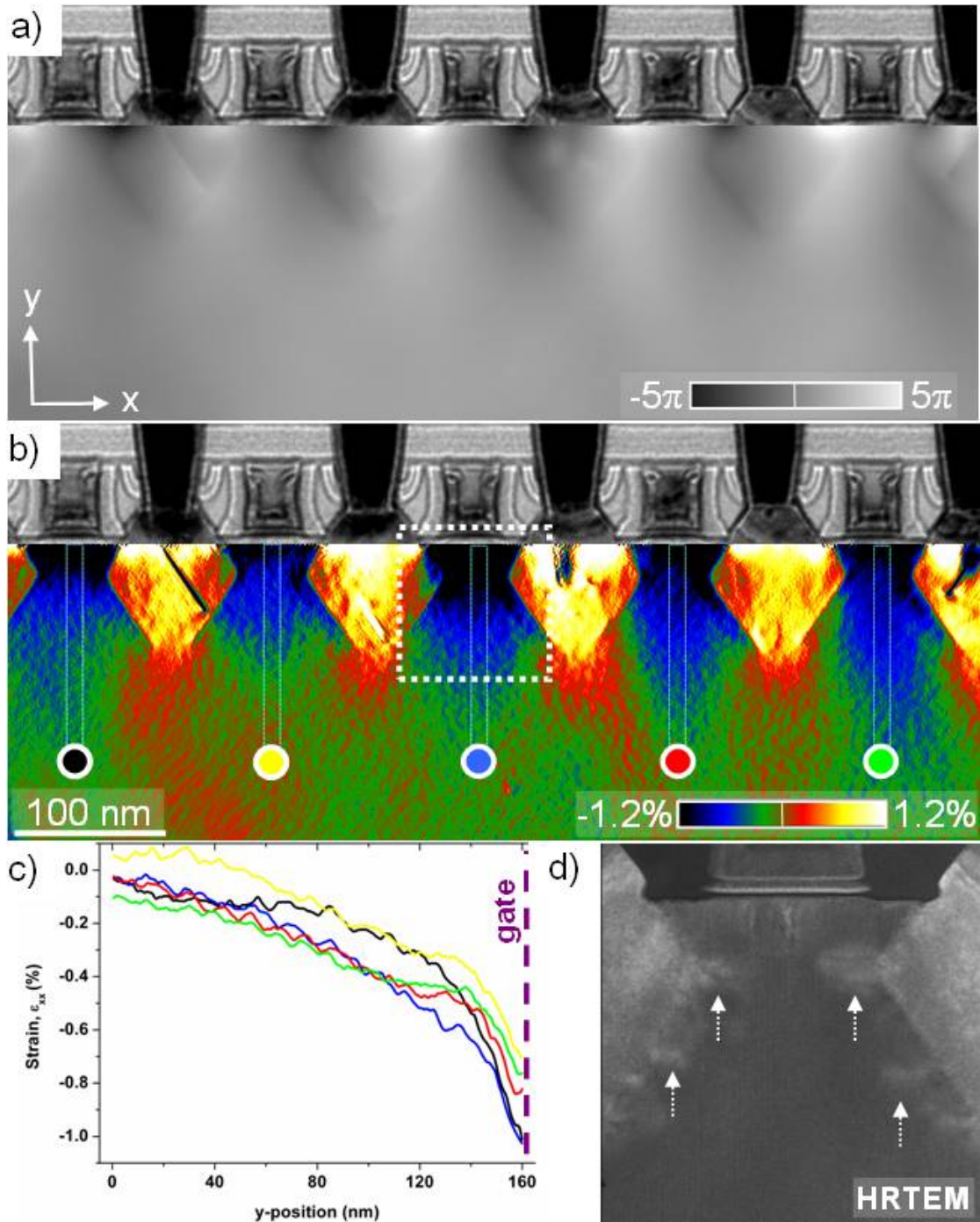


Fig 4.3: (a) Geometric phase reconstructed from a focal series of 15 dark-field inline electron holograms for the (220) reflection. The defocus step fitted by the full-resolution wave reconstruction (FRWR) software [16] was $3.98\ \mu\text{m}$. Above the phase map a bright-field image of the contacts is shown. (b) Map of the ϵ_{xx} strain component extracted from the geometric phase map shown in (a). The gate channels are compressively strained. As in (a), a bright-field image showing the electrical contacts is shown above the strain map. (c) Vertical strain profiles extracted from the narrow boxes in the ϵ_{xx} map shown in (b). The color of each plot corresponds to the color of the dot in (b) defining the line profile's origin. The profiles have been averaged across the width of the 11.7 nm (20 pixels) wide boxes shown in (b). (d) A $2\text{k} \times 2\text{k}$ pixel HRTEM image from the region marked as dashed square in (b) is recorded with the largest possible field of view ($0.1\ \mu\text{m} \times 0.1\ \mu\text{m}$) to still allow applying GPA. Dashed white arrows indicate the electron beam induced modification at the Si/SiGe interfaces.

0.1 μm x 0.1 μm , i.e. only 1/10th of that of the dark-field images. However, the strain profiles presented in Fig. 4.3(c) show that a field of view of at least 0.2 μm is necessary to include both the gate channel as well as a (narrow) reference area of undistorted perfect crystal. Also, as indicated with dashed arrows in Fig. 4.3(d), the large electron dose, aided possibly by the high electron beam energy of 1250 keV, seems to have triggered strain-induced diffusion of Ge from the source and drain into the surrounding silicon crystal. This effect could not be observed in any of the images recorded at lower magnification, demonstrating the fact that strain mapping by DIH is much more suitable for beam sensitive materials than GPA of HRTEM images.

4.4 Conclusion

While it is quite obvious that the electron dose requirements of strain mapping by DIH are much lower than for HRTEM-GPA they are also much lower than for DOAH. In addition to the much simpler experimental setup of inline holography compared to off-axis holography, the inline technique has the additional advantage of being able to freely adjust the signal-to-noise ratio independent of exposure time or illumination conditions. Since the signal is produced by variation of the image intensity with defocus, high-precision strain maps may be extracted from noisy low-dose data by choosing a large defocus step [17].

References:

- [1] "ITRS, *International Technology Roadmap for Semiconductors*, 2007 edition," <http://www.itrs.net/reports.html>.
- [2] M. Chu, Y. Sun, U. Aghoram, and S. E. Thompson, *Strain: a solution for higher carrier mobility in nanoscale MOSFETs*, *Annual Reviews in Materials* **39**, pp. 203-229 (2009).
- [3] T. M. Smeeton, M. J. Kappers, J. S. Barnard, M. E. Vickers, and C. J. Humphreys, *Electron-beam-induced strain within InGaN quantum wells: False indium "cluster" detection in the transmission electron microscope*, *Applied Physics Letters* **83**, pp. 5419-5421 (2003).
- [4] A. Krawitz and T. M. Holden, *The measurement of residual stresses using neutron diffraction*, *MRS Bulletin* **15**, pp. 57-65 (1990).
- [5] E. J. Mittemeijer and U. Welzel, *The „state of the art“ of the diffraction analysis of crystallite size and lattice strain*, *Zeitschrift für Kristallographie* **223**, pp. 552-560 (2008).
- [6] A. J. Wilkinson, G. Meaden, and D. J. Dingley, *High-resolution elastic strain measurement from electron backscatter diffraction patterns: New levels of sensitivity*, *Ultramicroscopy* **106**, pp. 307-313 (2006).
- [7] P. Zhang, A. A. Istratov, E. R. Weber, C. Kisielowski, H. He, C. Nelson, and J. C. H. Spence, *Direct strain measurement in a 65 nm node strained silicon transistor by convergent-beam electron diffraction*, *Appl. Phys. Lett.* **89**, pp. 161907-161910 (2006).
- [8] K. Usuda, T. Numata, T. Irisawa, N. Hirashita, and S. Takagi, *Strain characterization in SOI and strained-Si on SGOI MOSFET channel using nano-beam electron diffraction (NBD)*, *Mater. Sci. Eng. B* **124**, pp. 143-147 (2005).
- [9] M. Hÿtch, E. Snoeck, R. Kilaas, *Quantitative measurement of displacement and strain fields from HREM micrographs*, *Ultramicroscopy* **74/3**, pp. 131-146 (1998).
- [10] M. Hÿtch, F. Houdellier, F. Hÿe, and E. Snoeck, *Nanoscale holographic interferometry for strain measurements in electronic devices*, *Nature* **453**, pp. 1086-1089 (2008).

- [11] I. De Wolf, *Stress measurements in Si microelectronic devices using Raman spectroscopy*, Journal of Raman Spectroscopy **30**, pp. 877-883 (1999).
- [12] K.-J. Hanszen, *Method of off-axis electron holography and investigations of the phase structure in crystals*, J. Phys. D: Appl. Phys **19**, pp. 373-395 (1986).
- [13] C. T. Koch, W. Sigle, R. Höschel, M. Rühle, E. Essers, G. Benner, and M. Matijevic, *SESAM: Exploring the frontiers of electron microscopy*, Microscopy and Microanalysis **12**, pp. 506-514 (2006).
- [14] M. Teague, *Deterministic phase retrieval: a Green's function solution*, J. Opt. Soc. Am. **73**, pp. 1434-1441 (1983).
- [15] A. Howie and C. H. Sworn, *Column approximation effects in high resolution electron microscopy using weak diffracted beams*, Phil. Mag. **22**, pp. 861-864 (1970).
- [16] C. T. Koch, *A flux-preserving inline electron holography reconstruction algorithm for illumination of partial spatial coherence*, Ultramicroscopy, **108**, pp. 141-150 (2008).
- [17] C. Koch and A. Lubk, *Off-axis and inline electron holography: A quantitative comparison*, Ultramicroscopy **110**, pp. 460-471 (2010).
- [18] A. K. Gutakovskii, A. L. Chuvilin, and S. A. Song, *Application of high-resolution electron microscopy for visualization and quantitative analysis of strain fields in heterostructures*, Bulletin of the Russian Academy of Sciences: Physics **71**, pp. 1426-1432 (2007).
- [19] M. J. Hytch and M. Stobbs, *Quantitative comparison of high resolution TEM images with image simulations*, Ultramicroscopy **53**, pp. 191-203 (1994).
- [20] F. Phillipp, R. Höschel, M. Osaki, G. Möbus, and M. Rühle, *New high-voltage atomic resolution microscope approaching 1 Å point resolution installed in Stuttgart*, Ultramicroscopy **56**, pp. 1-10 (1994).

Chapter 5

A non-damaging electron microscopy approach to map In distribution in InGaN light-emitting diodes

Abstract:

Dark-field inline electron holography and, for comparison, high-resolution transmission electron microscopy are used to investigate the distribution of indium in GaN-based commercial high-efficiency green light-emitting diodes (LEDs) consisting of InGaN multi quantum wells (QWs). Owing to the low electron doses used in inline holography measurements; this technique allows to map the indium distribution without introducing any noticeable electron beam-induced damage which is hardly avoidable in other quantitative transmission electron microscopy methods. Combining the large field of view with a spatial resolution better than 1 nm, it is shown that the InGaN QWs exhibit random alloy nature without any evidence of nanometer scale gross indium clustering in the whole active region.

5.1 Introduction

The origin of the bright light emission of the InGaN LEDs has been investigated extensively during the past decade. Various experimental observations such as nanometer scale compositional fluctuations or indium clustering [1,2], gross or step-like monolayer well width variations [3,4] or quantum dot (QD) like growth [5] were supported by theoretical calculations to explain the reason for the localization of the excitons [4,6] in the InGaN epilayers of these devices. Being able to extract chemical and structural information at nanometer scale, different TEM techniques like HRTEM, Z-contrast imaging by high angle annular dark field scanning transmission electron microscopy (HAADF-STEM) as well as electron energy loss spectroscopy (EELS) and X-ray energy dispersive spectroscopy (XEDS) have been extensively exploited to reveal the structure-property relationship. Among all the proposed mechanisms mentioned above, the nanometer scale large compositional fluctuations in InGaN QWs has been controversially questioned due to the extreme sensitivity of InGaN under the electron beam doses required to realize these characterization methods [2,7]. The application of dark-field inline electron holography (DIH) is exploited to map the compositional distribution determined from the phase-map derived strain map in the active region of the LED without alteration of the original heterostructure.

5.2 Experimental

Cross-sectional TEM specimens were prepared from commercial high efficiency green LEDs by mechanical tripod polishing and low energy Argon ion milling in a L-N₂ cooled stage (accelerating voltage: 500 V, stage temperature: -160 C°) to minimize the ion beam-induced surface damage. HRTEM experiments were performed using a JEOL 4000EX operating at 400 kV to characterize the QW interfaces, well width fluctuations and to measure the local compositional variations via the strain derived from geometrical phase analysis (GPA) [8]. A two-beam condition with strongly excited (0000) and (0002) beams was used for image formation to minimize artifacts due to optical distortions in the microscope and to increase the signal-to-noise ratio at relatively low electron beam currents [1,9]. The contrast pattern in the [11-20]-zone axis of the wurtzite structure, that is frequently used for the HRTEM imaging of the nitrides, is extremely sensitive toward small variations of the imaging conditions, which reduces the area to be reliably investigated to very small extensions. Therefore, lattice fringe images were taken under two-beam conditions by only exciting the (000-2) and (0002) beams which is possible with a minimum number of other excited beams by tilting the sample about 5° out of the [1-100]-zone axis along the [11-20] direction. Delocalization contributes significantly to the phase shift of the (0002) fringes, resulting in a shift of the strain profiles extracted across the interfaces. It is therefore necessary to center the (0002) beam on the optical axis where the phase shift by the aberrated objective lens is zero independent of Δf (for a detailed analysis on the effect of the beam tilt on the image formation, see Ref. [9]). By the use of off-axis conditions, the thickness sensitivity of the contrast pattern of the images is reduced compared to conventional zone-axis HRTEM images due to an increase in extinction distances. The loss of resolution for planes perpendicular to the interface plane does not hamper the composition evaluation, which only requires the measurement of the (0002)-fringe distances.

The DIH experiments were performed using SESAM microscope (Carl Zeiss NTS) [10] equipped with a monochromated 200 kV field emission gun (FEG). The electron beam was tilted in such a way that the (0002) reflection was aligned parallel to the optical axis of the microscope. A small (diameter of 10 μm) objective aperture was used to block the undiffracted beam as well as all other reflections. The specimen

was tilted to a (0002) two-beam diffraction condition. The illumination semi-convergence angle was limited to 0.040 mrad to optimize the spatial coherence of the electron beam, which in turn decreased the electron dose rate to which the specimen was exposed. It can be shown that the signal-to-noise properties of the images by HRTEM and DIH are comparable for equal pixel size. For the optimized magnification used for the DIH experiments (31000x), the electron dose was reduced by approximately two orders of magnitude compared to the high dose HRTEM experiments (calculated values for electron dose rates in SESAM operating at 200 kV: a) in HRTEM mode, the illumination angle = 0.5 mrad, the magnification = 250000x, the electron dose rate = $2.96 \cdot 10^5$ e/nm²s; b) in DIH mode, the illumination angle = 0.03 mrad, the magnification = 20000x, the electron dose rate = $9.26 \cdot 10^2$ e/nm²s) The geometric phase images were reconstructed using the non-linear full-resolution wave reconstruction (FRWR) [11,12] algorithm. The FRWR algorithm automatically and self-consistently corrects for geometric distortions produced by large changes in the objective lens defocus. The indium distribution was obtained from the geometric phase image using an in-house developed script implemented in the DigitalMicrograph (DM) (Gatan, Inc.) software (see Appendix 1 for the DM script).

5.3 Results and discussion

An HRTEM image of the active region of the device consisting of four InGaN QWs with the GaN buffer layers is displayed in Fig. 5.1. Fig. 5.2(a) shows an HRTEM image of two 2.7 ± 0.3 nm thick InGaN QWs with well-defined defect-free interfaces from the active region as indicated by the dashed square in Fig. 5.1. The indium concentration x can be derived if the tetragonally distorted (0002) lattice spacing is known, assuming pseudomorphic growth. For the strain calculations, the

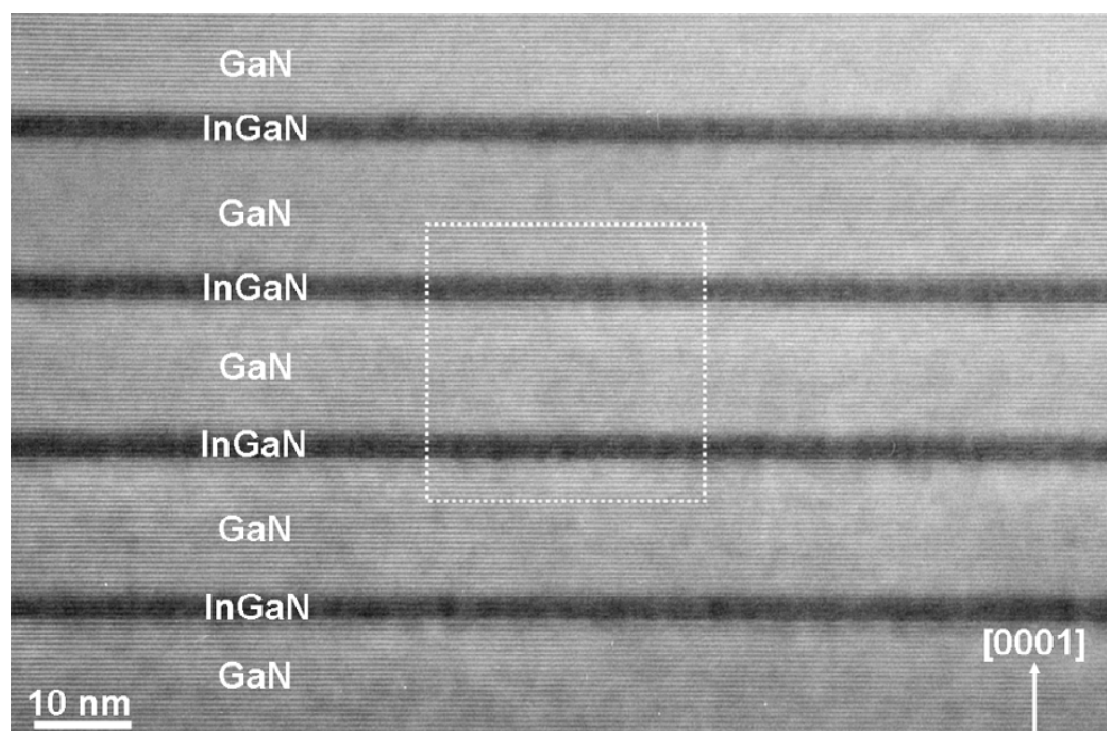


Fig. 5.1: (0002) two-beam HRTEM image showing the active region of a bright green LED, extracted from a commercial device, used for the work presented here. The active region consists of four InGaN QWs separated by GaN barrier layers. The dashed square marks the area shown in Fig. 5.2.

thick-film approximation is assumed [1]. The variation in spacing of lattice fringes has been measured by GPA by choosing only the (0002) reflection in reciprocal space, and the indium concentration shown in Fig. 5.2(b) was derived following Vegard's law, using calculated values for elastic constants [13]. The profile scans within the two QWs (Fig. 5.2(d)) revealed average indium contents of (20.1 ± 1.7) % and (21.1 ± 1.8) % without remarkable gross compositional fluctuations. The standard deviation

of the variations inside the reference area, which defines the inherent noise of the GPA is calculated as 1.3 % and is comparable with the fluctuations within the QWs.

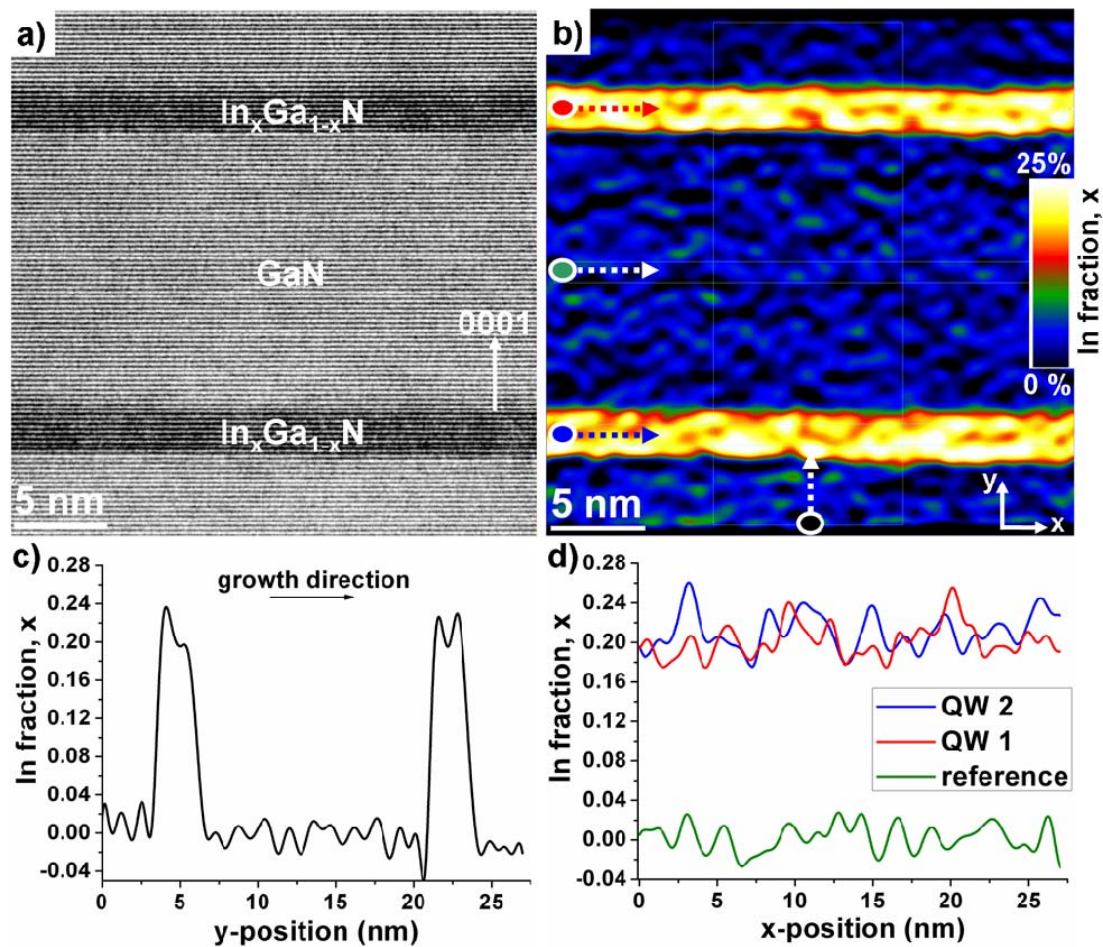


Fig. 5.2: (a) (0002) two-beam HRTEM image of the 2.7 nm thick QWs from a region represented as a dashed square in Fig. 5.1. (b) Indium distribution given as a color coded map. The resolution of the concentration map was limited to 1 nm by the Gaussian mask used for GPA. (c) Concentration profiles along the growth direction, averaged over 10 nm and (d) within the QWs and the reference GaN buffer layer averaged over a width of 1 nm.

The HRTEM image presented here was acquired within the first minute of exposure to the electron beam ($15 - 20 \text{ A cm}^{-2}$). Increasing the exposure time however, electron beam-induced modification of the specimen has been observed similar to those reported in previous studies [14,15,16]. This beam damage results in nanometer scale bending of the lattice fringes and thus localized strain modulations inside the QWs which are then interpreted as inhomogeneous indium distribution or clustering.

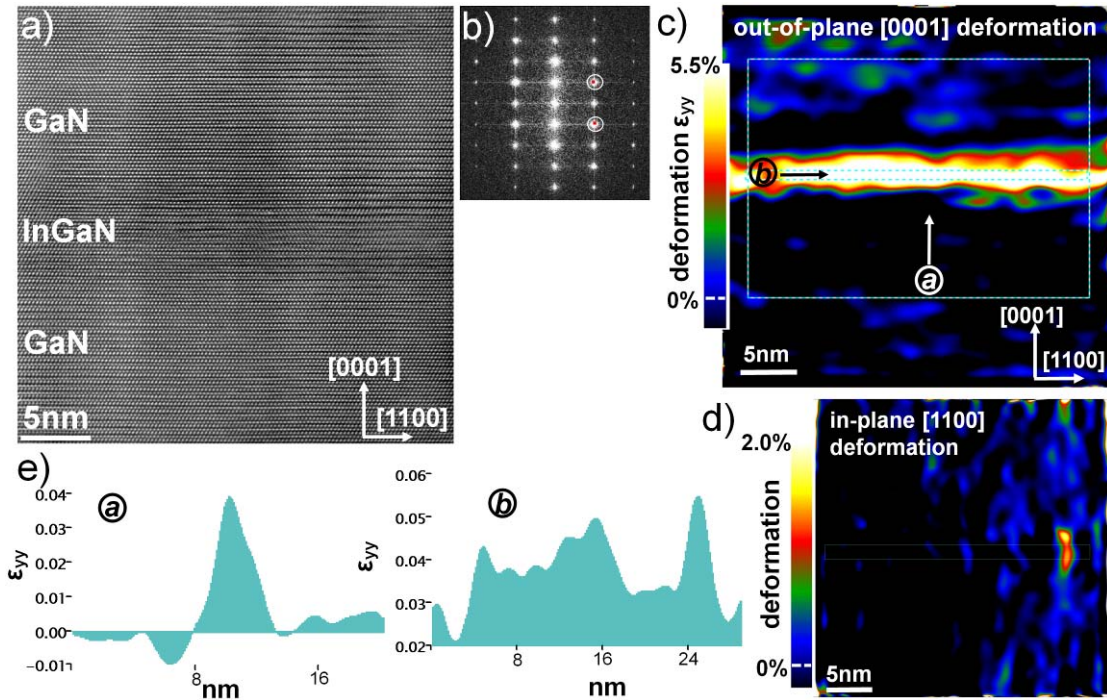


Fig. 5.3 (a) [11-20] HRTEM image of a single InGaN QW with corresponding FFT image (b). The local strain variations are obtained with GPA (resolution: 1.6 nm), using the phase images of $\{1110\}$ reflections as indicated in (b). (c) Strain mapping across the InGaN QW showing the tetragonal out of plane [0001] deformation, ϵ_{yy} , with respect to the GaN buffer layer. (d) 2D in-plane [1100] deformation, ϵ_{xx} , across the interface. (e) The averaged strain across the InGaN layer and the strain fluctuation within the layer are given as line scan profiles in the directions a and b as indicated in (c) (integration width of the profiles correspond to the width of the green boxes).

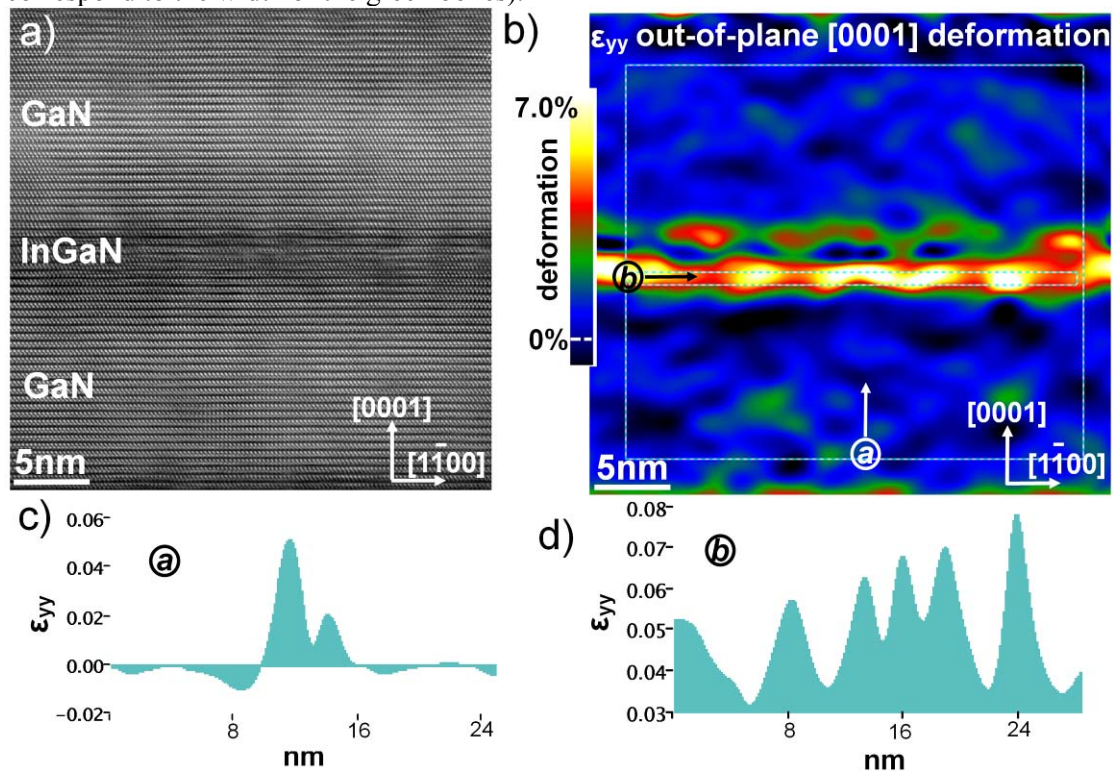


Fig. 5.4 (a) [11-20] HRTEM image and the corresponding ϵ_{yy} , out-of-plane strain map, (b). The strain across the QW and the strain fluctuations within the QW are shown in (c) and (d), respectively.

Fig. 5.3(a) shows [11-20] HRTEM image of a single InGaN QW and the GaN barriers (the power spectrum is given in 5.3(b)). The sample was prepared using FIB and the image was obtained on JEOL ARM operating at 1250kV. The out-of-plane [0001] strain, ε_{yy} , which is the only significant deformation due to the lattice mismatch, is given as 2D color map in Fig. 5.3(c). Fig 5.3(d) shows the corresponding in-plane [1-100] deformation, ε_{yy} . The line scan profiles in Fig. 5.3(d) show the average out of plane strain across the QW, in the direction a , as indicated in Fig. 5.3(c), and the strain fluctuations within the QW in the direction b . The maximum ε_{yy} within the QW reaches 5.5% which corresponds approximately to In concentration of 35%, much larger than the nominal value (20%). Even higher fluctuations in In concentration up to 45% were measured in another FIB sample investigated under similar experimental conditions (Fig. 5.4).

Although the exact mechanism of the irradiation damage is still unclear, it is obvious that the modification of the QWs occurs faster with increasing electron dose rates. Because of the high electron dose required to produce high quality HRTEM images it cannot be guaranteed that GPA strain measurements in this material system are not affected by beam damage. To overcome this problem we have exploited dark-field inline electron holography (DIH) [17] which requires about two orders of magnitude smaller electron doses. This technique is able to provide quantitative analysis at nanometer spatial resolution. Inline electron holography techniques are based on the reconstruction of the exit face wave function from the set of TEM images recorded at different planes of defocus (inline holograms). DIH reconstructs relative phase differences in a single diffracted beam, which give direct access to the changes in the geometric phase [18,19] and with that variations in the lattice spacing.

Fig. 5.5(a) shows sub-areas of the set of dark field inline holograms recorded with a sampling of 0.25 nm per pixel. The influence of the inelastically scattered electrons on the image formation was minimized using the SESAM's in-column MANDOLINE energy filter. The reconstructed geometric phase image is shown in Fig. 5.5(b). The spatial resolution of the reconstruction is limited to 0.8 nm, matching the experimental resolution defined by the objective aperture. The indium distribution in the whole active region of the LED, in Fig. 5.6(a), was obtained from the geometric phase image (Fig. 5.5(b)).

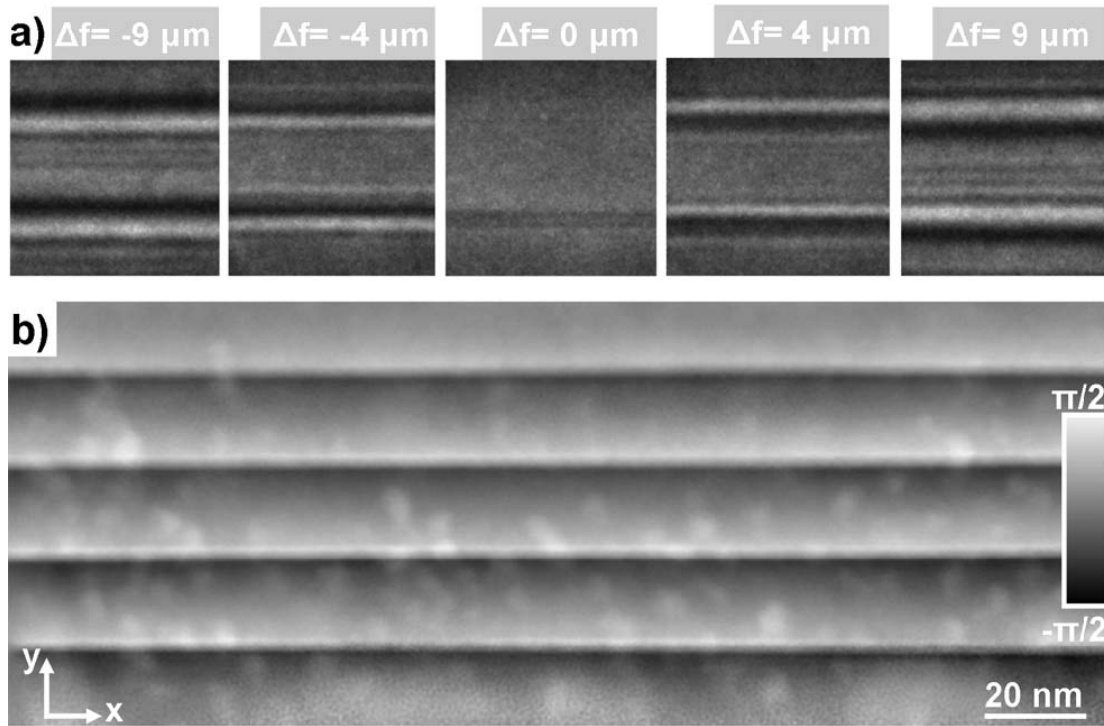


Fig 5.5: (a) shows the sub-areas (the size of the sub-areas correspond to the size of the dashed square in Fig. 5.1 (30 nm by 30 nm) of the (0002) dark field holograms. (b) displays the geometric phase image covering the whole active region of the LED reconstructed from 11 dark field images.

The composition profile extracted along the growth direction (Fig. 5.6(b)) shows oscillations, which appear as negative contribution at the interface and as double step within the QWs. These artificial oscillations may result from the mask applied to limit the spatial frequency in reciprocal space as well as from the abrupt step of the mean inner potential at the interface between the GaN and the InGaN. These oscillations would be less pronounced if a gradual chemical transition is present at the interface [9]. On the other hand, the oscillations are stronger compared to the ones observed in profiles obtained from HRTEM-GPA analysis (Fig. 5.2(c)) due to the increased multiple scattering contribution for thicker TEM samples used for DIH experiments.

To avoid the effect of artificial oscillations, it is necessary to extract the line profiles within the QWs. The profiles (1.6 nm integration width) shown in Fig. 5.6(c) reveal $20.8 \pm 1.2 \%$ and $22.5 \pm 1.4 \%$ indium fraction within the two inner QWs. The precision in the analysis calculated from the noise in the reference area (green profile in Fig. 5.6(c)) is 0.6 %. Comparing the compositional fluctuations within the QWs with the noise in the measurements, we have found no evidence for significant deviation from the indium distribution expected for a random alloy. Random alloy is

defined as following. The indium atoms are distributed randomly on the In/Ga sites, as would be expected from a simple ternary solution, without any tendency for the indium atoms to cluster together (for detailed analysis, see Ref. [20]).

The average indium concentration obtained from DIH is slightly higher than the GPA analysis, which might be due to the strain relaxation in the thin HRTEM specimens used for GPA analysis (20 - 30 nm) [7,9,14]. Although the DIH technique does not require a high quality thin TEM specimen, it is desirable to optimize the foil thickness to minimize the thin foil relaxation and projection related problems.

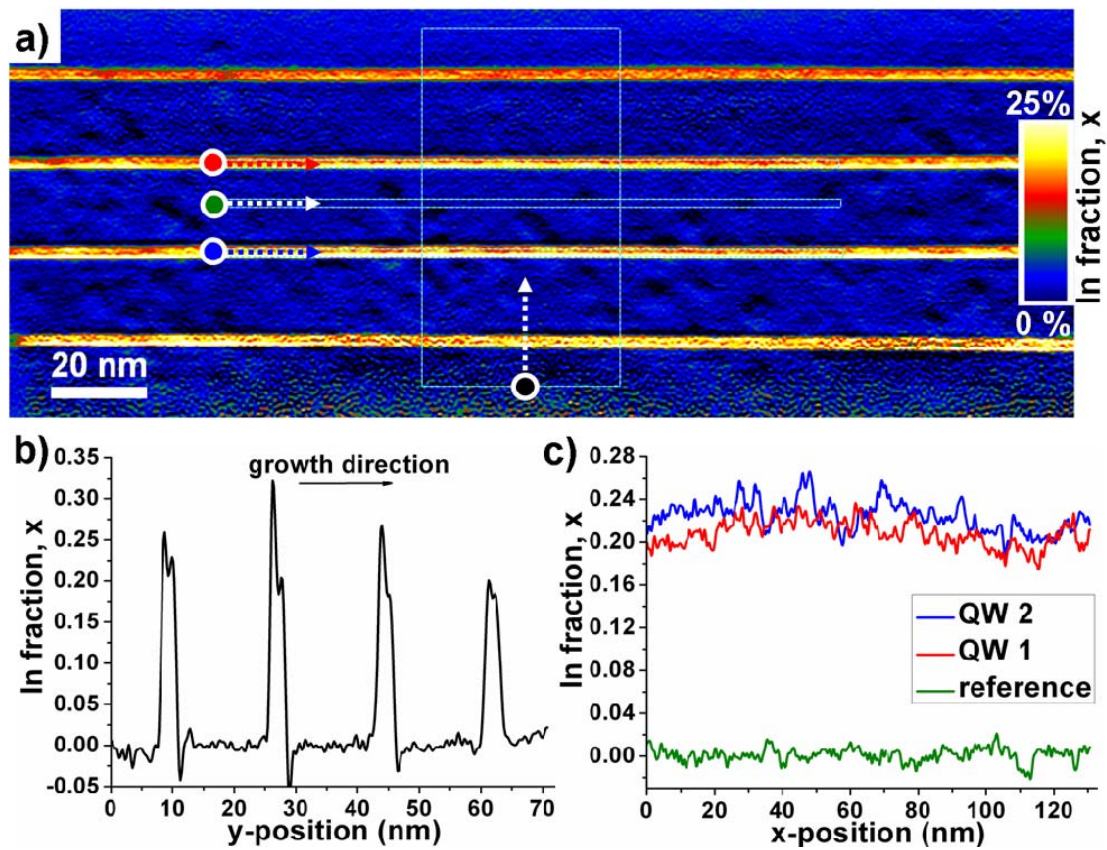


Fig 5.6: (a) Indium distribution map derived from the geometric phase image in Fig. 5.5(a). (b) The composition profile extracted along the growth direction (horizontally averaged over 40 nm). (c) The composition profiles extracted within the QWs and within the reference GaN buffer layer (averaged over a width of 1.6 nm).

5.4 Conclusion

Recently, strain maps covering a large field of view have also been reconstructed from dark-field off-axis holography (DOAH) measurements [18]. While DIH experiments may be performed on a standard TEM, DOAH requires some special equipment: an electrostatic biprism, a very bright electron gun, and, for a large field of view, a Lorentz lens. The poor resolution provided by standard Lorentz lenses (the spherical aberration coefficient typically being about 8000 mm) and the requirement to sufficiently sample the fine interference fringes in off-axis holograms allow this technique to achieve a resolution of about 4 nm for a comparable field of view [18]. Most importantly, DOAH requires the presence of an area of undistorted material at least as large as the region of interest and immediately adjacent to it. The commercial LED samples used in this study featured additional QW structures below and above the investigated area, making the application of DOAH impossible.

In conclusion, it is shown that the dark-field inline holography technique is ideally suited to map strain with very high precision at high spatial resolution, and a large field of view in beam-sensitive specimen. The technique is applied to map the composition of InGaN/GaN multiple QWs, which are very easily damaged by high dose electron beams. For comparison the same sample is analyzed using low-dose HRTEM-GPA. Within the error bars of the two techniques, the results agree very well. The slightly higher indium content measured by DIH compared to the HRTEM-GPA results may also be attributed to reduced thin-film strain relaxation in the thicker TEM specimen areas used in DIH experiments. Also, the error bar of the indium content extracted from the DIH experiments is smaller than in the HRTEM-GPA case.

References:

- [1] D. Gerthsen, E. Hahn, B. Neubauer, A. Rosenauer, O. Schön, M. Heuken, and A. Rizzi, *Composition fluctuations in InGaN analyzed by transmission electron microscopy*, phys. stat. sol. (a) **177**, pp. 145-155 (2000).
- [2] T.P. Bartel, and C. Kisielowski, *A quantitative procedure to probe for compositional inhomogeneities in In_xGa_{1-x}N alloys*, Ultramicroscopy **108**, pp. 1420-1426 (2008).
- [3] N. K. van der Laak, R. A. Oliver, M. J. Kappers, and C. J. Humphreys, *Characterization of InGaN quantum wells with gross fluctuations in width*, J. Appl. Phys. **102**, pp. 013513-013518 (2007).
- [4] D.M. Graham, A. Soltani-Vala, P. Dawson, M. J. Godfrey, T. M. Smeeton, J. S. Barnard, M. J. Kappers, C. J. Humphreys, and E. J. Thrush, *Optical and microstructural studies of InGaN/GaN single-quantum-well structures*, J. Appl. Phys. **97**, pp. 103508-103512 (2005).
- [5] T. Bartel, M. Dworzak, M. Strassburg, A. Hoffmann, A. Strittmatter, and D. Bimberg, *Recombination dynamics of localized excitons in InGaN quantum dots*, Appl. Phys. Lett. **85**, pp. 1946-1948 (2004).
- [6] S. Chichibu, K. Wada and S. Nakamura, *Spatially resolved cathodoluminescence spectra of InGaN quantum wells*, Appl. Phys. Lett. **71**, pp. 2346-2348 (1997).
- [7] C. J. Humphreys, *Does In form In-rich clusters in InGaN quantum wells?*, Philos. Mag. **87**, pp. 1971-1982 (2007).
- [8] M. Hÿtch, E. Snoeck, R. Kilaas, *Quantitative measurement of displacement and strain fields from HREM micrographs*, Ultramicroscopy **74/3**, pp. 131-146 (1998).
- [9] D. Gerthsen, E. Hahn, B. Neubauer, V. Potin, A. Rosenauer, and M. Schowalter, *Indium distribution in epitaxially grown InGaN layers analyzed by transmission electron microscopy*, phys. stat. sol (c) **0**, pp. 1668-1683 (2003).
- [10] C. T. Koch, W. Sigle, R. Höschen, M. Rühle, E. Essers, G. Benner, and M. Matijevic, *SESAM: Exploring the frontiers of electron microscopy*, Microscopy and Microanalysis **12**, pp. 506-514 (2006).

- [11] C. T. Koch, *A flux-preserving inline electron holography reconstruction algorithm for illumination of partial spatial coherence*, Ultramicroscopy, **108**, pp. 141-150 (2008).
- [12] C. Koch and A. Lubk, *Off-axis and inline electron holography: A quantitative comparison*, Ultramicroscopy **110**, pp. 460-471 (2010).
- [13] A. F. Wright, *Elastic properties of zinc-blende and wurtzite AlN, GaN, and InN*, J. Appl. Phys. **82**, pp. 2833-2839 (1997).
- [14] S. Kret, P. Dłuzewski, A. Szczepanska, M. Zak, R. Czernecki, M. Krysko, M. Leszczynski, and G. Maciejewski, *Homogenous indium distribution in InGaN/GaN laser active structure grown by LP-MOCVD on bulk GaN crystal revealed by transmission electron microscopy and x-ray diffraction*, Nanotechnology **18**, pp. 465707-465715 (2007).
- [15] T. M. Smeeton, M. J. Kappers, J. S. Barnard, M. E. Vickers, and C. J. Humphreys, *Electron-beam-induced strain within InGaN quantum wells: False indium “cluster” detection in the transmission electron microscope*, Applied Physics Letters **83**, pp. 5419-5421 (2003).
- [16] T. Li, E. Hahn, D. Gerthsen, A. Rosenauer, A. Strittmatter, L. Reissmann, and D. Bimberg, *In redistribution in an InGaN quantum well induced by electron-beam irradiation in a transmission electron microscope*, Appl. Phys. Lett. **86**, pp. 241911-241913 (2005).
- [17] C. T. Koch, V. B. Özdöl, and P. A. van Aken, *An efficient, simple, and precise way to map strain with nanometer resolution in semiconductor devices*, Appl. Phys. Lett. **96**, pp. 091901-091903 (2010).
- [18] M. J. Hÿtch, F. Houdellier, F. Hÿe, and E. Snoeck, *Nanoscale holographic interferometry for strain measurements in electronic devices*, Nature **453**, pp. 1086-1089 (2008).
- [19] F. Hÿe, M. Hÿtch, F. Houdellier, H. Bender, and A. Claverie, *Strain mapping of tensilely strained silicon transistors with embedded SiC source and drain by dark-field holography*, Appl. Phys. Lett. **95**, pp. 073103-073105 (2009).
- [20] M. J. Galtrey, R. A. Oliver, M. J. Kappers, C. J. Humphreys, D. J. Stokes, P. H. Clifton, and A. Cerezo, *Three-dimensional atom probe studies of an InGaN/GaN multiple quantum well structure: Assessment of possible indium clustering*, Appl. Phys. Lett. **90**, pp. 061903-061905 (2007).

Chapter 6

Correlating the structural, chemical and optical properties at nanometer resolution

Abstract:

Valence electron spectroscopic imaging (VESI) techniques, taking advantages of the energy-losses suffered by inelastic scattering of the fast electrons in the transmission electron microscope, offer an inherently high spatial resolution to characterize the electronic structure of materials close to the Fermi level. The combination of an electron monochromator and a highly dispersive imaging energy filter, which has become available only recently, allows reliable measurements of local bandgaps on the nanometer scale. In addition, the correlations of structural, chemical and optical properties can be revealed via VESI using monochromated electrons with a high spatial resolution. The following study demonstrates that plasmon mapping can be used to retrieve structural information of a material, such as strain, while the bandgap profile is strongly related to the local chemical composition.

6.1 Introduction

Intelligent design of materials and devices on the basis of nanometer scale structuring requires the development of characterization tools being able to visualize the relevant material properties with high spatial resolution. Electron spectroscopic imaging techniques in the TEM offer an inherently high spatial resolution. This is either achieved in a STEM by using a sub-nm electron probe scanning across the area of interest [1] STEM-SI or by recording images from a selected energy-loss range by making use of an electron energy filter, EFTEM [2]. In comparison to the STEM-SI method, valence-loss EFTEM usually provides shorter acquisition time and better spatial sampling which can efficiently enhance the imaging quality and prevent potential artifacts [3]. In recent years, EFTEM has become one of the most efficient methods for chemical composition mapping in materials on the nanometers scale [2]. In the EFTEM configuration, a certain energy-loss range is selected by a mechanical slit located in the energy-dispersive plane of the energy filter, which allows energy-filtered imaging or diffraction with a defined energy window.

For energy-losses below 50 eV, EFTEM maps contain material-specific information about volume, surface, and interface plasmons or single-electron excitations from the valence into the conduction band [4] which is why this technique is referred as valence-loss EFTEM. These excitations reflect the dielectric response of the materials to the electric field imposed by the transmitted fast electrons; thus they can be utilized for mapping of the corresponding electronic and optical properties [5]. It is not until recently that the development of monochromators and aberration-corrected energy filters has made valence electron energy-loss spectroscopy (VEELS) and valence-loss EFTEM powerful techniques. Owing to the non-isochromaticity of energy filters, there is a minimum useful size of the slit width for EFTEM studies. The excellent isochromaticity of the recently developed MANDOLINE filter included in the column of the SESAM microscope (Carl Zeiss, Oberkochen, Germany) [6] considerably increases the energy resolution of EFTEM mapping at low energy losses.

GaN and $\text{Al}_x\text{Ga}_{1-x}\text{N}$ alloys are among the direct wide-bandgap semiconductors which possess desirable optoelectronic properties for various applications such as light-emitting diodes (LED) and high-frequency, high-temperature electronics. In a direct semiconductor the minimum of the conduction band lies directly above the

maximum of the valence band in reciprocal space. Therefore, for bandgap measurements of direct semiconductors using VEELS, no momentum transfer perpendicular to the fast electron propagation direction is required to excite the electrons from the valence band into the conduction band. Thus the VEELS intensity is usually proportional to the joint density of states (JDOS) of the material [7]. Valence EFTEM is comparable to VEELS in this sense and the collection aperture directly determines the desired momentum transfer depending on different semiconductor transitions of interest.

Here, a reliable 2-dimensional (2D) EFTEM mapping of bandgaps using an $\text{Al}_{45}\text{Ga}_{55}\text{N}/\text{GaN}$ heterostructure is demonstrated with the use of monochromated electrons at the spatial resolution limit dictated by the fundamental limitation of the delocalization of the inelastic scattering process, *i.e.*, not limited by microscope aberrations. A volume-plasmon map on the same structure provides the local chemical composition and reveals a transition region at the interface. This compositional gradient was observed to coincide with the local strain gradient measured by the GPA method [8]. Both the compositional as well as the strain transition regions are considerably broader than that of the bandgap map. It was thus shown that valence EFTEM provides an effective access to local chemical, optical as well as structural properties at high spatial resolution. A thorough correlation of the structural, chemical and optical properties has not been demonstrated before with the highest possible resolution, which is of profound importance to understand material behaviors.

6.2 Experimental

The $\text{Al}_{45}\text{Ga}_{55}\text{N}/\text{GaN}$ structure was grown on [0001] sapphire by metal-organic chemical vapor deposition (MOCVD). Cross-sectional TEM specimens were prepared by the double-dimpling method followed by a final thinning using a precision-ion-polishing system (PIPS, Gatan, Pleasanton, USA). Owing to the electrostatic Ω -type monochromator and the improved stability, the energy resolution of the microscope defined by the full-width-at-half-maximum (FWHM) of the zero-loss peak is below 0.1 eV for routine applications. The in-column MANDOLINE filter provides high dispersion and high transmissivity. Since the signal-to-noise ratio is crucial in 2D bandgap mapping, we used a monochromator slit which gives about 0.2 eV energy resolution with the collection semi-angle defined by the objective aperture of 3 mrad. A series of images was acquired at energy losses from 2.5 to 5.5 eV with an energy-loss increment of 0.2 eV and an energy-selecting slit of 0.25 eV. For volume plasmon mapping of the $\text{Al}_{45}\text{Ga}_{55}\text{N}/\text{GaN}/\text{sapphire}$ structure, a series of images was acquired at energy losses from 2 to 30 eV with an energy-loss increment of 0.4 eV and an energy-selecting slit of 0.45 eV. HRTEM images were analyzed by the GPA method [8] to characterize the strain fields across the interface.

6.3 Results and discussion

In Fig. 6.1(a) an image constructed from the EFTEM series is shown where all images at energy losses ranging from 2 to 32 eV are summed up, *i.e.*, all the plasmon energies of the 3 materials ($\text{Al}_{45}\text{Ga}_{55}\text{N}/\text{GaN}/\text{sapphire}$) are included in the micrograph. To circumvent the potential limitations of the VEELS technique [9], we chose a specimen area with a sufficiently small thickness where artifacts due to Čerenkov radiation and surface effects are negligible in the studied material system [10]. To extract the bandgap energy from each image pixel of the EFTEM series we used the method described by Kimoto *et al.* [11], where the first apparent intensity increase in the local energy loss spectrum is taken as the bandgap value. The 2D bandgap map

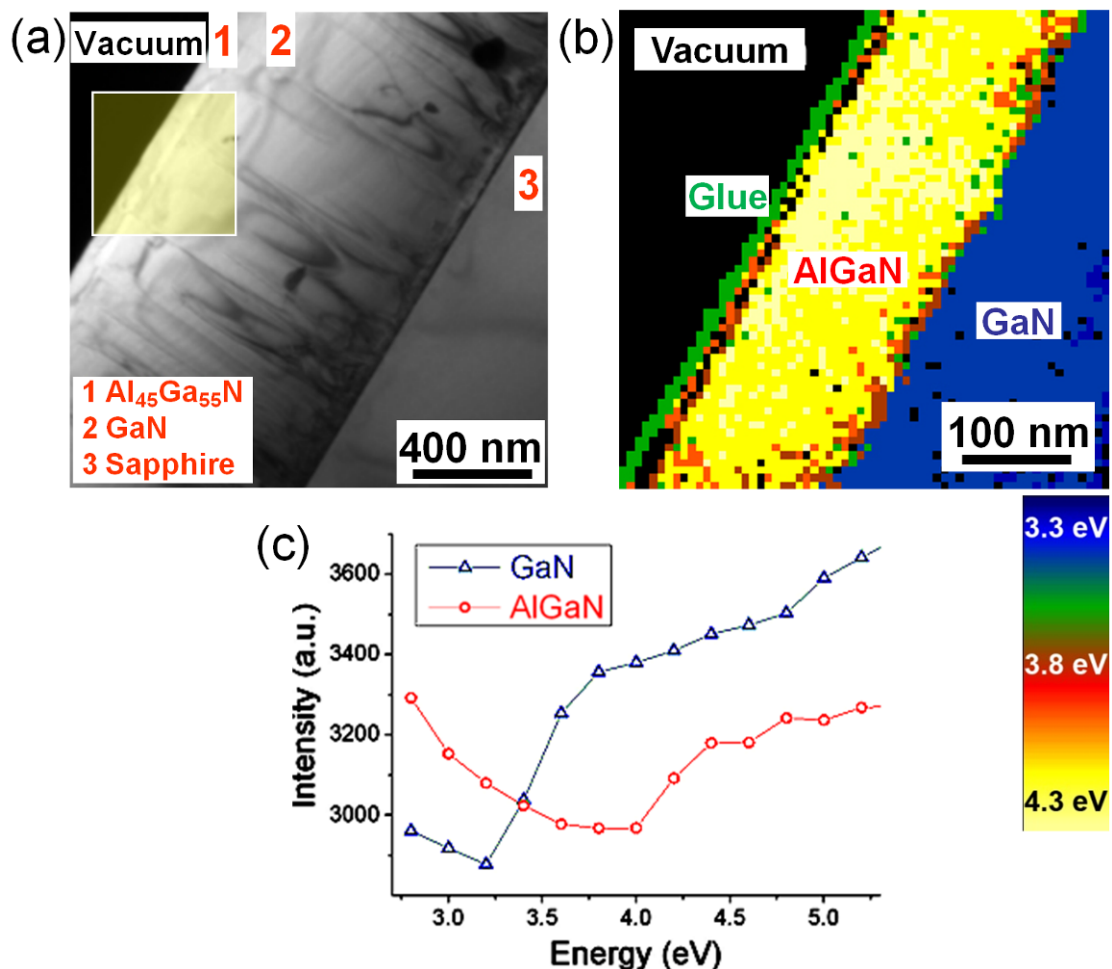


Fig. 6.1: (a) An integration of energy-filtered images showing the $\text{Al}_{45}\text{Ga}_{55}\text{N} / \text{GaN} / \text{sapphire}$ structure. (b) Bandgap mapping (pixel size = 6 nm) of the region marked in (a), corresponding bandgap values can be read from the color-coded legend. (c) Line profiles extracted from the 3D EFTEM stack indicating the bandgap difference to be about 0.8 eV.

obtained by this technique is shown in Fig. 6.1(b), and the corresponding bandgap values can be read from the color-coded legend. These bandgap values are highly consistent with recent theoretical calculations [12]. A similar bandgap map was presented recently Tsai *et al.* [13] using non-monochromated electrons. However, the energy resolution one can achieve without a monochromator is limited so that the bandgap onsets are difficult to be extracted from the EFTEM series.

No abrupt bandgap transition between Al₄₅Ga₅₅N and GaN is observed, as revealed from the intermediate bandgap energies of about 3.7 eV close to the interface. This apparent gradual change of the band gap can be mainly attributed to the inelastic delocalization arising from the low energy losses involved. A rough estimation of the inelastic delocalization length parameter d_{50} , within which 50 % of the total delocalized intensity is contained, suggests that at an energy loss of 2 eV with a kinetic energy of 200 keV for the fast electrons, d_{50} is larger than 11 nm [14]. This figure is close to the transition region revealed in Fig. 6.1(b), indicating a relatively sharp interface bandgap profile between the materials. An approximate expression of the d_{50} based on the single atom calculation shows that: [14]

$$d_{50} \approx 0.6\lambda / \bar{\theta} \approx 0.5\lambda / \theta_E^{3/4} \quad (6.1)$$

where λ is the electron wave length, $\bar{\theta}$ is the median angle of inelastic scattering and θ_E is the characteristic scattering angle, indicative of a large delocalization length at low energy losses. In a recent [15] paper we reported about the possibility to improve this fundamental limitation of spatial resolution at low energy losses by using dark-field valence spectroscopic imaging. This makes VEELS and valence-EFTEM powerful tools in retrieving the structural and electronic information of materials on the nanometer scale [15]. At the edge of the specimen, a thin layer (green) of materials with a bandgap value of about 3.5 eV is visible, which arises from the glue line due to specimen preparation. Figure 6.1(c) shows the extracted spectra from the 3D EFTEM data stack. The bandgap onset difference between GaN and Al₄₅Ga₅₅N was measured to be about 0.8 eV, consistent with previous studies [10].

In Fig. 6.2(a), a map of the Al₄₅Ga₅₅N/ GaN/ sapphire structure is shown using the volume plasmon peak energies obtained from the EFTEM image stack. The peak energies were acquired by a least-squares fit of a polynomial function to the plasmon peak for each image pixel. Note that the thin glue line (in white color) on top of the

Al₄₅Ga₅₅N layer gives plasmon peak energy of about 24 eV. A line profile of the plasmon peak energies is shown in Fig. 6.2(b) drawn across the GaN and Al₄₅Ga₅₅N interface in the position marked by the box in Fig. 6.2(a). The plasmon peak energy for GaN is (19.61 ± 0.04) eV and (20.21 ± 0.11) eV for Al₄₅Ga₅₅N. It is clearly revealed that the drop of the plasmon peak energy across the interface is far from abrupt; whereas the Al profile obtained by a line-scan of the corresponding *L*-edge energy loss displays a rather sharp picture.

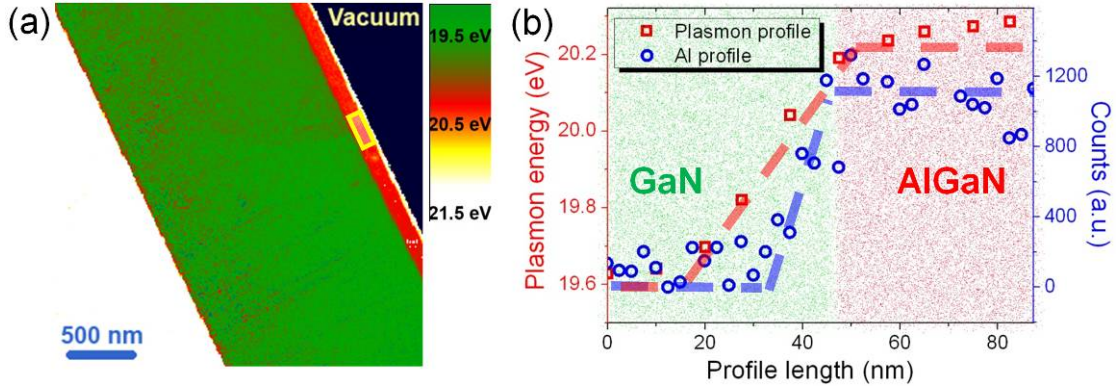


Fig. 6.2: (a) Plasmon mapping of the Al₄₅Ga₅₅N(red)/ GaN(green)/ sapphire(white) structure, respective plasmon energies can be read from the legend. (b) A line-profile acquired from the region marked in (a) showing the plasmon energy difference together with an Al profile across the interface obtained by the *L*-edge energy loss from the corresponding element.

One reason could be attributed to a gradual variation of the bandgap across the interface because the plasmon peak energy depends on the bandgap value as [3]

$$E_p \cong \left[\frac{\hbar^2 n e^2}{\epsilon_0 m_0} + E_g^2 \right]^{\frac{1}{2}} \quad (6.2)$$

where n is the valence electron density, e is the electronic charge, ϵ_0 is the permittivity of space, m_0 is the electron rest mass and E_g is the bandgap value. However, this would explain only a variation of the plasmon-peak energy by about 0.8 % by moving from pure GaN to Al₄₅Ga₅₅N. In addition, the bandgap mapping shown in Fig. 6.1(b) displays a relatively sharp transition, similar to that of the Al distribution, despite the fact that the inelastic delocalization degrades the attainable spatial resolution. Therefore it is concluded that the bandgap variation is not the main reason for the plasmon-peak energy variation.

Another reason for a variation of the plasmon peak energy is a change of the valence electron density, [16] arising from changes of the unit-cell volume for instance [17]. In order for more detailed insight into the variations of the unit cell across the interface, HRTEM investigations are performed followed by GPA at the corresponding regions. Fig. 6.3(a) shows a HRTEM micrograph acquired from the interface, where only (0002) planes are visible as shown in the enlargement.

The position of the interface is marked by arrows. A 2-beam configuration (excitation of mainly the (0000) and (0002) reflections) was exploited in order to increase the signal-to-noise ratio. Due to the lattice mismatch, the $\text{Al}_{45}\text{Ga}_{55}\text{N}$ layer is compressively strained in the growth direction under coherent deposition conditions.

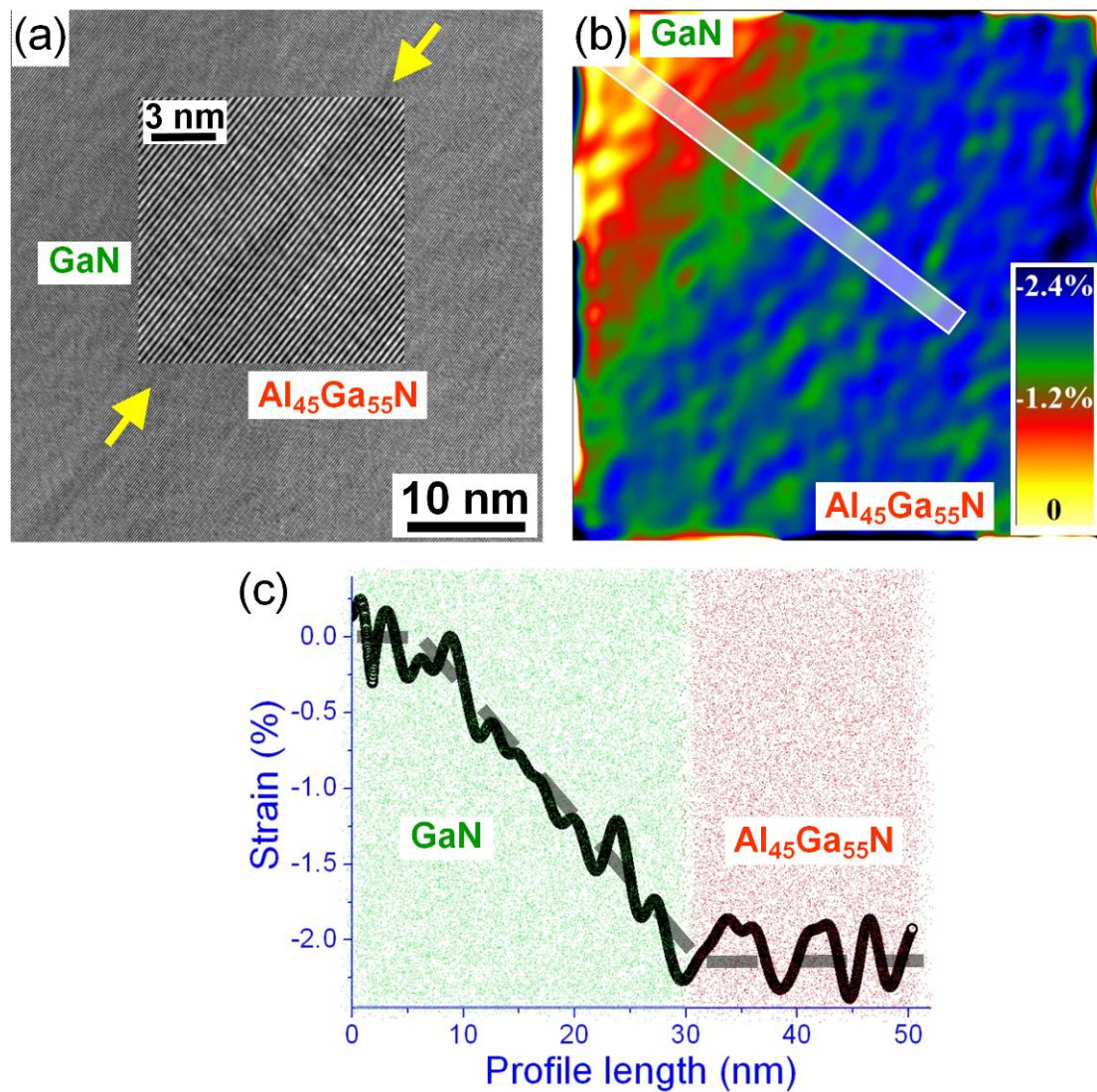


Fig. 6.3: (a) Off-zone-axis HRTEM image across the interface. Only (0002) planes are visible. (b) 2D tetragonal strain map in the growth direction. (c) A line-profile acquired from the region marked in (b) showing the strain gradient at the interface.

The 2D strain map obtained by applying GPA across the interface is given in Fig. 6.3(b). The strain evolution at the interface is shown in Fig. 6.3(c) as an integrated line profile from the region marked with a white box in Fig. 6.3(b). The local lattice parameter change in the growth direction was measured as (2.08 ± 0.16) % with respect to the undistorted GaN layer. In contrast to the chemistry profile, shown in Fig. 6.2(b) where the transition of the Al concentration profile across the interface is below 10 nm, the strain map reveals a rather broad distribution, very much like the plasmon peak energy profile. Owing to the fact that the plasmon peak position is directly linked to the valence electron density, the peak energy is a measure of unit-cell volumes. As the two independent measurements of strain and plasmon peak energy closely coincide, this reflects strong microscopic and spectroscopic evidences that the plasmon peak energy mapping can also be used for strain mapping [18], with a spatial resolution on the nanometer scale. Because the plasmon peak energy can be measured with accuracy below 0.5 %, variations of the unit-cell volume as small as $1.5 \times 10^{-4} \text{ nm}^3$ are detectable.

Taking into account the high spatial resolution of this technique of less than 2 nm [19], this is a very promising method for the analysis of strained-layer systems. On the other hand, both the bandgap and the chemistry profiles in our study exhibit a relatively abrupt change with similar trend, which provides a direct microscopic evidence to demonstrate the correlation of the optical properties with respect to the corresponding chemistry characteristic.

6.4 Conclusion

The combination of an electron monochromator and a highly dispersive imaging energy filter provides reliable measurements of local bandgaps on the nanometer scale. In addition, the structural, chemical and optical properties of materials can be correlated via valence electron spectroscopic imaging with monochromated electrons at high spatial resolution. Although the limited brightness of the electron source in the TEM used in this study and the need for a monochromator, which further reduces beam intensity, limit the signal to-noise ratio and with that the attainable spatial resolution, the measured widths of plasmon and strain profiles of about 30 nm are very distinct from those of the bandgap and Al concentration profiles which are significantly narrower about 15 nm and below 10 nm, respectively. This demonstrates that plasmon mapping can be used to retrieve structural information of a material, such as strain, while the bandgap profile is strongly related to the local chemical composition.

References:

- [1] P. E. Batson, *Simultaneous STEM imaging and electron energy-loss spectroscopy with atomic-column sensitivity*, *Nature* **366**, pp. 727-728 (1993).
- [2] L. Reimer, *Energy-Filtering Transmission Electron Microscopy*, (Springer-Verlag, Berlin and Heidelberg, 1995).
- [3] R. F. Egerton, *Electron Energy-Loss Spectroscopy in the Electron Microscope*, 2nd ed. (Plenum press, New York and London, 1996).
- [4] W. Sigle, *Analytical transmission electron microscopy*, *Annu. Rev. Mater. Res.* **35**, pp. 239-314 (2005).
- [5] H. Raether, *Excitation of Plasmons and Interband Transitions by Electrons*, *Springer Tracts in Modern Physics*, Vol. 88 (Springer-Verlag, Berlin 1980).
- [6] C. T. Koch, W. Sigle, R. Höschel, M. Rühle, E. Essers, G. Benner, and M. Matijevic, *SESAM: Exploring the frontiers of electron microscopy*, *Microscopy and Microanalysis* **12**, pp. 506-514 (2006).
- [7] B. Rafferty and L. M. Brown, *Direct and indirect transitions in the region of the band gap using electron-energy-loss spectroscopy*, *Phys. Rev. B* **58**, pp. 10326-10337 (1998).
- [8] M. Hÿtch, E. Snoeck, R. Kilaas, *Quantitative measurement of displacement and strain fields from HREM micrographs*, *Ultramicroscopy* **74/3**, pp. 131-146 (1998).
- [9] M. Stöger-Pollach, H. Franco, P. Schattschneider, S. Lazar, B. Schaffer, W. Grogger, and H. W. Zandbergen, *Cerenkov losses: A limit for bandgap determination and Kramers-Kronig analysis*, *Micron* **37**, pp. 396-402 (2006).
- [10] L. Gu, V. Srot, W. Sigle, C. T. Koch, P. A. van Aken, F. Scholz, S. B. Thapa, C. Kirchner, M. Jetter, and M. Rühle, *Band-gap measurements of direct and indirect semiconductors using monochromated electrons*, *Phys. Rev. B* **75**, pp. 195214-195221 (2007).
- [11] K. Kimoto, G. Kothleitner, W. Grogger, Y. Matsui, and F. Hofer, *Advantages of a monochromator for bandgap measurements using electron energy-loss spectroscopy*, *Micron* **36**, pp. 185-189 (2005).
- [12] P. Rinke, A. Qteish, J. Neugebauer, C. Freysoldt, and M. Scheffler, *Combining GW calculations with exact-exchange density-functional theory: an*

analysis of valence-band photoemission for compound semiconductors, New J. Phys. **7**, 126 (2005).

[13] J. S. Tsai, J. J. Kai, L. Chang, and F. R. Chen, *Bandgap mapping for III-V quantum well by electron spectroscopy imaging*, J. Electr. Microsc. **53**, pp. 371-380 (2004).

[14] R. F. Egerton and P. A. Crozier, *The effect of lens aberrations on the spatial resolution of an energy-filtered TEM image*, Micron **28**, pp. 117-124 (1997).

[15] L. Gu, W. Sigle, C. T. Koch, J. Nelayah, V. Srot, and P. A. van Aken, *Mapping of valence energy losses via energy filtered annular dark-field scanning transmission electron microscopy*, Ultramicroscopy **109**, pp. 1164-1170 (2009).

[16] D. Pines, *Collective energy losses in solids*, Rev. Mod. Phys. **28**, pp. 184-198 (1956).

[17] O. Ambacher, *Growth and applications of group III-nitrides*, J. Phys. D: Appl. Phys. **31**, pp. 2653-2710 (1998).

[18] A. M. Sanchez, R. Beanland, A. J. Papworth, P. J. Goodhew, and M. H. Gass, *Nanometer-scale strain measurements in semiconductors: An innovative approach using the Plasmon peak in electron energy loss spectra*, Appl. Phys. Lett. **88**, pp. 051917-051919 (2006).

[19] W. Sigle, S. Krämer, V. Varshney, U. Eigenthaler, and M. Rühle, *Plasmon energy mapping in energy-filtering transmission electron microscopy*, Ultramicroscopy **96**, pp. 565-571 (2003).

Chapter 7

Dedicated sample preparation techniques for transmission electron microscopy

Abstract:

Successful TEM depends on many parameters, one being the preparation of high quality specimens. With the tremendous advances in spatial and spectral resolution of state of the art microscopes, the quality of the samples examined has become a major limiting factor for quantitative analysis at the nanometer scale. Most of the preparation techniques currently in use have been exploited for many years in the microscopy laboratories around the world. There is numerous literature available which describes the existing techniques in detail, such as the earlier book by Hirsch et al [1], the books by Goodhew [2,3], the textbook by Williams and Carter [4], a series of book compilation by the Materials Research Society during 1990's [5-8], the Handbook of Microscopy [9] and, very recently, a comprehensive handbook set by Ayache et al [10,11]. Also an interactive data base has become available for sample preparation methods covering applications from material science to biological and earth sciences [12].

Each material and each field of electron microscopy application may require its own specific preparation technique. In the following context it will not be possible to cover all approaches systematically and in detail. Therefore, a short overview of the major preparation techniques will be followed by several examples of state of the art applications, mainly for nanometer scale characterization. For a more comprehensive and technical description of each particular method, the reader should follow the dedicated literature referred throughout the specific chapters. Manufacturers producing sample preparation tools may provide useful and complete information for dedicated applications of the methods described here [13-16].

7.1 Indirect preparation methods

The indirect methods, often referred as replica techniques, have been mainly used in earlier times to extract information about the surface topography or fracture surface of materials where the resolution of the nanometer sized features was the limiting factor for scanning electron microscopy (SEM) investigation [17]. Replica techniques can be divided into four main classes as (i) *direct replicas*, (ii) *indirect replicas*, (iii) *extraction replicas*, and (iv) *freeze fracture replicas*.

Direct replicas rely on the shadowing of the materials surfaces by deposition of thin metal film (usually Pt or W) at an oblique angle, which is then fixed by C deposition. The resulting shadowing metal-carbon surface film is then isolated by dissolution of the material investigated. The technique is mostly used for metals and semiconductors, but also applicable for electron beam sensitive materials like polymers. For characteristic film thicknesses like 5 nm for Pt and 30 nm for C, the surface topography can be revealed as good as with 1 nm height and 3 nm lateral resolution [18].

Indirect replicas are prepared mainly in the absence of appropriate solvent for the material investigated. Therefore, first, the topographical print of the surface is obtained by molding using liquid polymer. The direct replica procedure is then applied to the plastic mold resulting in a negative impression of the surface morphology. The resolution is poorer compared to direct replicas, but surface features in the order of 10 nm are resolvable.

Extraction replicas are used mainly to investigate submicron size inclusions or precipitates in the metal matrix. It involves stepwise etching of the matrix material to expose the inclusions on the surface. A 10 to 30 nm thick carbon film is then deposited under vacuum as a supporting material. The matrix material is then further dissolved revealing the inclusions trapped within the carbon film. The main limiting factor for this method is the availability of the solvent that dissolves the matrix selectively but also avoids the formation of new products like oxide particles [19].

Freeze fracture replicas are prepared to investigate the ultrastructure of the rapidly frozen biological samples [20]. Four main steps of the method include (i) rapid freezing of the specimen, (ii) fracturing it at low temperature (170 K or lower), (iii) making the direct replica of the newly exposed frozen surface by vacuum-

deposition of carbon or platinum, and (iv) cleaning the replica using bleach or acids to remove the biological material. The critical feature of the freeze-fracture technique is the tendency of the fracture plane to follow a plane through the central core of frozen membranes, splitting them into half-membrane leaflets. The resulting views of the membranes give three-dimensional perspectives of cellular organizations revealing the distribution of internal membrane proteins. Fig. 7.1 displays an example of a freeze fracture overview of lipid droplets (LD) in a lipid laden macrophage and their association with endoplasmic reticulum (ER) membranes [21].

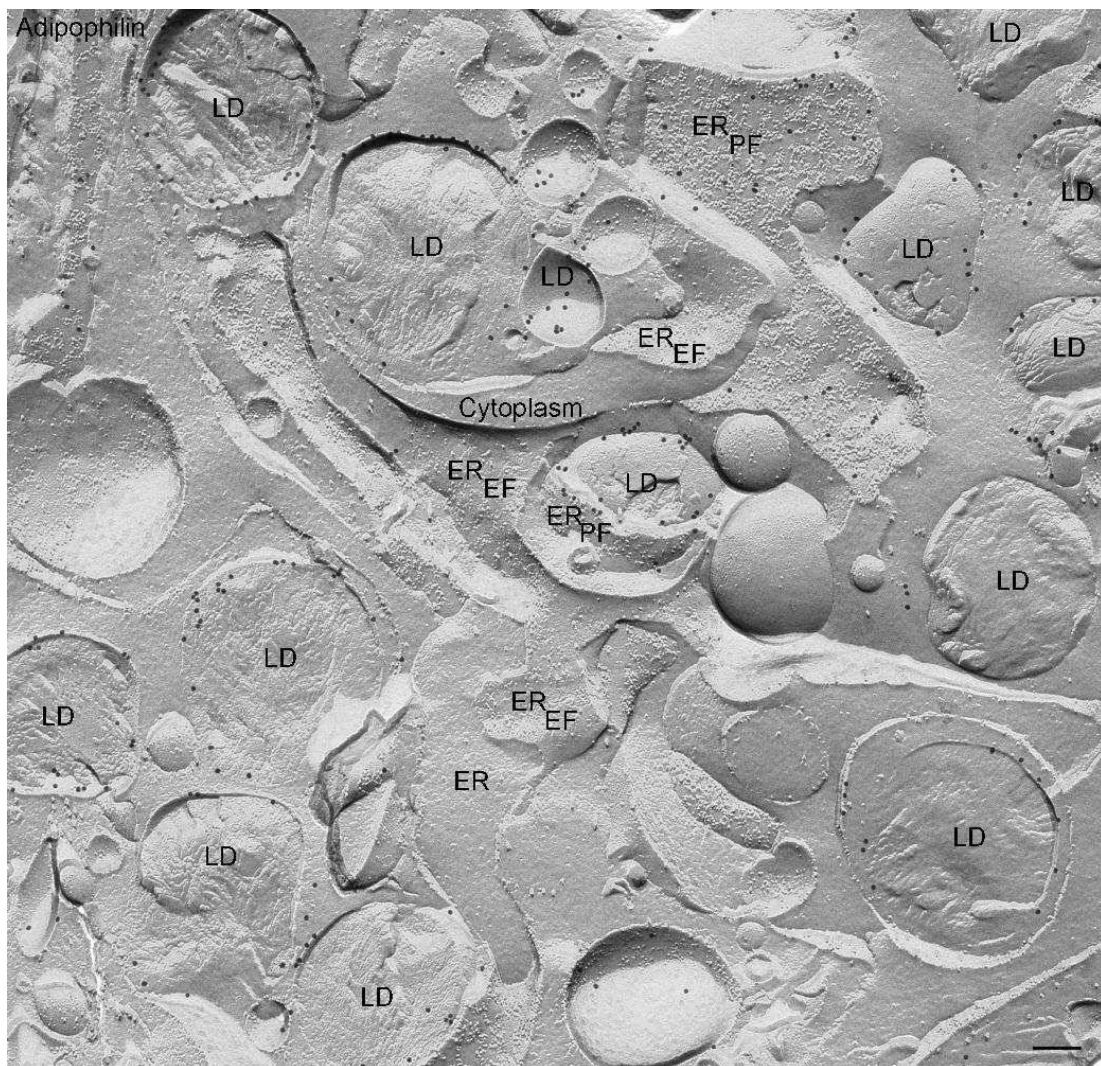


Fig. 7.1: Freeze fracture replica image of lipid droplets (LD) in a lipid laden macrophage and their association with endoplasmic reticulum (ER) membranes (reproduced from Ref. [21]).

7.2 Preliminary preparation techniques

Preliminary preparation steps are necessary in most of the cases prior to thinning the specimen to electron transparency. The techniques suitable for individual materials systems vary depending on its properties, e.g. whether it is ductile or brittle, soft or hard, porous or bulk, or conductive or nonconductive.

Sawing is necessary to cut thin slices from a bulk sample. Wheel or wire saws with abrasive blades or wires are used to obtain slices as thin as one hundred microns. While cutting speed varies from mm/h to mm/min depending on the material, water cooling and lubricants help to prevent temperature rise. Alternatively, electrochemical saws for conducting materials or acid saws without abrasives are used to avoid mechanical damage on the sample.

Ultrasonic cutters are used to cut different shapes of small dimensions (few millimeters) from hard material specimens. A hollow cutting tool vibrates laterally at high frequency and cuts into the specimen with the aid of abrasive containing lubricant or water.

Punching can be used for ductile metallic materials, where small disks (generally with a disk diameter of 3 mm) can be punched out from thin metal foils (100 μm).

Mechanical polishing is necessary for thinning the specimen either in plan-view or cross-section geometry and to obtain smooth scratch-free and flat surfaces by removing the mechanical damage due to cutting or sawing. A rotating disk (20 – 30 cm in diameter) with variable speed, which holds the polishing platforms or cloths with abrasive powders spread on it, is used for polishing the specimen under water cooling. Several steps are performed starting from coarse-grinding to final surface cleaning by using progressively finer-sized abrasives (e.g. silicon carbide, diamond, alumina or boron carbide, with grain sizes from 100 μm down to 1 μm). As an alternative to ultrasonic cutters or punching tools, disks can be prepared from crystals glued to 3-mm thick rods.

Dimpling is a widely used method to thin the center of a pre-cut flat disk with a diameter of 3 mm prior to final thinning of the specimen by means of electrochemical polishing or ion milling. Using this procedure, the specimen thickness in the center of the disc is reduced generally from 100 μm to 5-10 μm . The specimen

is centered and rotated on a variable-speed rotating axle, while a rotating grinding wheel made of bronze or steel grinds a dimple in the center. Progressively finer abrasives (3 – 0.1 μm in grain size), generally a paste containing a lubricant, are used to obtain a scratch-free final polish on both sides, while the depth of dimple is controlled and regulated precisely by a micrometer sensor and counterweight load.

For fine particles or fibers, which are hardly possible to handle or too soft, and for very brittle samples, *embedding* is necessary prior to other thinning methods. The sample is placed into a mold and immersed into a liquid resin which is then hardened by polymerization. For porous materials, infiltration-embedding can be performed, where the resin also fills into the gaps in the material. Embedding is specially needed for sample preparation using ultramicrotomy methods.

Chemical fixation is required mainly for hydrated biological samples prior to dehydration. Fixatives, either aldehydes or strong oxidants, are used to transform the protein gel into a cross-linked network so that the structure is preserved during subsequent dehydration.



Fig. 7.2: Several examples for preliminary preparation tools used in TEM specimen preparation: (a) punching tool, (b) wheel saw, (c) ultrasonic disk cutter, (d) wire saw, (e) rotary grinder/polisher, (f) dimple grinder.

7.3 Cleavage techniques

Cleavage is a relatively simple, quick and inexpensive method to prepare TEM samples without artifacts arising from further thinning procedures [22]. The technique requires materials to cleave or fracture, therefore its application is mainly limited to hard materials such as semiconductors, glasses, silicon carbide or sapphire. The procedure involves initiation of mechanical stress induced micro-cracking (generally using a diamond tip) of a back-thinned substrate (100-150 μm) along weakly bonded atomic planes. For instance, for epitaxially grown compound semiconductors such as GaAs with [001] surface orientation a 90° wedge is formed by initiating cleavage on the (110) and ($1\bar{1}0$) planes to obtain an electron-transparent edge [23]. The wedge is then mounted on a support grid using conductive epoxy as shown in Fig. 7.3(a).

A more delicate variation of cleaving, known as the small-angle cleaving technique (SACT), has been developed to achieve larger electron-transparent regions. In this case, the sample is first scribed on the pre-thinned side at a small angle to a standard cleavage plane ($15\text{-}30^\circ$), and then cleaved along the scribe line. For a Si (001) wafer for instance, the back-side of the wafer is scribed and cleaved along a $\{120\}$ plane. The cleavage can preferably be performed under water, as the liquid will control the stress field during fracture, improving the quality of the cleaved edge [24]. Sufficient back-thinning is essential to minimize the artifacts such as cleavage steps or tears. A second cleave is made from the front side of the wafer. The scribe is made along a $\{110\}$ plane and cleaved along this standard cleavage plane resulting in a small-angle wedge. For a more detailed description and various applications the reader is referred to the following references [22, 25, 26].

Whereas the short preparation time (less than an hour) enables to examine the films or coatings very soon after their growth, the technique can be used as a quick pre-thinning method prior to focused-ion milling as well [27]. It is particularly useful for samples that contain amorphous material, which may not be prepared using ion-assisted methods due to the severe artifacts induced by ion implantation. Fig. 7.3(b) displays the view of a Yb/Si specimen prepared by SACT [28]. At the tip of the wedge, the specimen is thin enough even for HRTEM, as shown in Figure 3c.

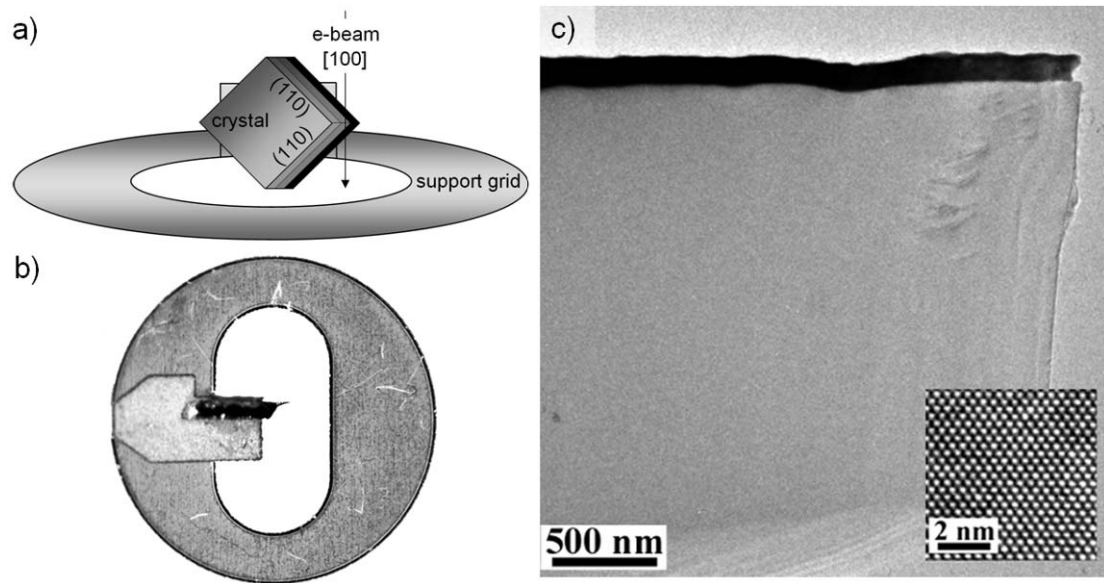


Fig. 7.3: (a) Orientation of a 90° wedge crystal on a special support grid. (b) Visible light microscopy image of a Yb/Si film prepared using the SACT. (c) Si wedge with a silicide film. The inset is an HRTEM image of the substrate (reproduced from Ref. [28]).

7.4 Chemical and electrolytic methods

Preparation of electron transparent specimens by means of chemical and electrolytic methods has been developed mostly in the earlier years of electron microscopy. These methods have been applied to broad range of materials [29-31], but mainly to metallic and semiconductor materials to avoid strain hardening and preparation artifacts due to high temperatures or ion irradiation [32]. The main principle of the methods relies on the polishing of the thin slice of material by chemical dissolution. In the case of electrolytic methods the thinning occurs as an anodic electrochemical dissolution of a conductive material. For both chemical and electrolytic thinning, there are two basic techniques. In the *window technique*, the mechanically pre-thinned specimen is immersed into an appropriate solvent to obtain a thin foil with relatively flat surfaces. The area of interest is defined by isolating the rest of the specimen from the solvent. In the more widely used *twin-jet polishing technique*, the electrolyte is introduced as a thin jet through a nozzle towards the surfaces of the pre-cut specimen to localize the dissolution effect.

For either method, the availability of the appropriate solvents is the key factor. A broad range of recipes for etching solutions can be found in the literature [32, 33]. The solution temperature is kept low to control the etching rate. In the case of electrolytic polishing, the applied voltage and current as well as the electrode materials influence the thinning rate. In many cases it is difficult to find the appropriate electrolytic solution, potential condition, current and adequate temperature for complex or multiphase materials. However, if the correct conditions are fulfilled, this technique has been successfully applied to multiphase materials such as metal alloys e.g. Cu-Cr or Mo-C [34] and semiconductor multilayer materials e.g. heterostructure systems of GaAs, AlAs, InP and HgTe [35, 36].

Since the thinning process does not introduce mechanical stress on the specimen, etching methods are particularly essential for the investigation of defects in deformed materials. The bright-field TEM image shown in Fig. 7.4 reveals the dislocation network in a deformed polycrystalline Cu alloy prepared by electrolytic polishing. The original defect density is maintained by avoiding any preparation-related strain hardening.

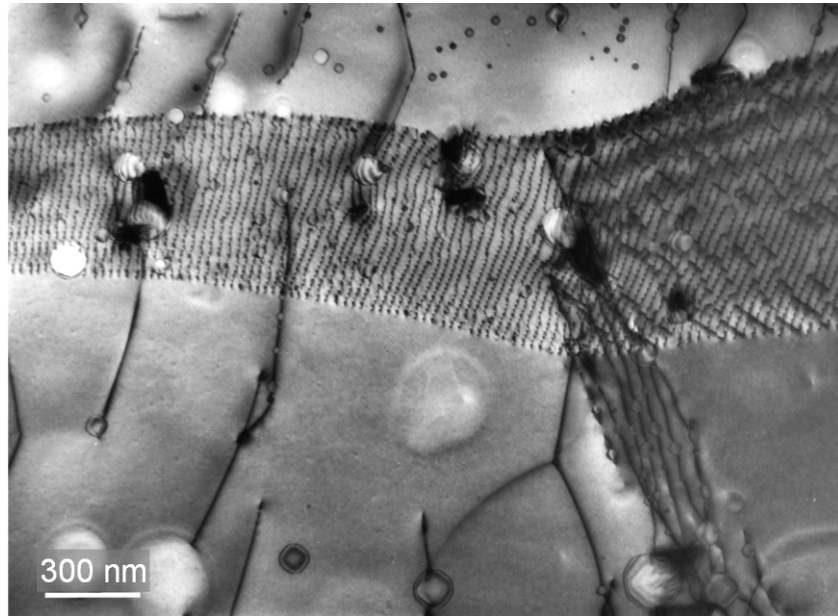


Fig. 7.4: Bright-field image of a dislocation-network in a polycrystalline Cu specimen prepared by electrolytic etching. Potential difference of 35 V at 100 mA was applied to etch the specimen in HNO₃/Methanol solution (1:2 volume ratio) at -50° C (specimen and the image courtesy of: Marion Kelsch, unpublished results).

7.5 Ion beam milling

One of the most widely spread specimen preparation techniques for TEM is ion-beam milling [9, 37]. The basic setup for ion milling requires an ion gun attached to a vacuum chamber (with a pressure in the order of 10^{-5} mbar). It involves bombardment of a mechanically pre-thinned specimen with energetic ions (typically Ar^+) which are accelerated and formed into a focused ion beam (Fig. 7.5 and 7.6 display the basic setup and examples for ion milling equipments, respectively). Mechanical thinning (down to 10-30 μm) is required prior to ion milling, which involves dimple grinding and polishing of the sample. The specimen surfaces should be smoothly polished which is favorable for the final high quality of the sample.

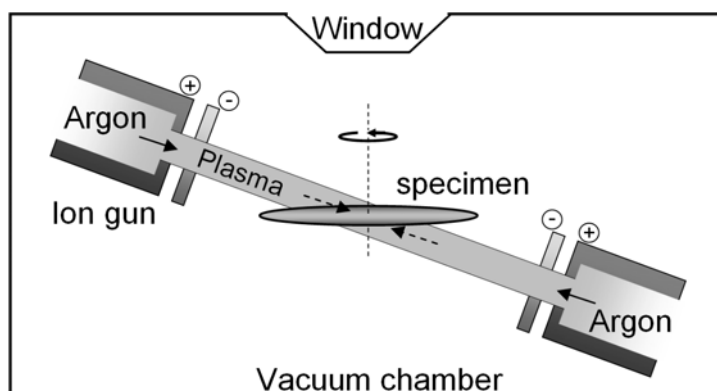


Fig. 7.5: Schematic diagram of an ion milling machine. Ar gas is introduced into the ionization chamber where potential difference creates Ar ions accelerated towards the rotating specimen.

In addition to the improvements of the specimen stage in terms of design and materials used [38], advances in modern electronics have allowed very precise manipulation of the ion beam in several ways such as modulating or focusing it tightly (e.g. 350 μm FWHM at 5 keV - 800 μm FWHM at 5 keV for broad beam guns) or controlling the incidence angle (typically from 10° to 1°) by retarding fields [39]. Different setups, like single or double sector thinning, accurate alignment and positioning of ion beams on the specimen surface and rotation of the specimen (generally at a few rpm) have made ion milling a precise and effective method, and enabled not only plan-view but especially cross-section sample preparation.

In the earlier efforts of improving the final surface quality of the specimens, geometrical models for ion beam erosion revealed that the main characteristic features of milling process (sputtering rate, topographical modifications, irradiation damage, etc.) depend on the incidence angle of the ion beam with respect to the specimen surface [40]. During preparation of cross-section TEM samples of multilayer structures for instance, differential thinning effects can be minimized by milling at low angles (down to 1°), so that the layers with slow thinning rate protect the fast milling layers from the ion beam. The preferential thinning at the interfaces can be further reduced by rocking the specimen, so that the ion beam does not travel only along the interfaces [41]. Fig. 7.7 shows defocused dark-field (DF) images of a Si/SiGe heterostructure to demonstrate the influence of the ion beam incidence angle and of the rotation of the specimen on the topographical surface quality. Using an incidence angle of 8° at 4 kV accelerating voltage of the Ar ions and a specimen oscillation limited to $\pm 20^\circ$, preferential thinning coupled with re-deposition of sputtered material [42] results in topographical modification (as marked with black arrows in Fig. 7.7(a)). Reducing the incidence angle down to 2° and allowing complete rotation of the specimen, these artifacts can be minimized as shown in Fig. 7.7(b).

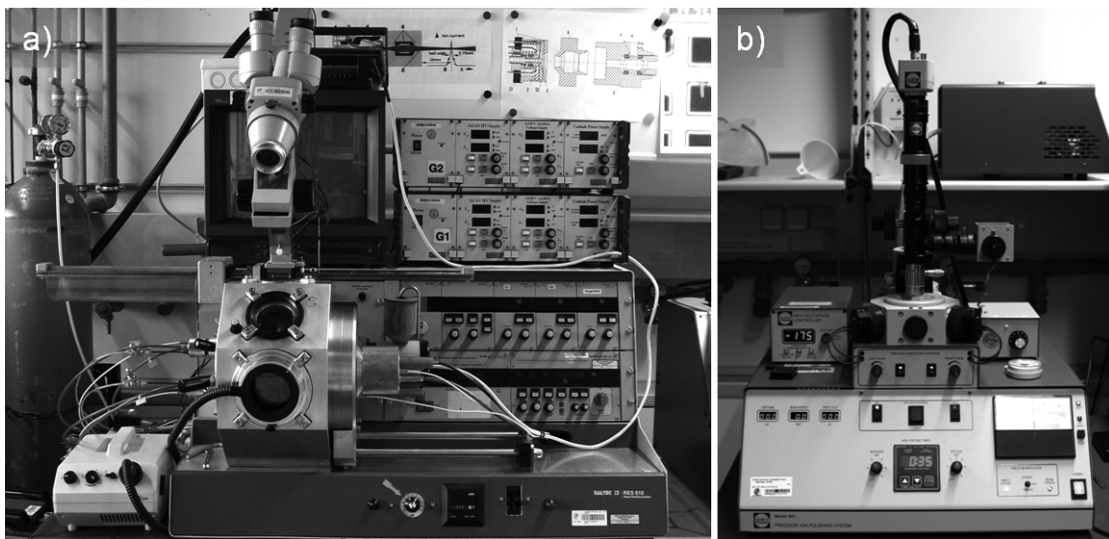


Fig. 7.6: Low energy ion milling equipments showing the evolution of device development: (a) modified ion-milling machine equipped with low-energy ion guns and cooling stage. (b) Commercially available ion-milling device.

Another detrimental effect of ion beam sputtering is the formation of amorphized surface layers, which has been one of the major limiting factors for

quantitative analysis of HRTEM images [42]. Many artifacts, like radiation induced defect agglomeration or segregation, are further triggered by beam heating of the TEM specimen during the thinning process [43]. Both experimental and theoretical studies have shown that under normal ion milling conditions, temperatures of up to several hundreds of °C can be generated at the specimen surface [44]. The improvements in specimen stage design including the specimen holders assisted with liquid nitrogen (LN₂) cooling helped to avoid excessive heating of the specimen [45].

However, the most remarkable and pronounced improvement of the surface quality is achieved with the advent of stable ion sources operating at ultra-low energies (in the energy regime from 100 eV to 500 eV) producing beam sizes as small as a few microns [46]. Fig. 7.8(a) and 7.8(b) show HRTEM images of Si/SiGe interfaces obtained from two specimens prepared under different conditions. The first specimen (Fig. 7.8(a)) was thinned with 4 keV ions at an incident angle of 8° at both sides. In addition to the reduced contrast due to the additive noise from amorphized surface layers, the image clearly shows large contrast variations, which are more pronounced in the vicinity of the interface and prohibit both, reliable qualitative and quantitative analysis. The second specimen is prepared by lowering the ion beam energy consecutively (from 4 keV to 0.2 keV) while thinning the specimen from both sides in a LN₂ cooled stage. By reducing the amorphous damage-layer thickness, high contrast HRTEM images can be obtained as shown in Fig. 7.8(b). In addition, the pronounced contrast variations are eliminated revealing the defect-free structure of the interface.

Reactive ion techniques are also available to reduce the artifacts arising from Ar ion milling. *Reactive ion beam etching* (RIBE), where the inert gas is replaced by reactive gases (mainly halogen-containing gases), has shown to reduce the ion milling induced defects, e.g. in II-VI compound semiconductors like CdTe and ZnS by using iodine ions for thinning [47]. *Chemically assisted ion beam etching* (CAIBE), where the reactive gas is kept in contact with the specimen while it is being milled with Ar ions, can be applied to III-V group semiconductors like InP, where the formation of In islands by Ar milling is avoided [48].

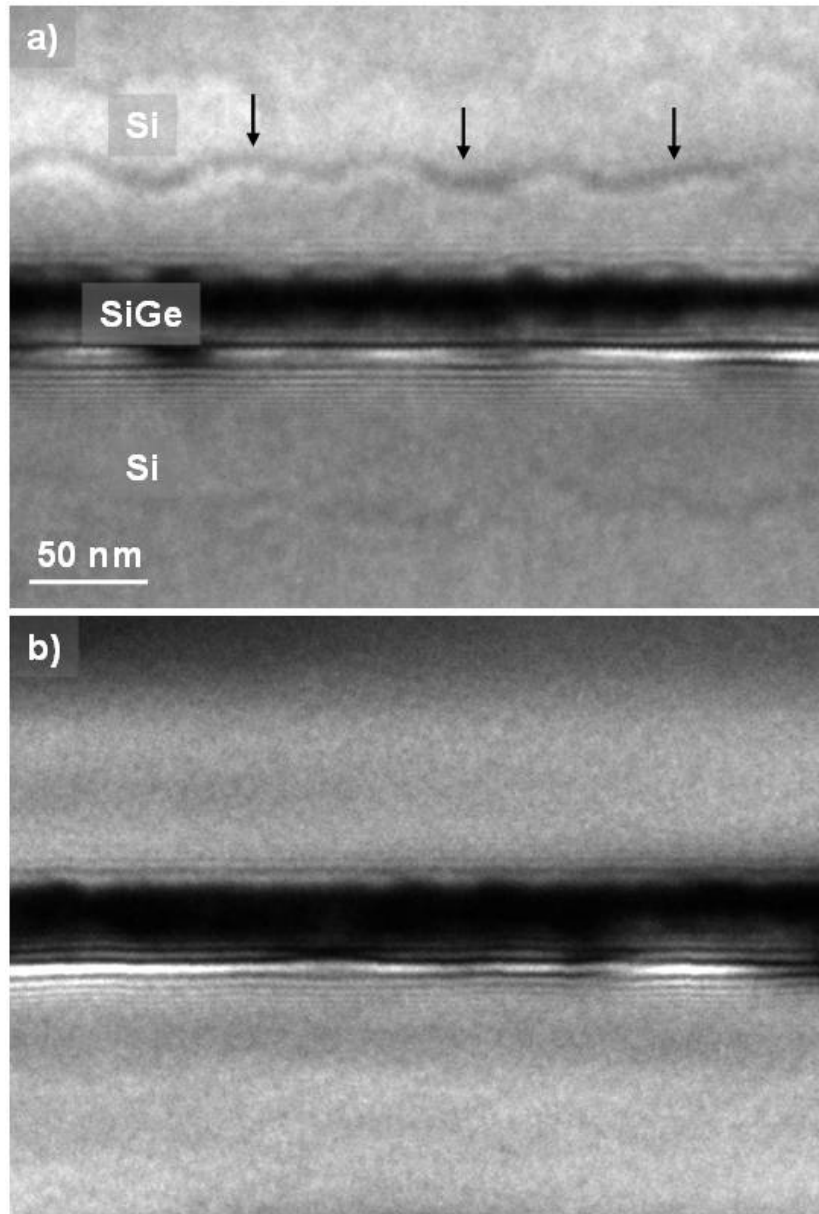


Fig. 7.7: Largely defocused DF images of a Si/SiGe heterostructure to demonstrate the topographical artefacts due to preferential thinning. a) The specimen is thinned at surfaces, top and bottom surface, using Ar ions and an accelerating voltage of 4 kV at an incidence angle of 8° while oscillating at a sector field of $\pm 20^\circ$. Preferential sputtering across the interface and re-deposition of sputtered material modify the surface topography as marked with black arrows. b) The artifacts due to preferential thinning are minimized by reducing the incidence beam angle to 1° , while rotating the specimen continuously. The defocus in a) and in b) are identical, $\Delta f = -25 \mu\text{m}$.

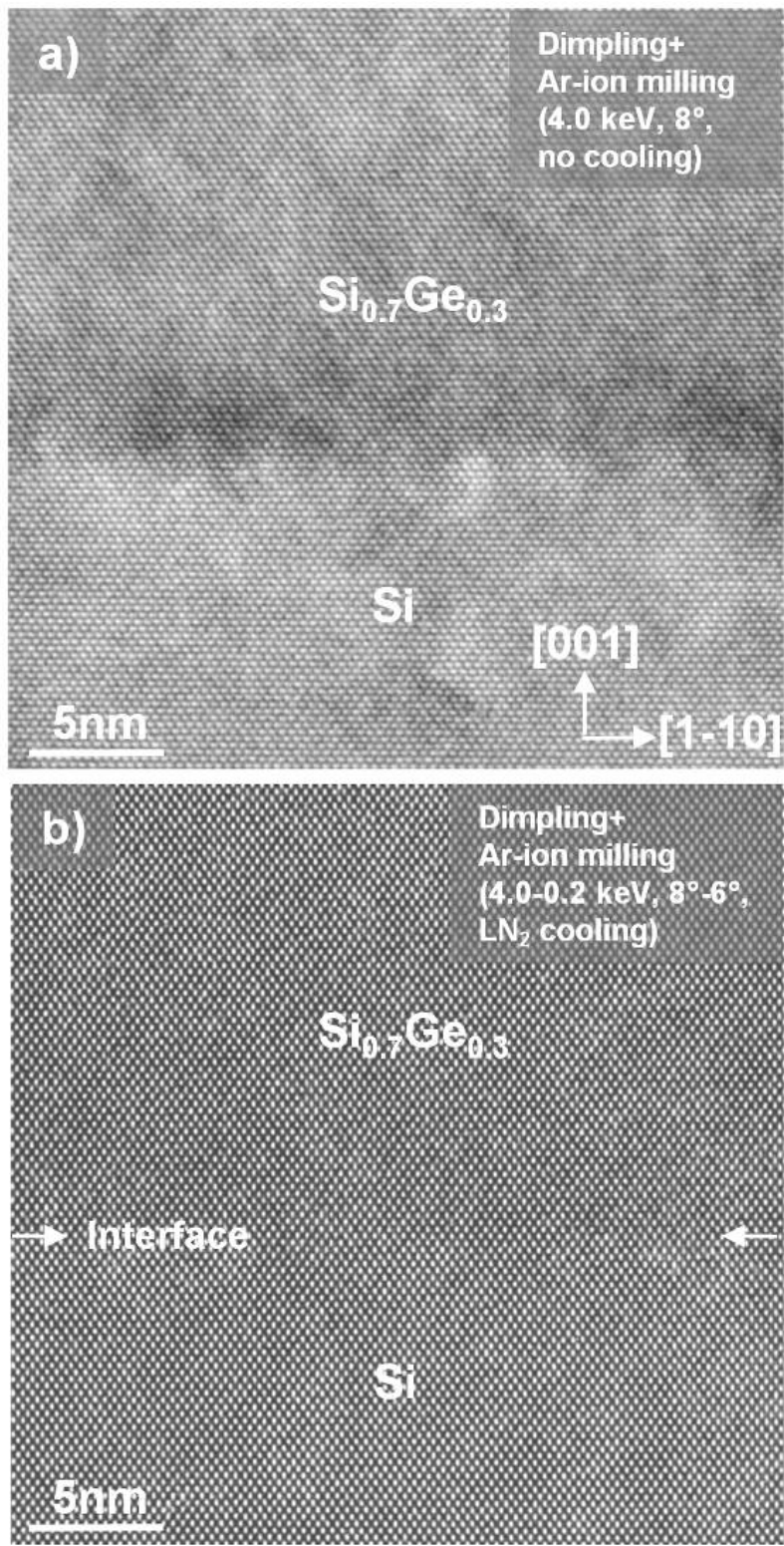


Fig. 7.8: HRTEM images of a Si/SiGe interfaces obtained from two different specimens under similar imaging conditions using a JEOL 4000EX TEM operating at 400 kV. (a) The specimen is thinned with 4 keV ions at an angle of 8° from both sides simultaneously without cooling. (b) The sample is simultaneously thinned from both sides using a liquid nitrogen cooled stage with energies consecutively lowered from 4 keV down to 0.2 keV while the incident beam angle was slightly decreased from 8° to 6° in the final low-energy ion milling step.

7.6 Tripod polishing

The tripod polishing method was originally developed to prepare site-specific, Si semiconductor device TEM specimens with large transparent areas [49]. The application of the method has been extended to broader range of hard materials like other types of semiconductors and ceramics or composite materials [50]. The basic setup relies on mechanical wet polishing of a pre-cut specimen on a rotating wheel using a hand-held tripod sample holder (Fig. 7.9(a)). A sequence of progressively finer diamond lapping films (with a granularity ranging from 30 μm to 0.1 μm) is used as abrasive material while reducing the rotation speed (typically from 100 rpm to 10-5 rpm) accordingly. The specimen surface is then briefly polished with a cloth wheel using colloidal silica slurries (with a grain size of 0.05 μm to 0.02 μm) to attain a scratch-free final polished surface. By introducing an angle between the first polished surface and the opposite surface during final polishing, it is possible to obtain an electron transparent wedge. In addition to preparation TEM specimens in either plan-view or cross section format (Fig. 7.9(b)), the method is widely used for pre-thinning prior to focused ion beam milling or for backside polishing of integrated circuits [51].

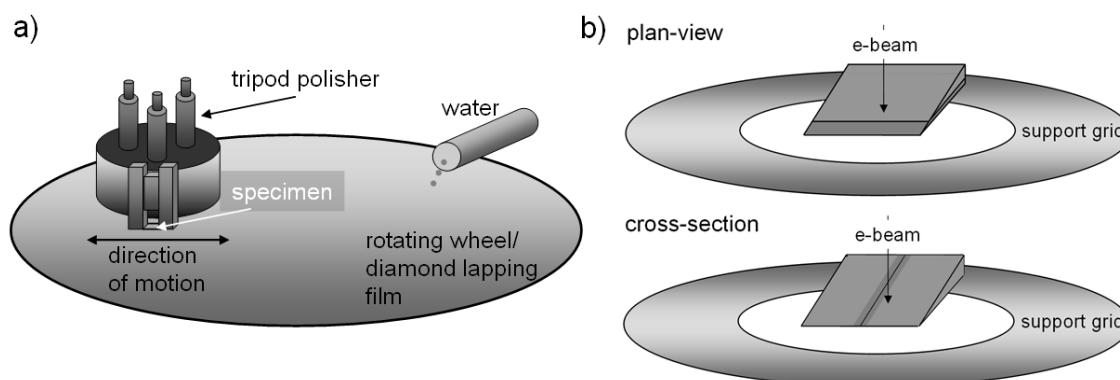


Fig. 7.9: (a) Schematic diagram of tripod polishing. (b) Diagram of tripod wedge specimens prepared for plan-view and cross-section investigations.

Although mechanical thinning by tripod polishing is a delicate operation, the introduction of automated and mechanically more stable tripod polishing systems (Fig. 7.10) has allowed controlling key parameters like specimen thickness, polishing speed, applied load and wedge angle with high precision and high reproducibility [52]. Consistent sample rotation, oscillation and load provide uniform material removal and

eliminate the artifacts that are associated with manual polishing. The desired wedge angle remains intact throughout the thinning process by letting only the sample contact with the abrasive.



Fig. 7.10: Automated tripod polishing machine for precise control of specimen thickness, wedge angle and applied load. A simpler hand-held version is shown in the upper inset.

In Fig. 7.11 a cross-section bright-field image of an array of pMOS transistors extracted from an integrated circuit demonstrates the high precision in TEM sample preparation achieved for semiconductor devices with repeating structures. Much larger electron-transparent areas with uniform thickness are achievable compared to conventional preparation methods. In addition, by optimizing the wedge angle depending on the material system investigated bending of the thinner regions of the specimen and, thus, artifacts like bending contours are avoided.

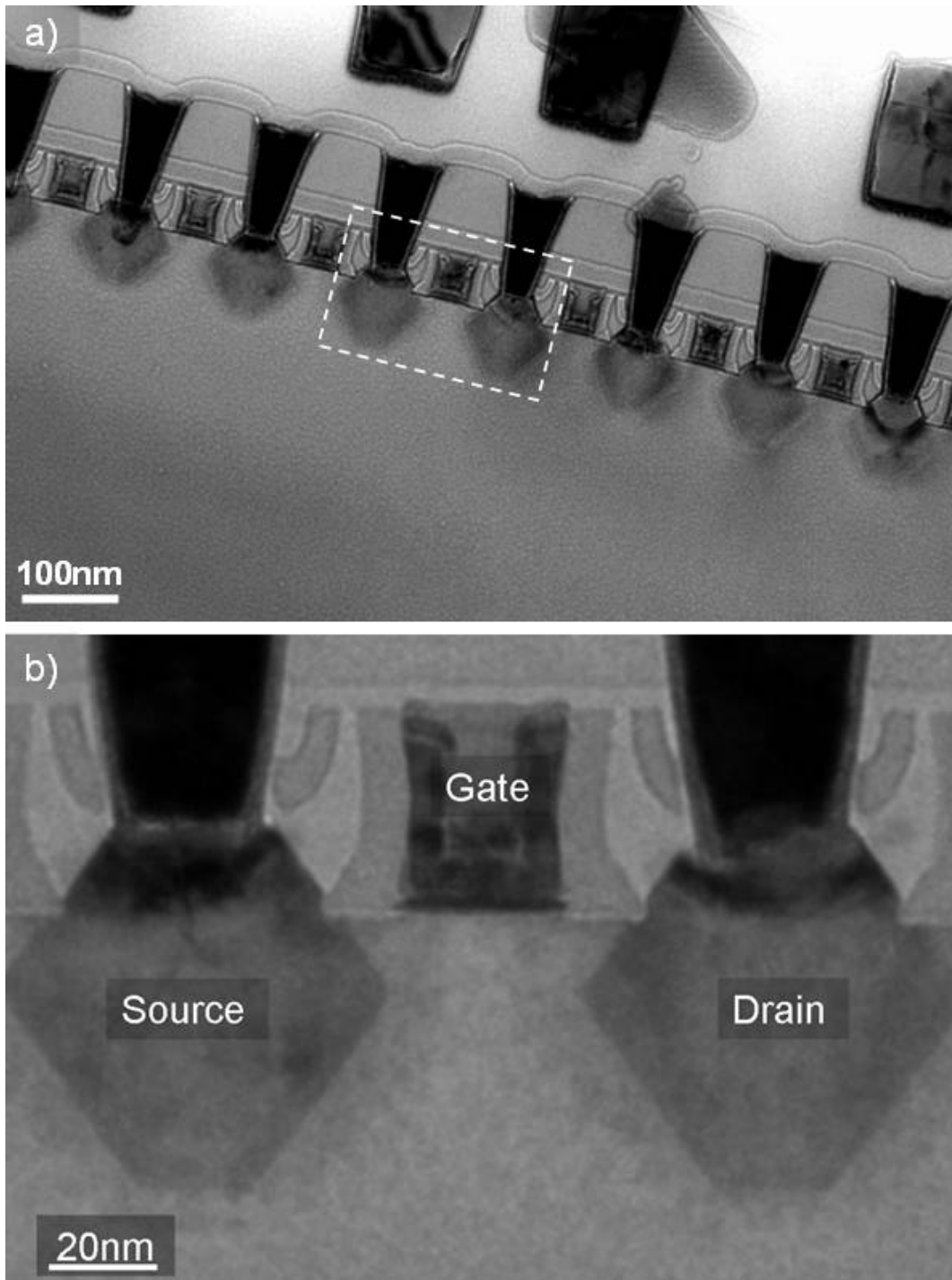


Fig. 7.11: Bright-field TEM image of a pMOS transistor array (the enlargement displays the main components of the single transistor) obtained from a cross-section specimen prepared by tripod polishing. Relatively large electron transparent areas with uniform thickness are achievable compared to conventional sample preparation, e.g. using dimple grinding and ion milling.

7.7 Ultramicrotomy

Ultramicrotomy has been routinely used for the preparation of soft biological materials using glass knives since the 1950s [53]. The development of instrumentation and introduction of defect-free diamond knives in the early 1970s enabled the use of ultramicrotomy also for the preparation of different hard materials such as metals, ceramics, semiconductors and composites [54-55].

Ultramicrotomy is a technique used to prepare thin slices with a thickness less than 100 nm. The preparation process is purely mechanical relying on plastic deformation and/or micro-crack initiation that propagates and extends into the sample. Bulk materials that are strong enough to resist the cutting force and remain rigid can be prepared without any additional support. When the sample is soft, porous, small or too brittle embedding in resin or in epoxy is necessary. A typical basic setup of an ultramicrotome device is demonstrated in Fig. 7.12. The procedure involves trimming of the sample block on one side to a pyramidal shape in order to produce a very small surface area (Fig. 7.13(a)). Harder materials require smaller areas. The sample is mounted into an ultramicrotome holder to section thin slices onto a liquid, in most cases distilled water. The sections should be then collected onto the supporting grids (Fig. 7.13(b)).

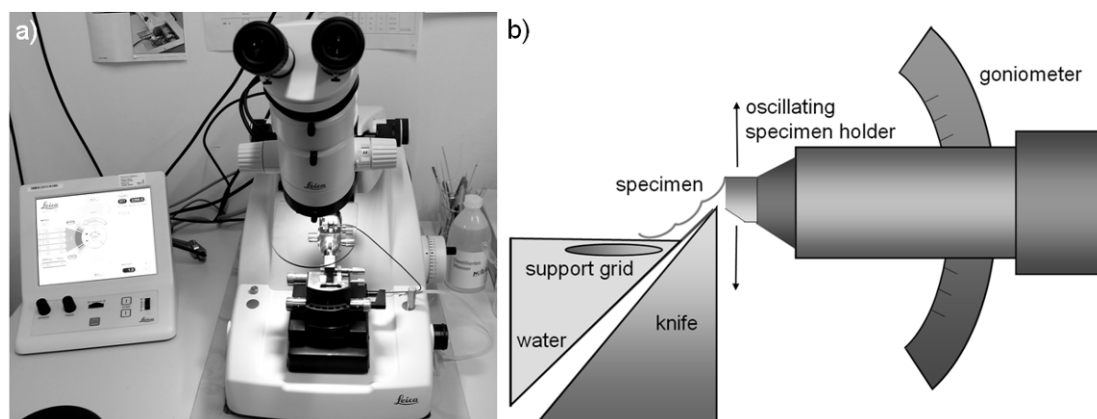


Fig. 7.12: (a) Ultramicrotome for sectioning thin lamellas from biological and industrial materials. (b) Schematic diagram of ultramicrotomy: The specimen, generally embedded in resin or epoxy, is moved precisely across the knife edge with the help of oscillating specimen holder. Thin slices of material are then collected from a liquid medium onto the specimen grid.

The technique can be used at room temperature or at low temperature (cryo-ultramicrotomy). Samples prepared by ultramicrotomy do not undergo any irradiation damage, chemical mixing or preferential thinning. Additionally, many thin sections can be prepared in a relatively short time. However, mechanical damage of the specimens, like compression in soft samples or formation of cracks in brittle samples, can still be a limitation.

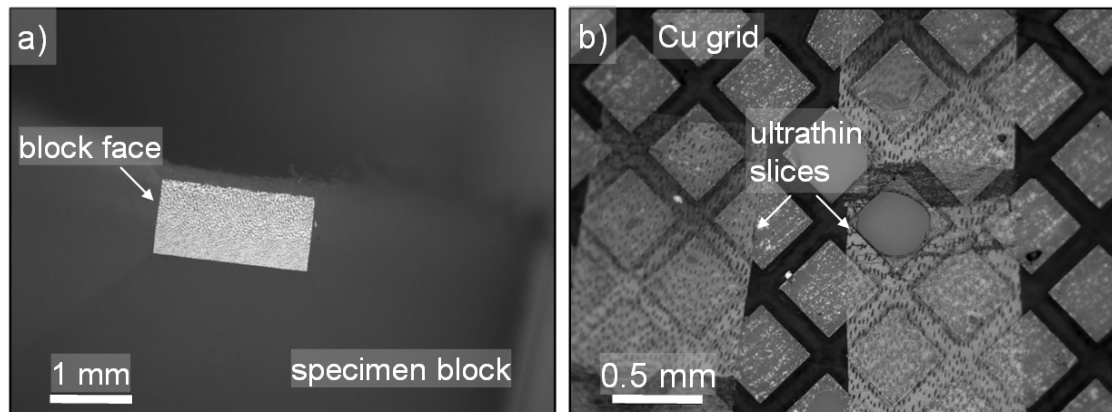


Fig. 7.13: (a) Trimmed specimen block of human dentin with a pyramidal shape. (b) Ultrathin slices of material on a mesh Cu grid (sample courtesy of: Birgit Bussmann, unpublished results).

7.8 Focused ion beam milling

Although the early development of focused ion beam (FIB) workstations has been driven by the microelectronics industry due to their unique site-specificity and performance for chip modification and circuit failure analysis, the FIB is being realized as a powerful characterization and sample preparation tool for almost any materials system ranging from hard materials [56,57], e.g. like metals, semiconductors or ceramics, to soft matter [58,59], e.g. like polymers or biological materials.

The principle of sample preparation in a FIB instrument, which generally consists of an ion gun attached to a scanning electron microscope column (referred as dual-beam or cross-beam), relies on sputtering off the material by scanning the ion beam over the region of interest (Fig. 7.14(a)). Originally, Ga has been used as a liquid metal ion source (LMIS) because of its low melting point – which is near room temperature – and its ease of focusing it into a very fine probe. Over the years, the resolution of focused ion beam milling has improved dramatically from 50-100 nm to 5 nm or better whereas higher milling rates are achieved with the increased beam currents (higher than 50 nA) [60]. More recently, inductively coupled plasma (ICP) sources are incorporated into FIB systems [61]. The use of heavier ions like Xe at higher beam currents enabled much higher sputter rates allowing preparation of larger area cross-sections [62].

Three fundamental FIB techniques to prepare TEM lamellae are (i) the H-bar or trench method [63], (ii) the in-situ lift-out method [64] and (iii) the ex-situ lift-out method [65]. Prior to cutting, a metal or a carbon layer should be deposited on the area of interest to protect the surface during the specimen milling process. In the *H-bar or trench technique*, a thin slice of material should be mechanically polished to a thickness of approximately 50 μm , fastened to a special support grid (Fig. 7.14(b)) and mounted vertically in the FIB.

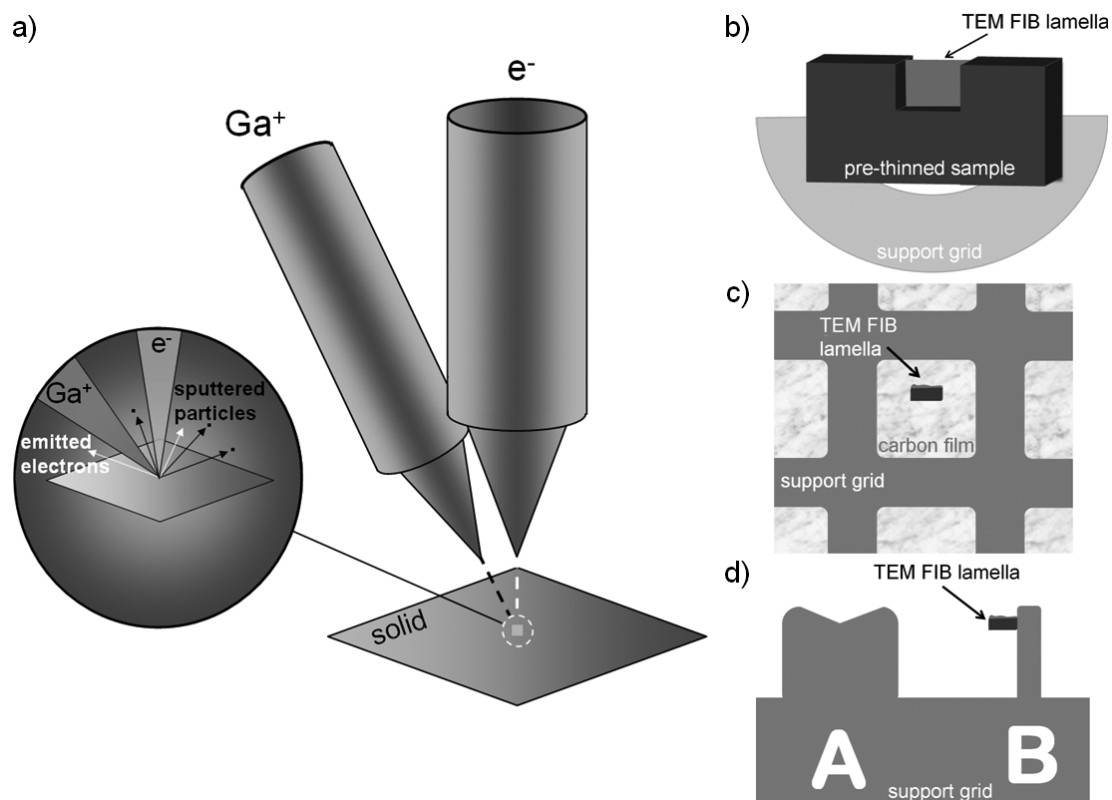


Fig. 7.14: (a) Principle of a two-beam (ion-electron) FIB. Schematic diagrams of TEM samples prepared by different FIB thinning techniques: (b) H-bar or trench method, (c) ex-situ lift out and (d) in-situ lift out.

The FIB is used to cut two trenches from each side and a thin electron transparent slice or lamella remains connected to the bulk material. The *in-situ lift-out method* relies on extraction of a thicker lamella (up to $\sim 5 \mu\text{m}$) from a site-specific region, which is then transferred to a TEM half grid using a micromanipulator. The probe of the micromanipulator is attached to the sample by FIB metal deposition and then the sample that was lifted out is attached to a TEM grid (Fig. 7.14(d)). Consecutively, the TEM sample is further thinned to electron transparency. TEM samples prepared in such a way can be additionally thinned in the FIB. For the *ex-situ lift-out method*, a lamella from a site-specific region is milled to electron transparency. Both sides and the base of the sample are cut by the ion beam. The sample is then transferred from the FIB onto a carbon-coated TEM grid (Fig. 7.14(c)) using an electrostatic micromanipulator under an optical microscope. Samples prepared in this way are not very suitable for further thinning. Lift-out methods are significantly faster compared to H-bar technique, since no mechanical pre-thinning is required.

Despite the fast and precise micro-sampling achieved over the years, the application of FIB sample preparation for quantitative analysis at the nanometer scale

has been limited due to severe sample damage resulting from heavy ion implantation during the sputtering process. Various procedures as well as different ion sources have been applied to reduce or repair these damages [66,67]. For semiconductor materials, amorphized surface layers (typically 30 nm thick side wall damage for Si sample prepared at 30 keV) are formed proportional to the accelerating energies used for FIB milling. Improved FIB columns operating at energies as low as 1-2 keV have been available, reducing the modified layer thickness to few nanometers [68]. In addition, new column designs like triple beam systems are commercialized, combining a focused low-energy noble gas ion beam column (Ar^+ , Xe^+) with a FIB and an SEM column. Small diameter low energy scanning Ar ion beam (500-1000V, 10 nA, 100 μm) coincident with SEM imaging provides precise control of the lamella thickness during the final polishing process [69]. Fig. 7.15(a) displays the lift-out lamella of a YAG-bicrystal material before and after the in-situ Ar ion polishing at 1 keV. Reduced surface damage and roughness improves the HRTEM image quality allowing the structural characterization of the bi-crystal grain boundary (Fig. 7.15(b)).

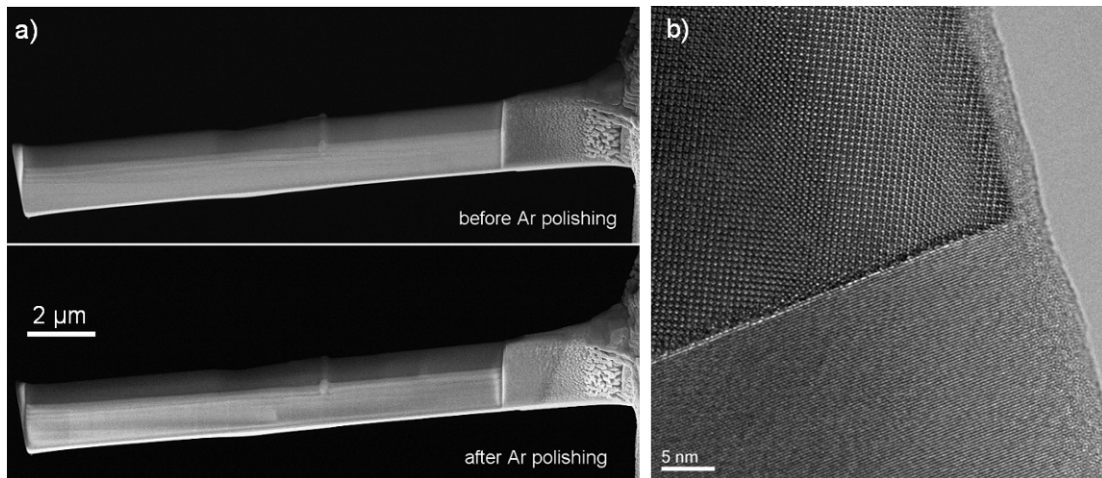


Fig. 7.15: In-situ low energy Ar ion milling: (a) Lift-out lamella of a YAG bi-crystal before and after 1 keV Ar polishing. Monitoring the polishing procedure by SEM allows precise control of the minimum thickness as well as the surface damage of the lamella. (b) HRTEM image of the bi-crystal grain boundary after final polishing (Sample courtesy of: K. Hartmann, TEM imaging: S. Irsen, unpublished results).

Although the FIB is more frequently used in the field of semiconductor materials, with the development of the in-situ lift-out technique it has become a powerful tool to prepare thin sections from mechanically unstable material systems like polymers, biological samples or materials with porous structures. Fig. 7.16

demonstrates the use of the FIB for the preparation of samples consisting of dense SiC fibers in a relatively porous and polycrystalline SiC matrix (Fig. 7.16(a)). Different thinning properties of the fibers and the polycrystalline matrix lead to mechanically unstable samples, as has already been shown on the same samples that were prepared by classical ion-milling or wedge-shape polishing methods [70]. Thickness differences across the fiber/matrix interface hindered detailed studies across that interface. The TEM sample preparation of this material with the FIB was a challenging enterprise. First, a platinum strap was deposited directly onto the region of interest in order to protect the sample and to additionally improve the mechanical support. FIB milling was then carried out using the gallium ion source operated at 30 kV (Fig. 7.16(b)). The TEM lamella was lifted out using an in-situ micromanipulator (Fig. 7.16(c)) and fastened to a Cu-grid. Pores in the matrix were filled with Pt (Fig. 7.16(d)) and only selected parts were thinned using Ga ions to a thickness of around 50 – 70 nm (Fig. 7.16(e)). By this way the prepared samples are robust enough to be handled and additionally they offer thin areas for a detailed TEM investigation (Fig. 7.16(f)).

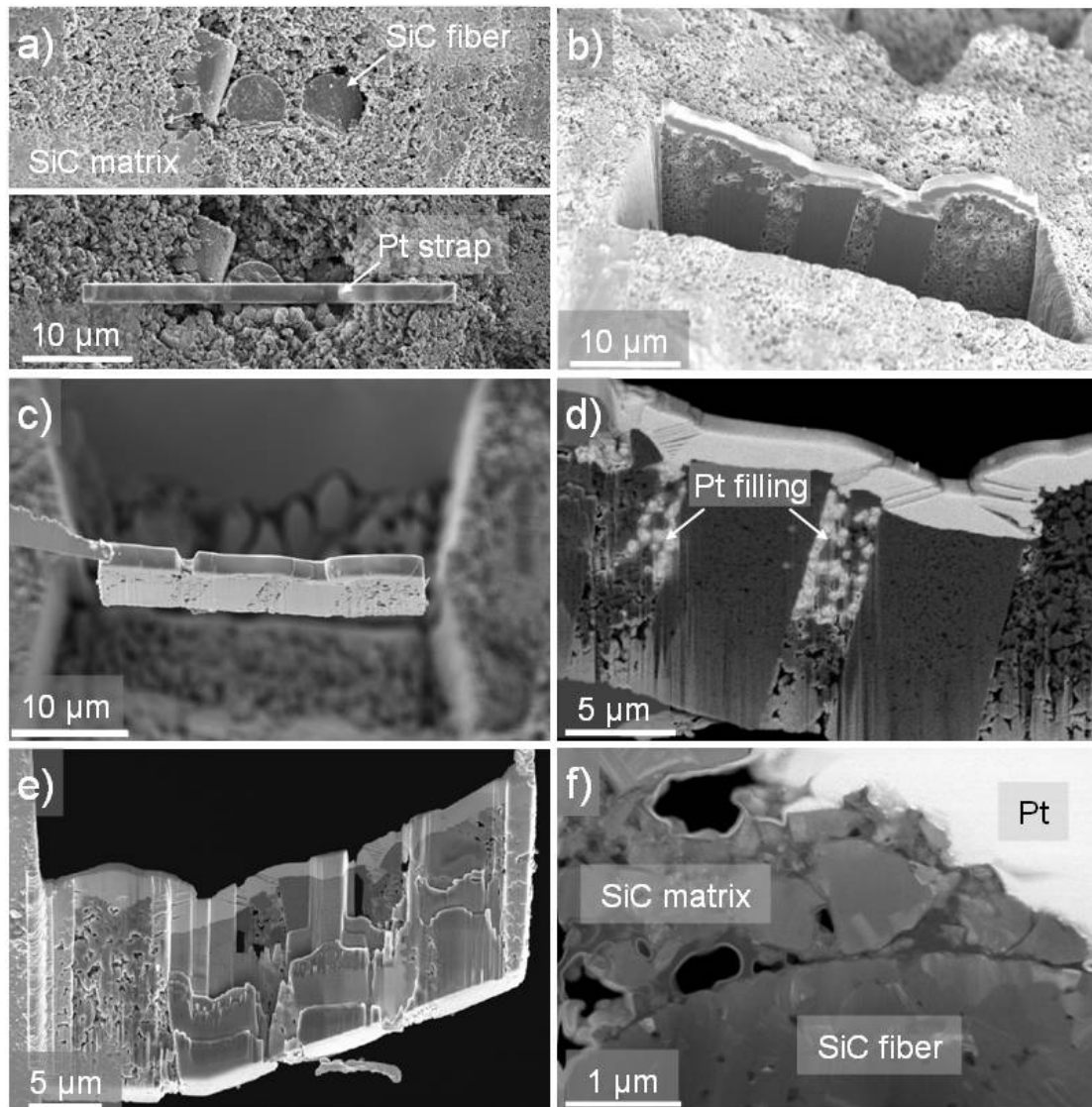


Fig. 7.16: In-situ lift out technique to prepare cross-section from a porous composite material: (a) Secondary electron image of SiC fibers in a porous SiC matrix and the Pt layer deposited onto the area of interest. (b) Sectioning of a thin lamella by sputtering of the material by focused Ga ions at 30 keV. (c) Extracting the lamella using a micromanipulator to mount on a support grid. (d) Filling the pores in the matrix with Pt prior to final thinning. (e) TEM lamella after the final thinning at 5 keV. (f) Annular dark-field STEM image of the cross-section (specimen courtesy: Tea Toplisek, FIB sample preparation by Bernhard Fenk, ADF-STEM investigations by Vesna Srot, unpublished results).

7.9 Combination of different preparation methods

Over the past decades, sample preparation techniques have evolved remarkably in terms of precision, reliability and reproducibility parallel to the requirements for state of the art characterization techniques. However, depending on the physical, chemical or structural nature of the material to be characterized, combination of different preparation methods are generally applied to overcome the challenges as well as to reduce the preparation-related artifacts.

Tripod polishing is a useful technique to prepare wedge specimens from hard materials with relatively uniform and large electron-transparent areas. The control of mechanical stability at the final stage of thinning might be difficult for brittle materials. In addition, residual polishing artifacts rising from chemical slurries or fine particles may alter the surface quality. Alternatively, combining tripod thinning with successive final low-energy ion milling (typically 2.0 – 0.5 keV), it is even possible to obtain high-quality specimens for HRTEM, as shown in Fig. 7.17. The figure displays an HRTEM image of a pMOS transistor, where uniform image contrast across the channel region allows quantitative analysis like nanometer-scale strain mapping for instance.

Modification in the composition of irradiation-sensitive alloys and compounds as a consequence of ion bombardment has been known for many years. Tripod polishing can be used as an alternative to dimple-grinding to achieve thinner specimens prior to ion-milling. Fig. 7.18 displays an HRTEM image of the active region of a light-emitting diode consisting of ion-beam sensitive InGaN quantum wells, where the specimen was prepared by tripod polishing [71]. Since the time necessary for final ion-beam thinning is remarkably reduced (typically on the order of 5 to 10 min at 2.0 keV for Si) compared to conventional techniques (typically several hours at 4 keV for a dimpled Si specimen), sample preparation of such materials can be realized without alteration of the original structure allowing reliable quantitative analysis.

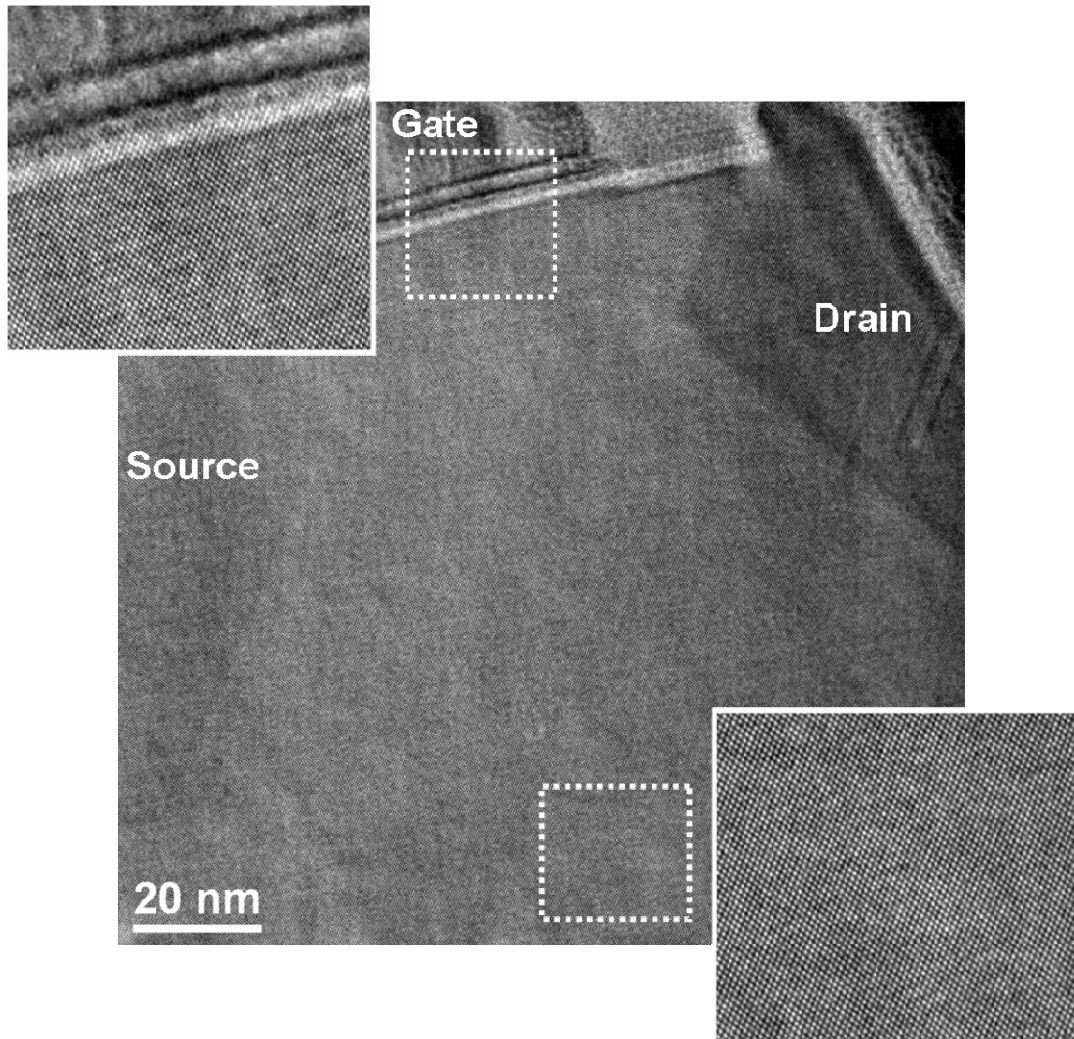


Fig. 7.17: HRTEM image of a PMOS transistor channel region obtained from a specimen prepared by automated tripod polishing followed by low energy Ar ion milling at 0.5 keV. A homogeneous specimen thickness and flat exit surfaces are necessary to obtain HRTEM images with uniform contrast across the field of view (see the enlargements from dashed squares).

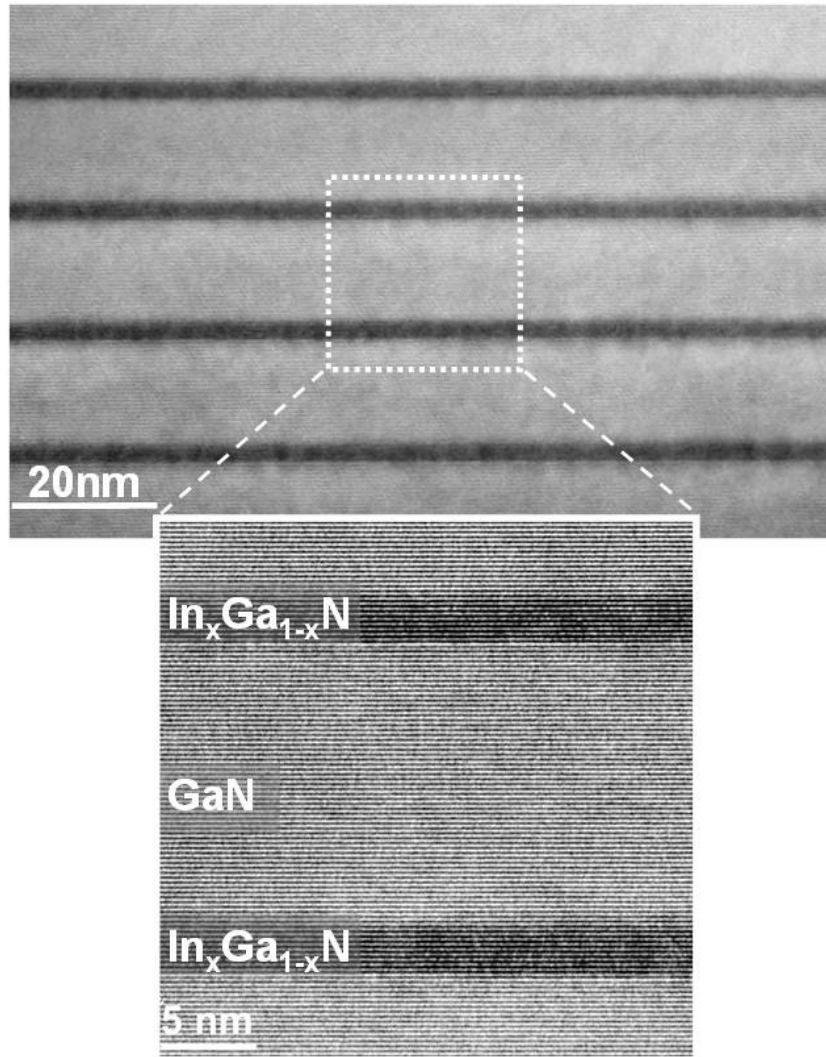


Fig. 7.18: (0002) HRTEM image of the active region in a high-efficiency light-emitting diode. Two 2.5 nm-thick InGaN quantum wells with sharp bottom and diffused upper interfaces are shown in the enlargement. Reduced ion milling times for the final ion thinning successively to tripod polishing minimizes the alteration of composition and morphology and reveals the original structure of the ion-beam sensitive InGaN multi quantum wells for quantitative analysis.

References

- [1] Hirsch, P.B., Nicholson, R.B., Howie, A., Pashley, D.W. and Whelan, M.J. (1965) *Electron Microscopy of Thin Crystals*, Butterworths, London.
- [2] Goodhew, P.J. (1985) *Thin Foil Preparation for Electron Microscopy*, in *Practical Methods in Electron Microscopy*, vol. 11 (ed A. Glauert), Elsevier, Amsterdam.
- [3] Goodhew, P.J. (1984) *Specimen Preparation for Transmission Electron Microscopy of Materials*, Bios Scientific Publishers, Oxford.
- [4] Williams, D.B. and Carter, C.B. (2009) *Transmission Electron Microscopy: A Text Book for Materials Science*, Springer, New York.
- [5] Brawman, J.C., Anderson R.M. and McDonald, M.L. (eds) (1988) *Specimen Preparation for Transmission Electron Microscopy of Materials*, vol. 115, Materials Research Society, Pittsburgh.
- [6] Anderson, R.M. (ed) (1990) *Specimen Preparation for Transmission Electron Microscopy of Materials II*, vol. 199, Materials Research Society, Pittsburgh.
- [7] Anderson, R.M., Tracy, B. and Bravman, J. (eds) (1992) *Specimen Preparation for Transmission Electron Microscopy of Materials III*, vol. 254, Materials Research Society, Pittsburgh.
- [8] Anderson, R.M., Walck, S.D. (eds) (1997) *Specimen Preparation for Transmission Electron Microscopy of Materials IV*, vol. 480, Materials Research Society, Pittsburgh.
- [9] Barna, A., Radnoczi, G. and Pecz, B. (1997) *Preparation techniques for Transmission Electron Microscopy*, in *Handbook of Microscopy: Applications in Materials Science*, Solid-state Physics and Chemistry (eds Amelinckx, S., van Dyck, D., van Landuyt, J. and van Tendeloo, G.), VCH, Weinheim, pp 751-801.
- [10] Ayache, J., Beaunier, L., Boumendil, J., Ehret, G. and Laub, D. (2010) *Sample preparation Handbook for Transmission Electron Microscopy: Techniques*, Springer, Berlin.
- [11] Ayache, J., Beaunier, L., Boumendil, J., Ehret, G. and Laub, D. (2010) *Sample preparation Handbook for Transmission Electron Microscopy: Methods*, Springer, Berlin.
- [12] <http://temsamprep.in2p3.fr/> (21.04.2011).
- [13] http://www.gatan.com/products/specimen_prep/ (21.04.2011).

- [14] <http://www.southbaytech.com/> (21.04.2011).
- [15] <http://www.fishione.com/> (21.04.2011).
- [16] <http://www.leica-microsystems.com/products/electron-microscope-sample-preparation/> (21..2011).
- [17] Willison, J.H.M and Rowe, A.J. (1980) *Replica, shadowing and freeze-etching techniques*, in Practical Methods in Electron Microscopy, vol. 8 (ed A.M. Glauert), Elsevier, Amsterdam, pp. 171-301.
- [18] Adachi, K.K., Hojou, K., Katoh, M. and Kanaya, K. (1976) *High resolution shadowing for electron microscopy by sputter deposition*, Ultramicroscopy, 2, pp. 17-29.
- [19] Carpenter, G.J.C, Yelim, J.N.G., and Phaneuf, M.W. (1994) *Extraction of second phases from magnesium and aluminum alloys for analytical electron microscopy*, Microscopy Research and Technique, 28, pp. 422-426.
- [20] Severs, N.J., (2007) *Freeze-fracture electron microscopy*, Nature Protocols, 2, pp. 547- 576.
- [21] Robenek, H. and Severs, N.J., (2007) *Recent advances in freeze-fracture electron microscopy: the replica immunolabeling technique*, Biological Procedures Online, 10 (1), pp. 9-19.
- [22] Ayache, J., Beaunier, L., Boumendil, J., Ehret, G. and Laub, D. (2010) *Sample preparation Handbook for Transmission Electron Microscopy: Techniques*, Springer, Berlin, pp. 160-177.
- [23] Hetherington, C.J.D (1988) *Preparation of semiconductor cross sections by cleaving*, in *Specimen Preparation for Transmission Electron Microscopy*, vol. 115 (eds J.C. Bravman, R.M. Anderson and M.L McDonald) Materials Research Society, Pittsburgh, pp. 143-148.
- [24] McCaffrey, J.P., (1991) *Small-angle cleavage of semiconductors for transmission electron microscopy*, Ultramicroscopy, 38, pp. 149-157.
- [25] Scott, D.W. and McCaffrey, J.P., (1997) *The small angle cleavage technique: an update*, in *Specimen Preparation for Transmission Electron Microscopy IV*, vol. 480 (eds R.M. Anderson, S.D. Walck) Materials Research Society, Pittsburgh, pp. 3-42.
- [26] http://www.southbaytech.com/appnotes/60_pre-thinning_for_fib_tem_sample_preparation_using_the_small_angle_cleavage_technique.pdf/ (21.04.2011).

- [27] Walck, S.D. and McCaffrey, J.P., (1997) *The small angle cleavage technique applied to coatings and thin films*, Thin Solid Films, 308-309, pp. 399-405.
- [28] Nowak, J.D., Song, S.H., Campell, S.A., and Carter, C.B. (2008) *TEM study of ytterbium silicide thin films*, in Microscopy of Semiconducting Materials 2007, vol. 120(5) (eds A.G. Cullis and P.A. Midgley) Springer, Bristol, pp. 333-336.
- [29] Wheeler, R., (1991) *Electropolishing of polycrystalline and single-crystal $YBa_2Cu_3O_{7-\delta}$ for TEM studies*, Ultramicroscopy, 35, pp. 59-64.
- [30] Wang, N. and Fung, K.K., (1995) *Preparation of TEM plan-view and cross-sectional specimens of ZnSe/GaAs epilayers by chemical thinning and argon ion milling*, Ultramicroscopy, 60, pp. 427-435.
- [31] Aebersold, J.F., Stadelmann, P.A. and Matlosz, M., (1996) *A rotating disk electropolishing technique for TEM sample preparation*, Ultramicroscopy, 62, pp. 157-169.
- [32] Goodhew, P.J., (1985) *Final thinning: chemical and electropolishing*, in Thin Foil Preparation for Electron Microscopy, (Practical Methods in Electron Microscopy), vol. 11 (ed A. Glauert), Elsevier, Amsterdam, pp. 51-102.
- [33] Hirsch, P.B., Nicholson, R.B., Howie, A., Pashley, D.W. and Whelan, M.J. (1965) *Electron Microscopy of Thin Crystals*, Butterworths, London, Appendix 1, p. 453, and references therein.
- [34] Witcomb, M.J. and Dahmen, U., (1995) *Method for jet polishing two-phase materials*, Microscopy Research and Technique, 32, pp. 70-74.
- [35] Howard, D.J., Paine, D.C. and Sacks, R.N., (1991) *Large-area plan-view sample preparation for GaAs-based systems grown by molecular beam epitaxy*, Journal of Electro Microscopy Technique, 18, pp. 117-120.
- [36] Kim, Y., Ourmazd, A., Bode, M. and Feldman, R.D., (1989) *Nonlinear diffusion in multilayered semiconductor systems*, Physical Review Letters, 63 (6), pp. 636-639.
- [37] Ayache, J., Beaunier, L., Boumendil, J., Ehret, G. and Laub, D. (2010) *Sample preparation Handbook for Transmission Electron Microscopy: Techniques*, Springer, Berlin, pp. 125-135.
- [38] Strecker, A., Mayer, J., Baretzky, B., Eigenthaler, U., Gemming, T., Schweinfest, R., and Rühle, M., (1999) *Optimization of TEM specimen preparation by double-sided ion beam thinning under low angles*, Journal of Electron Microscopy, 48 (3), pp. 235-244.

- [39] Barna, A., Gosztola, L., and Reisinger, G., (1989) Hungarian Patent, No. 205814.
- [40] Barna, A., (1992) *Topographic kinetics and practice of low angle ion beam thinning*, in Specimen Preparation for Transmission Electron Microscopy III, vol. 254 (ed R.M. Anderson), Materials Research Society, Pittsburgh, pp. 3-22.
- [41] Tagg, M.A., Smith, R., and Walls, J.M., (1986) *Sample rocking and rotation in ion beam etching*, Journal of Materials Science, 21, pp. 123-130.
- [42] Müller, K.P. and Pelka, J., (1987) *Redeposition in ion milling*, *Microelectronic Engineering*, 7, pp. 91-101.
- [43] Kim, M.J. and Carpenter, R.W., (1987) *TEM specimen heating during ion beam thinning: microstructural instability*, Ultramicroscopy, 21, pp. 327-334.
- [44] Viguier, B. and Mortensen, A., (2001) *Heating of TEM specimens during ion milling*, Ultramicroscopy, 87, pp. 123-133.
- [45] http://www.gatan.com/specimenprep/pips_cols_stage.php/ (01.05.2011).
- [46] Barna, A., Pecz, B., and Menyhard, M., (1998) *Amorphisation and surface morphology development at low energy ion milling*, Ultramicroscopy, 70, pp. 161-171.
- [47] Cullis, A.G., Chew, N.G., and Hutchinson, J.L., (1985) *Formation and elimination of surface ion milling defects in cadmium telluride, zinc sulphide and zinc selenide*, Ultramicroscopy, 17, pp. 203-212.
- [48] Alani, R., Jones, J., and Swann, P., (1990) *Chemically assisted ion beam etching (CAIBE) - A new technique for TEM specimen preparation of materials*, in Specimen Preparation for Transmission Electron Microscopy II, vol. 199 (ed R.M. Anderson), Materials Research Society, Pittsburgh, pp. 85-101.
- [49] Klepeis, S.J., Benedict, J.P., and Anderson, R.M., (1987) *A grinding/polishing tool for TEM sample preparation*, in Specimen Preparation for Transmission Electron Microscopy, vol. 115 (eds J.C. Bravman, R.M. Anderson and M.L McDonald) Materials Research Society, Pittsburgh, pp. 179-184.
- [50] Ayache, J., Beaunier, L., Boumendil, J., Ehret, G. and Laub, D. (2010) *Sample preparation Handbook for Transmission Electron Microscopy: Techniques*, Springer, Berlin, pp. 177-201.
- [51] Benedict, J.P., Anderson, R., Kelepeis, S.J., and Chaker, M., (1990) *A procedure for cross sectioning specific semiconductor devices for both SEM and*

- TEM analysis*, in Specimen Preparation for Transmission Electron Microscopy II, vol. 199 (ed R.M. Anderson), Materials Research Society, Pittsburgh, pp. 189-204.
- [52] Okuno, H., Takeguchi, M., Mitsuishi, K., Xing, J.G., and Furuya, K. (2008) *Sample preparation of GaN-based materials on a sapphire substrate for STEM analysis*, Journal of Electron Microscopy, 57 (1), pp. 1-5.
- [53] Claesson, S. and Svensson, A.A., (1956) *A new ultramicrotome for electron microscopy*, Experimental Cell Research, 11, pp. 105-114.
- [54] Malis, T.F., Steele, D., (1990) *Ultramicrotomy for materials science*, in Specimen Preparation for Transmission Electron Microscopy II, vol. 199 (ed R.M. Anderson), Materials Research Society, Pittsburgh, pp. 3-42.
- [55] Glauert, A.M., and Lewis, P.R., (1998) *Biological Specimen Preparation for Transmission Electron Microscopy*, Portland Press, London.
- [56] Gasser, P., Klotz, U.E., Khalid, F.A., and Beffort, O., (2004) *Site-specific specimen preparation by focused ion beam milling for transmission electron microscopy of metal matrix composites*, Microscopy and Microanalysis, 10, pp. 311-316.
- [57] Stevie, F.A., Shane, T.C., Kahora, P.M., Hull, R., Bahnck, D., Kannan, V.C., David, E., (1995) *Applications of focused ion beams in microelectronics production, design and development*, Surface and Interface Analysis, 23, pp. 61-68.
- [58] Loos, J., van Duren, J.K.J, Morrissey, F., and Janssen, R.A.J, (2002) *The use of the focused ion beam technique to prepare cross-sectional transmission electron microscopy specimen of polymer solar cells deposited on glass*, Polymer, 43, pp. 7493-7496.
- [59] Marko, M., Hsieh, C., Schalek, R., Frank, J., and Mannella, C., (2007) *Focused ion beam thinning of frozen-hydrated biological specimens for cryo-electron microscopy*, Nature Methods, 4 (3), pp. 215-217.
- [60] Giannuzzi, L.A., (2010) *Latest developments in FIB technology and applications*, Microscopy and Microanalysis, 10, pp. 166-167.
- [61] Smith, N.S., Skoczylas, W.P., Kellogg, S.M., Kinion, D.E., Tesch, P.P., Sutherland, O., Aanesland, A., and Boswell, R.W., (2006) *High brightness inductively coupled plasma source for high current focused ion beam applications*, Journal of Vacuum Science and Technology B, 24 (6), pp. 2902-2906.

- [62] Kellogg, S.M., Schampers, R., Zhang, S.Y., Graupera, A.A., Miller, T., Laur, W.D., and Dirriwachter, A.B., (2010) *High throughput sample preparation and analysis using an inductively coupled plasma (ICP) focused ion beam source*, *Microscopy and Microanalysis*, 16 (2), pp. 222-223.
- [63] Young, R.J., Kirk, E.C.G, Williams, D.A., and Ahmed, H., (1990) *Fabrication of planar and cross-sectional TEM specimens using focused ion beam*, in *Specimen Preparation for Transmission Electron Microscopy II*, vol. 199 (ed R.M. Anderson), Materials Research Society, Pittsburgh, pp. 205-216.
- [64] Yaguchi, T., Urao, R., Kamino, T., Ohnishi, T., Hashimoto, T., Umemura, K., and Tomimatsu, S., (2001) *A FIB micro-sampling technique and a site-specific TEM specimen preparation method for precision materials characterization*, *Materials Research Society Proceedings*, 636, pp. (D9) 35.1-35.6.
- [65] Overwijk, M.H.F., van den Heuvel, F.C., and Bulle-Lieuwma, C.W.T, (1993) *Novel scheme for the preparation of transmission electron microscopy specimens with a focused ion beam*, *Journal of Vacuum Science and Technology B*, 11 (6), pp. 2021-2024.
- [66] Mayer, J., Giannuzzi, L.A., Kamino, T., and Michael, J., (2007) *TEM sample preparation and FIB-induced damage*, *MRS Bulletin*, 32, pp. 400-407.
- [67] Kato, N.I., (2004) *Reducing focused ion beam damage to transmission electron microscopy samples*, *Japanese Society of Microscopy*, 53 (5), pp. 451-458.
- [68] Giannuzzi, L.A., Geurts, R., and Ringnalda, J., (2005) *2 keV Ga⁺ FIB milling for reducing amorphous damage in silicon*, *Microscopy and Microanalysis*, 11 (2), pp. 828-829.
- [69] Stegmann, H., Ritz, Y., Utess, D., Engelmann, H.J., and Zschech, E., (2009) *In-situ low energy argon ion milling of nanoelectronic structures using a triple beam system*, *Microscopy and Microanalysis*, 15 (2), pp. 170-171.
- [70] Gec, M., Toplisek, T., Srot, V., Drazic, G, Kobe, S., van Aken, P.A., and Ceh, M., (2008) *Preparation of SiC/SiC thin foils for TEM observation by wedge polishing method*, in *Proceedings European Microscopy Congress 2008*, vol. 1 (eds M. Luysberg, K. Tillmann, T. Weirich), Springer, Berlin, pp. 817-818.
- [71] Özdöl, V.B., Koch, C.T., and van Aken, P.A., (2010) *A nondamaging electron microscopy approach to map In distribution in InGaN light-emitting diodes*, *Journal of Applied Physics*, 108, pp. 056103-056105.

Chapter 8

Conclusions and future work

Strain mapping techniques at nanometer scale are becoming more and more important as the downscaling of the semiconductor devices continues. The main objective of the research presented here is to characterize the strain state very locally, two-dimensionally and quantitatively. HRTEM coupled with geometric phase analysis was optimized to convert the atomic position information into strain information. The HRTEM images should be taken under optimum conditions to maximize the lattice fringe contrast. Based on the standard deviation of strain measurements on Si/SiGe model structures, it can be estimated that GPA can detect strains as small as 0.1-0.2 % on a scale of 2 nm. However, it is important to note that the specimens are necessarily thin, which allow strains to relax significantly (based on the comparison of the experimental results with the theoretical calculations) with respect to the bulk state. In addition, the technique is not fully developed for sample areas where strong strain gradients exist. Application of GPA directly on reconstructed complex-valued exit-face wave function is proposed to minimize the artifacts rising from objective lens aberrations and to improve the precision by increasing the signal-to-noise ratio compared to single HRTEM images.

Dark-field inline holography method proposed in this study addresses the limitations of HRTEM based GPA. Unlike in HRTEM (images are acquired at zone axis), the reconstruction of the geometric phase is achieved by isolating the reflection of interest in two-beam Bragg diffraction condition inside the microscope. The phase of the diffracted beam is therefore much less sensitive to thickness variations and local changes in specimen orientations. Non-necessity for imaging lattice fringes breaks the barrier of the limited field of view, while at the same time the low electron dose required for image formation reduces the electron-beam induced modification of the original structure. Application of DIH on compressively strained p-MOS transistors shows that 10 times larger field of view is achievable compared to HRTEM (typically 100 nm square) allowing simultaneous strain mapping on multiple transistor channels. Semiconductor devices like InGaN-based LEDs are possible to investigate without introducing In clusters. Since the method is based on dark-field imaging,

thicker samples are desirable which in turn reduces the thin foil relaxation as demonstrated by comparison with the experimental HRTEM results on InGaN LEDs.

Strain mapping can be used as a complementary technique to correlate the structural and optical properties of semiconductor devices as well. Based on the comparative case study on an AlGaIn/GaN heterostructure, it has been demonstrated that plasmon mapping by EFTEM can be used to extract the strain information with an accuracy below 0.5%.

The application of geometric phase analysis using complex-valued exit-face wave function can be further improved based on the use of all available reflections, where the contribution of each reflection is additionally weighted by its intensity. Over the existing “two non-collinear reflection” formalism, it will be possible to increase the signal-to-noise ratio in the phase images, thus the precision in the strain maps.

Due to the increasing complexity of state-of-the-art semiconductor devices, three-dimensional strain analysis will become a key technique in the near future. The dark-field holography method should therefore be expanded to three dimensions. An alternative method is currently under development which is based on a new dark-field tilt-focal series reconstruction algorithm. It is aimed to characterize the strain state in embedded crystalline nanoparticles and semiconductor nanostructures with complex geometries.

Appendix

DM script for strain analysis

The strain analysis on geometric phase images reconstructed using DIH method was carried out by digital image processing using DigitalMicrograph script language. The following script was used to derive the tetragonal out-of-plane strain from the phase images calculated by FRWR reconstruction algorithm.

```
//Strain calculation
number width,height
number scaleX,scaleY
string unitString

number cz = 0.51420,l=2;
getnumber("Lattice constant in vertical direction (nm):",cz,cz);
getnumber("Reflection order:",l,l);
number lg = l/cz;

Image img := getfrontimage()
img.getSize(width,height)
img.getScale(scaleX,scaleY)
img.getUnitString(unitString)

Image Gy := CreateFloatImage(img.getname()+"_Eyy",width,height)
Gy = (offset(img, 0,-1)-offset(img, 0,1))/(2*scaleY);
Gy /= (-2*Pi()*lg);

Gy.setScale(scaleX,scaleY)
Gy.setUnitString(unitString)
Gy.showimage()
```

Acknowledgements

The present work was performed at the Max Planck Institute for Intelligent Systems (formerly Institute for Metals Research), in the legendary microscopy floor of the Stuttgart Center for Electron Microscopy (StEM). I would like to express my appreciation to Prof. Dr. Peter A. van Aken for providing me with great freedom during my whole research time. Apart from his scientific supervision, his professional approach to research problems is gratefully acknowledged.

I would like to thank Prof. Dr. Wolfgang Jäger for accepting me as a PhD student in the Microanalysis of Materials Department at the Kiel University (Christian-Albrechts-Universität zu Kiel). His unique way of guidance and supportive attitude at the critical points of my PhD research is invaluable.

I am more than grateful to my daily supervisor Dr. Christoph T. Koch for his continuous, encouraging and friendly co-operation. He could always tell me where I should look for the answers of my questions. His ingenious ideas have considerably contributed to the successful completion of this work.

The financial support from the European Union under the Framework 6 program under a contract for an Integrated Infrastructure Initiative, Reference 026019 (ESTEEM) is acknowledged.

My special thanks to Ute Salzberger for sharing her endless knowledge on sample preparation techniques with me. I would also like to thank Bernard Fenk and Ulrike Eigenthaler for the preparation of FIB specimens; Kersten Hahn, Peter Kopold, Marion Kelsch and Rainer Höschen for their technical support available at any time needed.

I also acknowledge random but fruitful conversations with Dr. Fritz Phillipp, Dr. Yun Jin-Phillipp, Dr. Wilfried Sigle, and Dr. Lin Gu.

I am grateful to my “family” at StEM for their help and love: “Mom” Dr. Vesna Srot, “Daddy” Dr. Paul Bellina, “Brother” Dr. Jaysen Nelayah and “Sister” Burcu Ögüt.

Finally, I would like to thank my family in Turkey for their inexhaustible support and love: My father Mesut Özdöl, my mother Setvan Özdöl, and my sister Nur Derinöz.

Curriculum Vitae

Personal

Name	Vasfi Burak Özdöl
Date and Place of Birth	21.05.1980, KDZ Eregli, Turkey
Marital Status	Single
Nationality	Turkish

Schooling

1991 – 1999	Istanbul Erkek Lisesi, Istanbul, Turkey
-------------	--

Higher education

1999 – 2004	B. Sc. in Metallurgical and Materials Engineering Middle East Technical University, Ankara, Turkey
2004 – 2006	M. Sc. in Materials Science Christian-Albrechts-Universität zu Kiel, Kiel, Germany

Dissertation

2007 – 2011	Ph.D. at Max-Planck-Institute for Intelligent Systems and Christian-Albrechts-Universität zu Kiel, Title: “Characterization of strained semiconductor structures using transmission electron microscopy”
-------------	---

Publications

- H. Stegmann, V.B. Özdöl, C.T. Koch, P.A. van Aken, H.J. Engelmann, P. Potapov and E. Zschech, *Chemical bonds in damaged and pristine low-k materials: A comparative EELS study* in *MICROELECTRONIC ENGINEERING* 85, 2169 (2008)
- V.B. Özdöl, F. Phillipp, E. Kasper and P.A. van Aken, *Quantitative local strain analysis of Si/SiGe heterostructures using HRTEM* in *Proceedings EMC 2008 14th EUROPEAN MICROSCOPY CONGRESS*, p 141-142 (2008)

- V.B. Özdöl, C.T. Koch, F. Phillipp and P.A. van Aken, *Strain measurements on Si/SiGe heterostructures using HRTEM* in Proceedings *MICROSCOPY CONFERENCE 2009 GRAZ*, p 447-448 (2009)
- L. Gu, V.B. Özdöl, W. Sigle, C.T. Koch, V. Srot and P. van Aken, *Correlating the structural, chemical, and optical properties at nanometer resolution* in *JOURNAL OF APPLIED PHYSICS* 107, 013501 (2010)
- C.T. Koch, V.B. Özdöl and P.A. van Aken, *An efficient, simple, and precise way to map strain with nanometer resolution in semiconductor devices* in *APPLIED PHYSICS LETTERS* 96, 091901 (2010)
- V.B. Özdöl, C.T. Koch and P.A. van Aken *Strain mapping of 45 nm MOSFET by dark-field inline holography* in Proceedings *MICROSC. MICROANAL.* 16, Suppl. 2, 592 (2010)
- V.B. Özdöl, C.T. Koch, and P.A. van Aken, *A nondamaging electron microscopy approach to map In distribution in InGaN light-emitting diodes* in *JOURNAL OF APPLIED PHYSICS* 108, 056103 (2010)
- V. B. Özdöl, V. Srot, and P. A. van Aken, *Dedicated sample preparation for transmission electron microscopy* in *HANDBOOK OF NANOSCOPY*, Wiley-VCH, Weinheim, in press (2011)
- P. A. van Aken, N. Y. Jin-Phillipp, C. T. Koch, B. Ögüt, V. B. Özdöl, F. Phillipp, B. Rahmati, W. Sigle, and V. Srot, *The Stuttgart Center for Electron Microscopy at the Max Planck Institute for Metals Research* in *INTERNATIONAL JOURNAL OF MATERIALS RESEARCH*, in press (2011)

Awards

Graduate Student Award at the *E-MRS Spring Meeting* (2010)

Topic: *Strain Mapping by Dark-field Inline Electron Holography*